



David Retschitzegger, BSc

**Experimental investigation in the
layout process of a hybrid powertrain
for hand-held power tools**

MASTER THESIS

to achieve the university degree of
Diplomingenieur

submitted to

Graz University of Technology

Supervising Professor
Assoc.Prof. Dipl.-Ing. Dr. techn. Roland Kirchberger
Institute of Internal Combustion Engines and Thermodynamics

Supervisor
Dipl.-Ing. Dr. techn. Hans-Jürgen Schacht
Dipl.-Ing. Dr. techn. Stephan Schmidt
Institute of Internal Combustion Engines and Thermodynamics

Graz, June 2021



Institute of Internal Combustion Engines and Thermodynamics
Chairman: Univ.-Prof. DI Dr. Helmut Eichlseder

Preface

This master thesis was written at the Institute of Internal Combustion Engines and Thermodynamics at Graz University of Technology as part of the RC-LowCAP research project.

I would like to thank the Head of the Institute, Univ.-Prof. Dipl.-Ing. Dr. techn. Helmut Eichlseder, the Head of the Department of Design, Assoc.Prof. Dipl.-Ing Dr. techn. Roland Kirchberger and Dipl.-Ing. Dr. techn. Stephan Schmidt, General Manager & Key Researcher of the RC-LowCAP research project, for making this work possible.

I would like to express my special thanks to Dipl.-Ing. Dr. techn. Hans-Jürgen Schacht for supervising this thesis and for his comprehensive technical support. Special thanks go to MSc Dimitrios Vogiatzis, who supported me daily with his technical knowledge in the execution of my master thesis. Furthermore, I would like to thank all the employees of the Department of Design for their amicable cooperation and extensive support during my master thesis.

My greatest thanks, however, go to my family and friends who have supported me with all their strength, love and patience throughout my studies and without whose support these studies would not have been possible. Equally as much gratitude is due to my girlfriend, who accompanied me with a lot of patience, love and even more understanding during the preparation of this thesis.

Table of Contents

FORMULA SYMBOLS, INDICES AND ABBREVIATIONS	VI
AFFIDAVIT.....	IX
ABSTRACT	XI
1 INTRODUCTION	2
1.1 OBJECTIVE	2
1.2 STATE OF THE ART	3
1.3 BOUNDARY CONDITIONS	4
2 THEORETICAL BACKGROUND.....	7
2.1 FOUR-STROKE SPARK-IGNITION ENGINE WITH EXTERNAL MIXTURE FORMATION	7
2.1.1 <i>Forces</i> ([2],[12],[24]).....	7
2.1.2 <i>Mean effective pressure</i> ([33],[35]).....	8
2.1.3 <i>Torque and Power</i> ([2],[35]).....	9
2.1.4 <i>Efficiency</i> ([2],[3],[35]).....	9
2.1.5 <i>Specific fuel consumption</i> ([3],[33],[35])	10
2.1.6 <i>Excess air ratio</i> ([2],[35]).....	11
2.1.7 <i>Mixture calorific value and air expenditure</i> ([2],[3],[35])	11
2.1.8 <i>Combustion process</i> ([2],[3],[33],[35]).....	12
2.1.9 <i>Exhaust emissions</i> ([2],[3]).....	14
2.1.10 <i>Mixture formation</i> ([3],[13]).....	15
2.1.11 <i>Ignition</i> ([2],[35])	16
2.2 BRUSHLESS DIRECT CURRENT MOTOR ([10],[11],[22],[24]).....	18
2.2.1 <i>Torque, Power and Efficiency</i>	18
2.2.2 <i>Number of poles and electrical turn</i>	19
2.2.3 <i>Commutation</i>	19
2.3 HYBRID DRIVE ([9],[11],[36]).....	20
2.3.1 <i>Parallel hybrid</i>	20
2.3.2 <i>Serial hybrid</i>	21
2.3.3 <i>Combined hybrid (power-split)</i>	21
3 TEST CARRIER AND CONTROLLER	22
3.1 STIHL 4-MIX ENGINE.....	22
3.2 STIHL BLDC MOTOR.....	23
3.3 MoTeC.....	24
3.4 ROBOTEQ.....	24
3.4.1 <i>Motor control modes</i> [22]	25
4 TEST-BENCH SETUP	26
4.1 DESIGN	26
4.1.1 <i>Boundary conditions</i>	26
4.1.2 <i>Three different engine setups</i>	26
4.1.3 <i>Test bench</i>	28
4.1.4 <i>ICE mounting plate</i>	29
4.1.5 <i>Connection between the crankshaft and the eddy-current brake</i>	32
4.1.6 <i>Magnetic speed sensor</i>	37
4.1.7 <i>Cooling</i>	38
4.1.8 <i>Electric Motor coupling – first design</i>	40
4.1.9 <i>Electric Motor coupling – second design</i>	42
4.2 MEASURING SETUP	44
4.2.1 <i>Reference ICE</i>	44
4.2.2 <i>ICE with modified carburettor and ignition system</i>	46
4.2.3 <i>Parallel Hybrid System</i>	48
5 EXPERIMENTAL INVESTIGATIONS.....	49
5.1 WOT COMPARISON WITH STIHL DATA.....	49

5.1.1	<i>Test setup</i>	49
5.1.2	<i>Results</i>	50
5.2	ICE CHARACTERISATION.....	50
5.2.1	<i>Test setup ignition change</i>	51
5.2.2	<i>Results ignition change</i>	51
5.2.3	<i>Test setup carburettor change</i>	53
5.2.4	<i>Results carburettor change</i>	53
5.3	PARALLEL HYBRID SYSTEM.....	58
5.3.1	<i>Test setup</i>	58
5.3.2	<i>First design results</i>	59
5.3.3	<i>Second design results</i>	59
6	CONCLUSIONS	66
7	OUTLOOK	67
	REFERENCES	68
	FIGURES	71
	TABLES	73
	APPENDIX	74
	RINGFEDER ELASTOMER JAW COUPLINGS [18].....	74

Formula symbols, indices and abbreviations

Latin formula symbols

a	m/s^2	acceleration
A	m^2	area; surface area; cross-sectional area
b_e	$\text{g}/(\text{kWh})$	brake specific fuel consumption
B	T	magnetic flux density
c	m/s	velocity
d	m	diameter
E	J	energy
f	s^{-1}	frequency
F	N	force
g	m/s^2	local gravitational acceleration
H_G	MJ/m^3	mixture calorific value (calorific value of the combustible air-fuel mixture)
I	A	electric current
l	m	length; conrod length
m	kg	mass
\dot{m}	kg/s	mass flow rate
M	$\text{N}\cdot\text{m}$	torque
n	min^{-1}	speed
O_2	$\text{kmol O}_2/\text{kmol F}$ or $\text{kg O}_2/\text{kg F}$	Amount of oxygen
$O_{2\text{min}}$	$\text{kmol O}_2/\text{kmol F}$ or $\text{kg O}_2/\text{kg F}$	minimum O_2 demand
p	bar, Pa	pressure
P	W	power
q	J/kg	specific heat
Q	J	heat
r	m	crank radius
R	Ω	electric resistance
s	m	length; distance
t	$^{\circ}\text{C}$	Celsius-temperature
T	$\text{N}\cdot\text{m}$	torque
U	V	voltage
V	m^3	volume
w	J/kg	specific work
W	J	work

Greek formula symbols

α	$^{\circ}$, rad	angle
ε	–	compression ratio
η	–	efficiency
η_e	–	effective efficiency
η_i	–	inner (indicated) efficiency
η_m	–	mechanical efficiency
λ	–	excess air ratio
λ_a	–	air expenditure
ρ	kg/m^3	density

φ	$^{\circ}$ CA	crank angle
$\phi = 1/\lambda$	–	equivalence ratio
ω	s^{-1}	angular velocity

Operators and designations

d	total differential
Π	product
Σ	sum
Δ	difference of two values; Laplace operator
\cdot	time derivative

Further indices and abbreviations

:=	definition
a	air
A/F	air-fuel ratio
BDC	bottom dead centre
BLDC	Brushless Direct Current
BMEP	brake mean effective pressure
BSFC	brake-specific fuel consumption
c	compression
cc	cubic centimeters
const	constant
CA	crank angle
CI	compression ignition
CLD	chemiluminescence detector
CO	carbon monoxide
CO ₂	carbon dioxide
COV	coefficient of variation
DIN	German Institute for Standardization
e	effective
el	electrical
ECU	engine control unit, electronic control unit
EM	electric motor
ESS	energy storage system
f	friction
FID	flame ionization detector
FMEP	friction mean effective pressure
GCV	gross calorific value (see also HHV)
HC	hydrocarbons
HHV	higher heating value (see also GCV)
i	control variable (1, 2, ..., k); inner; inferior
ICE	internal combustion engine
IMEP	indicated mean effective pressure
ISFC	indicated specific fuel consumption
ISO	International Organization for Standardization
IVT	Institute of Internal Combustion Engines and Thermodynamics
LHV	lower heating value (see also NCV)
m	mean; molar
max	maximum
min	minimum

MEP	mean effective pressure
MF	mixture formation
MFB	mass fraction burnt
MOSFET	metal-oxide-semiconductor field-effect transistor
N ₂	nitrogen
NCV	net calorific value (see also LHV)
NDIR	nondispersive infrared sensor
NO	nitrogen monoxide
NO ₂	nitrogen dioxide
NO _x	nitrogen oxides
O ₂	oxygen
ÖNORM	Austrian Standard
PM	permanent magnetic
PMD	paramagnetic detector
PWM	pulse width modulation
rel	relative
sync	synchronisation
st	stoichiometric; steam
SFC	specific fuel consumption
SI	spark ignition
SoC	State of Charge
th	theoretical
TDC	top dead centre
TUG	Graz University of Technology
vol	volumetric
V	volume
WOT	wide open throttle

Affidavit

I declare that I have authored this thesis independently, that I have not used other than the declared sources/resources, and that I have explicitly indicated all material which has been quoted either literally or by content from the sources used. The text document uploaded to TUGRAZonline is identical to the present master thesis.

Ich erkläre an Eides statt, dass ich die vorliegende Arbeit selbstständig verfasst, andere als die angegebenen Quellen/Hilfsmittel nicht benutzt, und die den benutzten Quellen wörtlich und inhaltlich entnommenen Stellen als solche kenntlich gemacht habe. Das in TUGRAZonline hochgeladene Textdokument ist mit der vorliegenden Masterarbeit identisch.

Graz, 23.06.2021

David Retschitzegger

Abstract

For hand-held power tools such as chain saws, leaf blowers and grass trimmers, the two-stroke engine equipped with a carburettor is the preponderant propulsion system. Due to the necessity of reducing CO₂ emissions, the efficiency of such power tools is challenged to be improved. In addition, emission limits will, in all likelihood, become stricter in the future.

As part of the RC-LowCAP research project, the approach of combining a combustion engine and an electric motor to a hybrid system shall be examined, in order to gain fuel consumption and emission benefits. The research project started with a simulation model to determine the optimum powertrain and hybrid configuration for this application. Therefore, load cycles of different hand-held power tools have been investigated to ascertain possible efficiency potentials. Following the initial results of the simulation, a parallel hybrid configuration combining a four-stroke engine and a brushless DC motor was chosen for the experimental investigations. Under those boundary conditions, the aim of this thesis is laying on the design and build-up of a test-bench setup, and on the experimental investigation of the combustion engine and the hybrid system.

At first, a test-bench setup for mounting the combustion engine on the test bench and for connecting the crankshaft to the shaft of the brake was designed and built. After this setup was prepared, measurements with two different ignition systems and two different carburettors were carried out as a preparation step for the hybrid system measurements. The goal of these measurements was to maintain the behaviour of the engine with the implemented changes. The resulting engine maps of those measurements will be used afterwards in this research project to refine the simulation model.

For the hybrid powertrain, a connection was designed and manufactured to join the crankshaft of the combustion engine with the shaft of the electric motor. Subsequently, the first measurements with the hybrid configuration were carried out on the start-up behaviour of the system. The start-up investigations done with the hybrid system could confirm that the start-up of the engine, by powering and controlling the electric motor is possible. After those experiments steady-state measurements were carried out. The resulting efficiency maps from those stationary measurements are compared to efficiency of the combustion engine alone. By this comparison, the hybrid configuration is promising in terms of increasing the efficiency of a hand-held power tool. However, in order to determine whether this potential advantage in the efficiency proves true, load cycles must be driven with the hybrid system. Furthermore, all the gained results from the hybrid powertrain measurements are used after this master thesis for enhancing the simulation model and to investigate possible efficiency benefits.

1 Introduction

In the field of hand-held power tools, a broad majority uses a combustion engine as propulsion system. Those engines possess a high-power-density, but suffer from a high fuel consumption. Due to the necessity of reducing carbon dioxide emissions, much effort is put into research and development of those small combustion engines. Despite the improvements in small combustion engines, a trend in utilizing electric motors as power unit for hand-held tools can be seen. [7],[34]

In this master thesis the approach of combining a combustion engine and an electric motor to gain a hybrid system shall be examined. The focus of this thesis is laying on the design and construction of a test-bench setup, as well as on the experimental investigation of the combustion engine and the hybrid system. This thesis was written within the framework of the RC-LowCAP research project (cf. [17]). In the course of this research project a doctoral thesis is authored, which builds the basis for this master thesis (cf. chapter 1.3).

In the first chapter of this thesis, an overview of the state of the art in hand-held power tools and a brief look at the general framework of the research project is given. Chapter two explains the theoretical background in order to get a better understanding of the content presented in the following chapters. In chapter three the utilised test carriers and controllers are explained. The test-bench setup, starting from the design until the final measuring setup, is displayed in the fourth chapter. Chapter five shows the experimental investigations and the gained results. The conclusions which can be taken from the results and an outlook is outlined in the sixth chapter and seventh chapter of this thesis.

1.1 Objective

The aim of this master thesis is to design and build a test-bench setup for carrying out experiments on a combustion engine and a hybrid system, as well as experimentally characterising the utilised systems. In order to gain those results, the following tasks have been carried out:

- Design of an engine mounting for the test bench
- Manufacturing and assembling of the engine setup
- Preparation and setting up of the engine and test bench for the measurements
- Measurements on the three different engine arrangements:
 - Reference ICE (cf. 5.1)
 - Modified ICE (cf. 5.2)
 - Hybrid system (cf. 5.3)
- Results usability and comparison

1.2 State of the art

In hand-held power tools like chain saws, leaf blowers and grass trimmers the two-stroke engine fitted with a carburettor is the most used propulsion system. The necessity of reducing CO₂ emissions and a shortage in fossil resources leads to the need of improving the engine efficiency. Furthermore, emission limits will become stricter in the future. [34]

The various requirements a hand-held power tool has to fulfil are shown in Figure 1-1. Some of those requirements are in contrast to each other, which proves difficult to the development of hand-held power tools. [34]



Figure 1-1: Requirements on hand-held power tools [34]

As mentioned before, the two-stroke engine is the mainly used propulsion technology in hand-held power tools because of its high-power-density. For some applications, such as leaf blowers and grass trimmers, four-stroke engines can be seen on the market. The four-stroke engine possesses a lower fuel consumption and emissions compared to the two-stroke engine, but has a lack of specific power. [34]

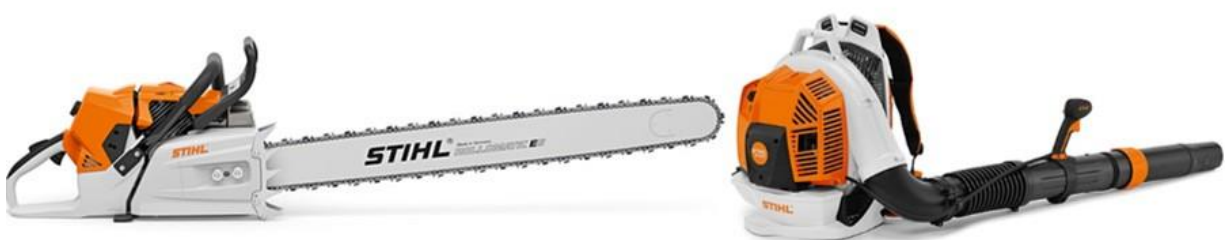


Figure 1-2: Two-stroke powered chainsaw and four-stroke driven leaf blower [25],[26]

For applications, where low noise emissions are required, battery powered tools or electric tools with a power cord are suitable. [8]



Figure 1-3: Electric brush cutter with power cord and battery powered grass trimmer [27],[28]

The biggest power range of hand-held power tools can be seen on two-stroke tools with a range of 0.8 kW to 6.5 kW. Tools powered by a four-stroke engine feature a range from 0.9 kW up to 3.5 kW and electric tools have a power output up to 2.5 kW. [29]

1.3 Boundary conditions

Based on the RC-LowCAP research project group of IVT at the Technical University of Graz, that started in December of 2019, 9 research sub-projects are created (Figure 1-4). In the category of “Tools”, the idea of a hybrid tool is examined as a way to increase the efficiency and reduce the emissions of these applications. As known from the automotive industry, the hybrid powertrain is already a state-of-the-art driver to bring down greenhouse gas emissions from combustion driven powertrains by adding a second power source to the system - the electric energy. [17]







Area	Tools 	Personal Mobility 	Transport 
Fuels 	F1 F-Tool	F2 F-Pers	F3 F-Trans
Hybrid 	H1 H-Tool	H2 H-Pers	H3 H-Trans
Cross 	X1 X-Sens	X2 X-LCA	X3 X-Fuels

Figure 1-4: RC-LowCAP projects [17]

The research on the hybrid tool started with a concept investigation, fully parametric, system-level simulation model in MATLAB and Simulink in order to examine the efficiency potential of different powertrain units, sizes and hybrid configurations for different load cycles. [36]

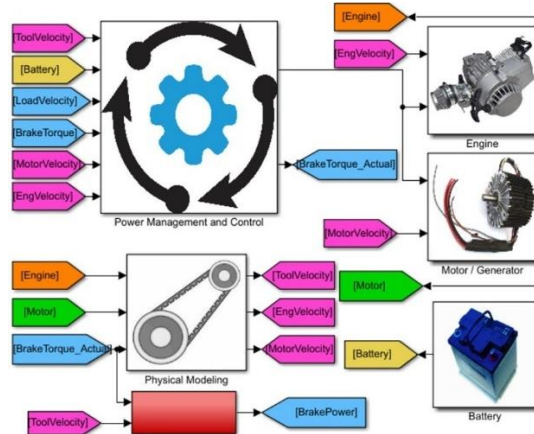


Figure 1-5: hybrid tool simulation model [36]

Figure 1-6 depicts the load cycle of a light load and high transient application in the field use (e.g.: limbing a tree with a chainsaw or cutting thick weeds with a brushcutter). The normalised speed and torque versus the time are shown. In the recorded normalised speed, the average speed is about 83% of the maximum speed (red line). Furthermore, the oscillation magnitude of the speed amounts to 30% and on 20 to 30% of the cycle duration the tool is on idle.

An oscillation magnitude of 100% can be seen in the normalised torque of the recorded load cycle. Moreover, the averaged torque of this hand-held tool in field use is accounting to 55% of the maximum torque (red line).

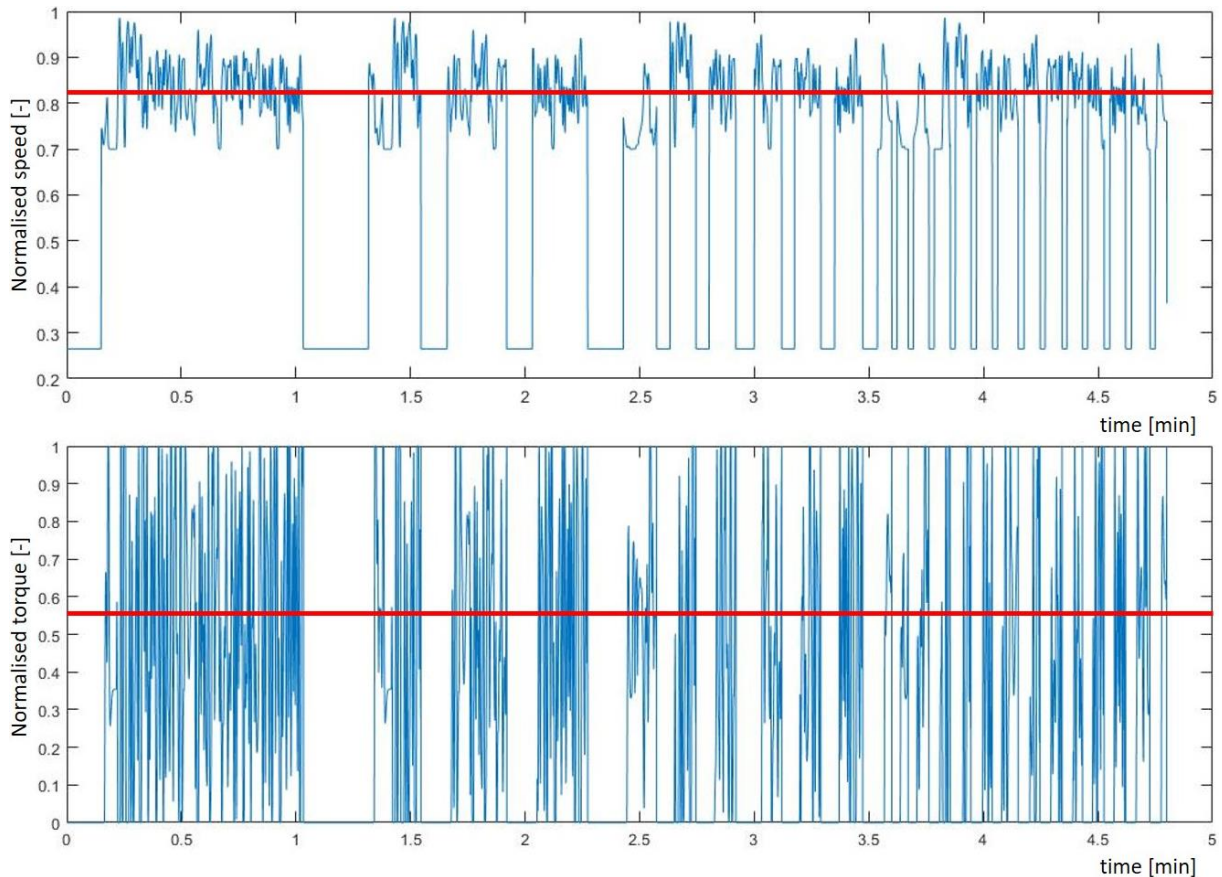


Figure 1-6: Normalised speed and torque of a hand-held power tool [36]

This information gained from the load cycle of such a hand-held power tool led to idea of investigating a hybrid powertrain for such an application.

Due to the high amount of time staying on idle, a potential benefit in the fuel consumption and in reducing the emissions by minimizing the idle time can be seen. Furthermore, the hybrid approach can reduce the high transient speed of the ICE, by the utilisation of the EM as a torque balancer (cf. Figure 1-8). This reduction of the high transient speed may be beneficial to lower the fuel consumption by keeping the ICE on its best efficiency line. By investigating the normalised torque, it can be seen that the oscillations are very high and the average torque amount is about 55% of the maximum torque. This means that for a given load cycle, a downsized ICE combined with an EM can be used according to the operational strategy mentioned below (Figure 1-8).

With those ideas and potential benefits, the hybrid tool simulation started. After the first simulation results (cf. H-Tool simulation paper [36]), comes the powertrain dimensioning in order to build and implement the selected optimum simulation-based hybrid system on the test bench. The powertrain selected for the hybrid tool is combining a 65cc 4-stroke combustion engine with a 1.8kW BLDC Electric Motor from the company STIHL connected on the same shaft in a 1:1 parallel hybrid configuration without any intermediate clutch (pic below). [36]

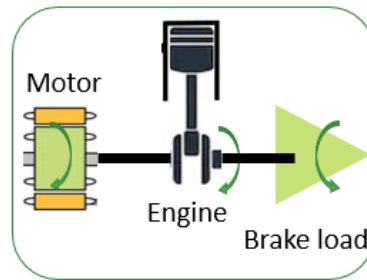


Figure 1-7: Parallel hybrid configuration [36]

The operational strategy of the parallel hybrid system follows the approach of the ICE best operational line. Above a critical speed, the ICE is working at its best operational line and the EM acting as a torque balancer. In this mode the EM is adding or subtracting torque based on the ICE and the applied external load. Below the critical speed, the combustion engine is not producing any torque but is cranked by the EM (i.e.: start-stop function). [36]

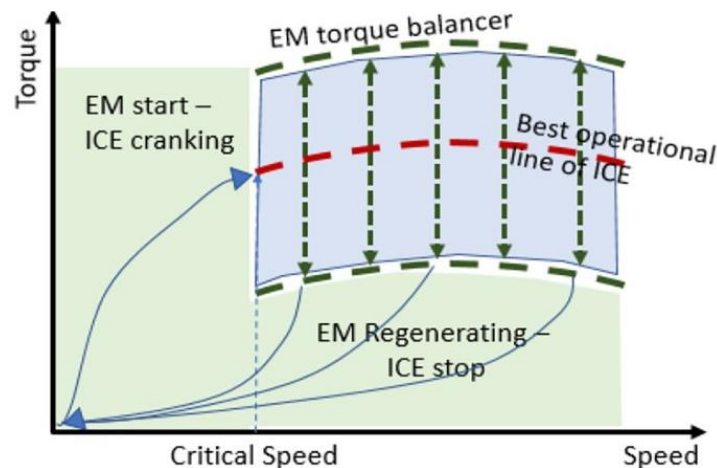


Figure 1-8: Operating strategy for parallel hybrid system [36]

With these constraints, this study aims to design, built and characterize the aforementioned system as a next step of the H-Tool research project targeting for the first experimental data to validate and correct the accuracy of the simulation model.

2 Theoretical Background

In this chapter, the theoretical foundations, necessary for a better understanding of the content of this thesis, are explained. The first subchapter describes the working principle of the four-stroke spark-ignition engine and the specifics of our ICE. In the second subchapter, the brushless direct current motor is delineated. The possible combinations of an ICE and an EM, to gain a hybrid system, are depicted in the third subchapter.

2.1 Four-stroke spark-ignition engine with external mixture formation

2.1.1 Forces ([2],[12],[24])

An internal combustion engine converts the chemical energy stored in the fuel, into mechanical energy, that moves the piston. The reciprocation piston movement is transferred into a rotating motion of the crankshaft via the conrod. On the four-stroke engine two revolutions of the crankshaft are needed to complete one cycle (Figure 2-1).

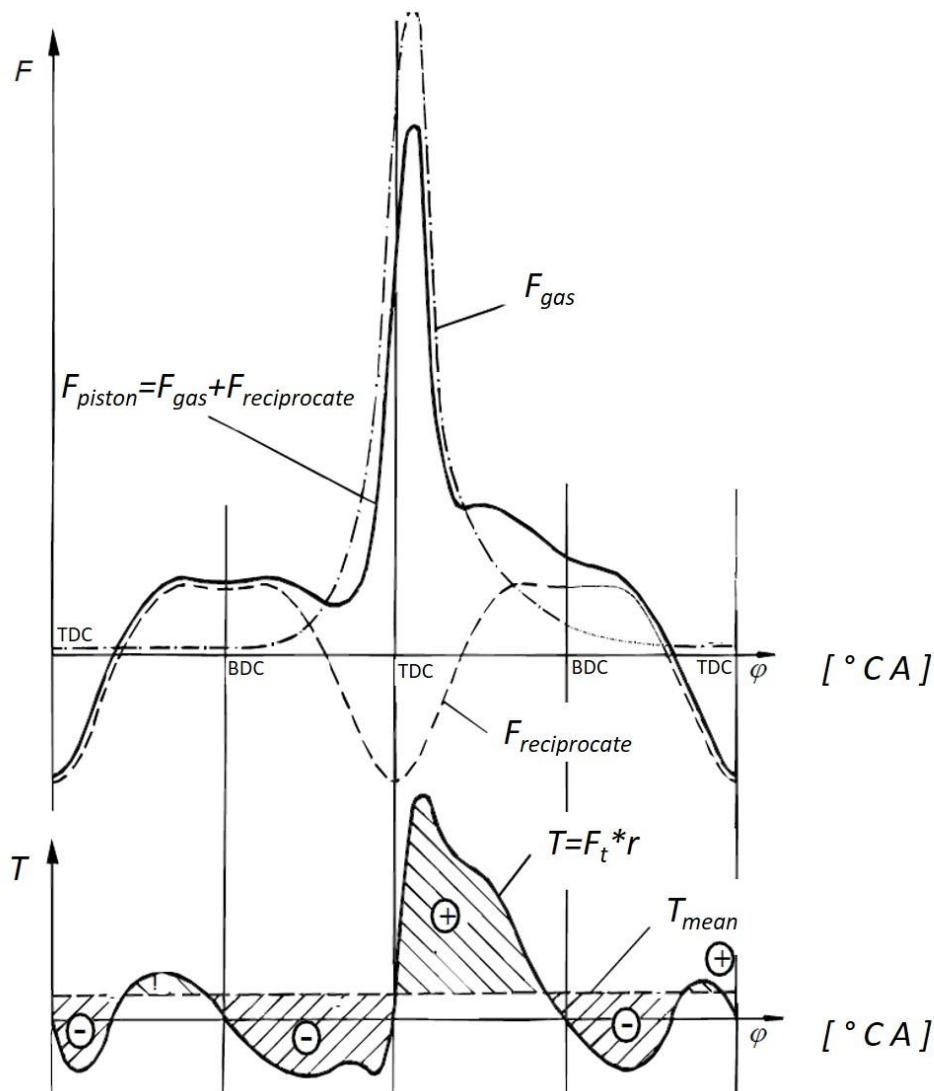


Figure 2-1: Curve of forces and moments vs. CA of a single cylinder four-stroke engine [2]

Figure 2-1 shows the forces acting on the piston F_{piston} and the resulting torque T on the crankshaft via the crank angle for a single cylinder four stroke engine. The forces acting on the piston F_{piston} are a result of the gas force F_{gas} plus the reciprocating inertial forces $F_{\text{reciprocate}}$. The tangential force F_t is a result of the force on the piston F_{piston} and is producing the torque at the crankshaft T . By averaging the torque curve T , the mean torque T_{mean} is gained. Comparing the mean torque T_{mean} with the torque curve T , oscillations can be investigated. A possible way to smoothen those oscillations is to add inertia to the crankshaft (e.g., a flywheel). Multicylinder engines are showing less oscillations and, therefore, a more uniform torque curve.

2.1.2 Mean effective pressure ([33],[35])

The mean effective pressure in general is the output work over the swept volume during one working cycle. There are three different types of mean effective pressure to distinguish. The two key types are the indicated mean effective pressure (*imep*) and the brake mean effective pressure (*bmep*). The third one is the friction mean effective pressure (*fmep*), which is a result of the other two mean effective pressures.

Indicated mean effective pressure

The *imep* is determined from the cylinder pressure over the swept volume during one working cycle.

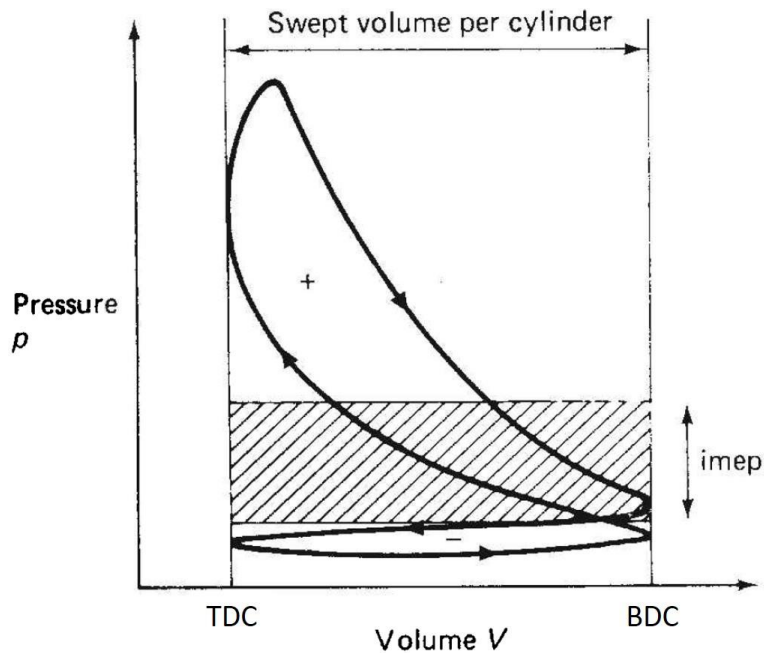


Figure 2-2: Cylinder pressure over swept volume [33]

The cylinder pressure curve is used to derive the gas work at the piston.

$$dW_{\text{piston}} = p_{\text{cylinder}} * A_{\text{piston}} * ds_{\text{piston}} \quad (2-1)$$

With the gas work the *imep* can be calculated.

$$p_{\text{mi}} = \text{imep} = \frac{W_{\text{indicated}}}{V_{\text{swept}}} \quad (2-2)$$

Brake mean effective pressure

The *b MEP* can be determined from the torque at the crankshaft, or from the effective output work of the engine and the swept volume.

$$p_{me} = b MEP = \frac{W_{\text{effective}}}{V_{\text{swept}}} = \frac{T_{\text{crankshaft}} * 4\pi}{V_{\text{swept}}} \quad (2-3)$$

Friction mean effective pressure

The difference between the *i MEP* and the *b MEP* originates from power losses due to mechanical friction.

$$f MEP = i MEP - b MEP \quad (2-4)$$

$$p_{mf} = p_{mi} - p_{me} \quad (2-5)$$

2.1.3 Torque and Power ([2],[35])

The power can be calculated from the mean effective pressure and engine speed (2-6), or from torque and speed (2-7). Vice versa, the torque can be calculated from the power and engine speed (2-8), or from the mean effective pressure and speed (2-9).

$$P = V_{\text{swept}} * p_m * \frac{n}{2} \quad (2-6)$$

$$P = T * 2\pi * n \quad (2-7)$$

$$T = \frac{P}{2\pi * n} \quad (2-8)$$

$$T = \frac{V_{\text{swept}} * p_m}{4\pi} \quad (2-9)$$

Those equations apply, depending on the index, for the effective, indicated or friction power and torque.

2.1.4 Efficiency ([2],[3],[35])

In internal combustion engines a distinction between the indicated, effective and mechanical efficiency is made. The indicated and effective efficiency are determined from the output work and the energy stored in the fuel. This energy stored in the fuel is the product of the net calorific value (NCV, H_u) and the fuel mass (m_{fuel}); $E = H_u * m_{\text{fuel}}$. Furthermore, the efficiency can be calculated from the output power and the fuel mass flow together with the net calorific value.

$$\eta_i = \frac{W_{\text{indicated}}}{H_u * m_{\text{fuel}}} = \frac{P_{\text{indicated}}}{\dot{m}_{\text{fuel}} * H_u} \quad (2-10)$$

$$\eta_e = \frac{W_{\text{effective}}}{H_u * m_{\text{fuel}}} = \frac{P_{\text{effective}}}{\dot{m}_{\text{fuel}} * H_u} \quad (2-11)$$

The mechanical efficiency is the quotient of the effective efficiency and the indicated efficiency.

$$\eta_m = \frac{\eta_e}{\eta_i} = \frac{W_{\text{effective}}}{W_{\text{indicated}}} = \frac{P_{\text{effective}}}{P_{\text{indicated}}} = \frac{p_{\text{me}}}{p_{\text{mi}}} \quad (2-12)$$

2.1.5 Specific fuel consumption ([3],[33],[35])

The specific fuel consumption is inversely proportional to the efficiency and to the net caloric value. Another way to determine the specific fuel consumption is to measure the fuel mass flow and the power output.

$$sfc = b = \frac{1}{\eta * H_u} = \frac{\dot{m}_{\text{fuel}}}{P} \quad (2-13)$$

Similar to the calculations of power, mean effective pressure and efficiency, the specific fuel consumption can be referred to the indicated values or the effective values.

$$isfc = b_i = \frac{1}{\eta_i * H_u} = \frac{\dot{m}_{\text{fuel}}}{P_{\text{indicated}}} \quad (2-14)$$

$$bsfc = b_e = \frac{1}{\eta_e * H_u} = \frac{\dot{m}_{\text{fuel}}}{P_{\text{effective}}} \quad (2-15)$$

The excess air ratio λ has a major effect on the combustion, hence on the specific fuel consumption and the achievable mean effective pressure. Figure 2-3 shows the *bsfc* and the *bme_p* for different excess air ratios at constant engine speed and with a constant throttle angle. The minimum *bsfc* is reached at roughly $\lambda = 1.1$. The maximum *bme_p* is achieved around $\lambda = 0.9$ because of an increased mixture calorific value.

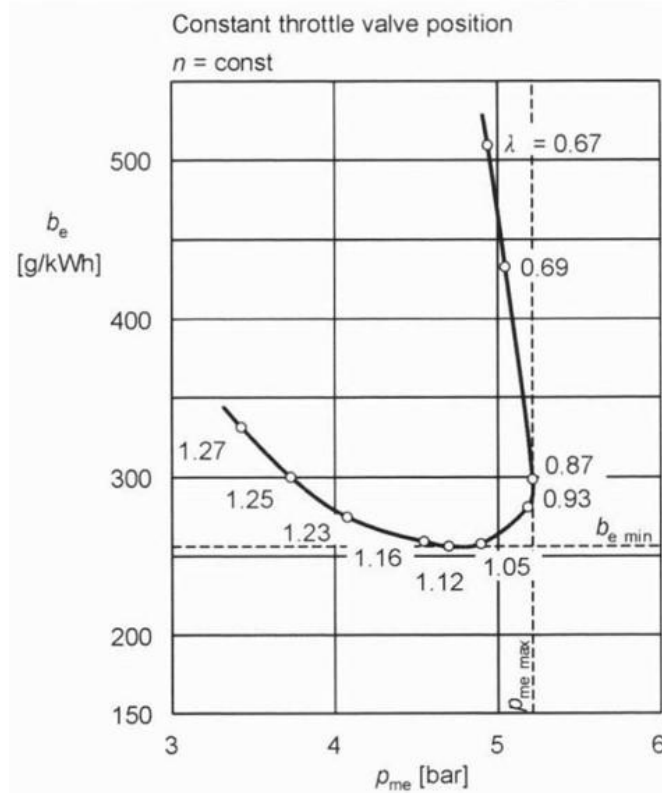


Figure 2-3: *bsfc* and *bme_p* for different excess air ratios [35]

2.1.6 Excess air ratio ([2],[35])

The excess air ratio λ is described by the air mass in the cylinder during the combustion m_{air} and the stoichiometric air mass $m_{\text{air,st}}$. The stoichiometric air requirement L_{St} is calculated from the air mass $m_{\text{air,st}}$ and the fuel m_{fuel} mass under stoichiometric conditions.

$$L_{\text{St}} = \frac{m_{\text{air,st}}}{m_{\text{fuel}}} \quad (2-16)$$

$$\lambda = \frac{m_{\text{air}}}{m_{\text{air,st}}} = \frac{m_{\text{air}}}{L_{\text{St}} * m_{\text{fuel}}} \quad (2-17)$$

2.1.7 Mixture calorific value and air expenditure ([2],[3],[35])

The torque and mean effective pressure of a combustion engine are dependent on the cylinder charge, respectively on the energy contained in the fuel. To calculate this energy, the mixture calorific value H_G is defined.

$$H_G = \frac{m_{\text{fuel}} * H_u}{V_G} \quad (2-18)$$

V_G is the volume of the air fuel mixture and ρ_G the density of the air fuel mixture.

$$V_G = \frac{m_{\text{air}} + m_{\text{fuel}}}{\rho_G} \quad (2-19)$$

$$m_{\text{air}} = \lambda * L_{\text{st}} * m_{\text{fuel}} \quad (2-20)$$

By substituting equation (2-19) and (2-20) into equation (2-18), the following equation is obtained.

$$H_G = \frac{\rho_G * H_u}{\lambda * L_{\text{st}} + 1} \quad (2-21)$$

In Figure 2-4 the heavy influence of the excess air ratio on the mixture calorific value can be seen.

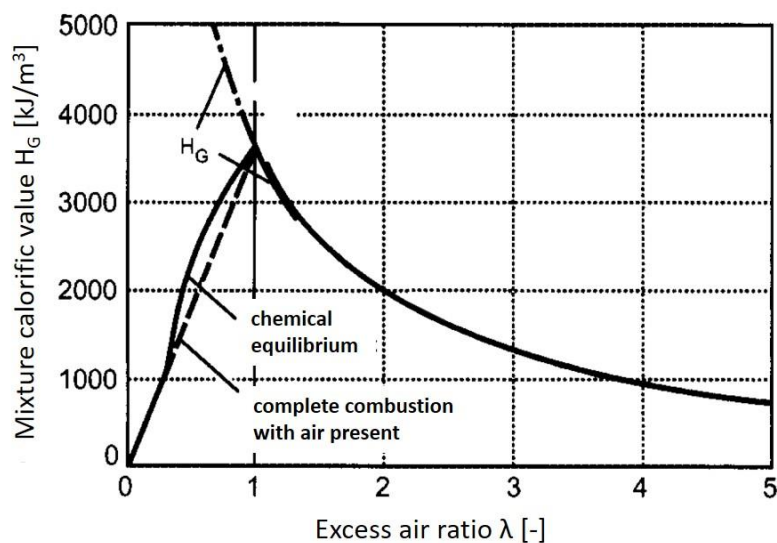


Figure 2-4: Mixture calorific value versus excess air ratio [15]

To characterise the cylinder charge, the air expenditure λ_a is defined. It is a measure for the fresh charge introduced in the engine.

$$\lambda_a = \frac{m_G}{m_{th}} = \frac{m_{fuel} + m_{air}}{m_{th}} \quad (2-22)$$

m_G describes the overall fresh charge mass admitted to the engine. m_{th} is the theoretical fresh charge mass calculated from the ambient pressure and temperature of the charge, and the swept volume of the engine V_{swept} .

The energy stored in the fuel, which is brought into the combustion chamber, is crucial for the output torque and mean effective pressure. This energy can be calculated from the NCV and fuel mass (cf. 2.1.4), or from the mixture calorific value and the air expenditure.

$$E = \lambda_a H_G V_{swept} \quad (2-23)$$

By substituting the equation $W_{effective} = E * \eta_e$ and (2-23) into equation (2-3), the following equation is obtained.

$$p_e = bmep = \lambda_a H_G \eta_e \quad (2-24)$$

This equation exemplifies the upper limits in the $bmep$ for the investigated four-stroke spark-ignition engine with external mixture formation. H_G is heavily influenced by the excess air ratio and λ_a is used to control the engine (cylinder-charge control). The efficiency η_e shall not only be raised to gain a better $bsfc$, but also to reach a higher mean effective pressure.

2.1.8 Combustion process ([2],[3],[33],[35])

According to the working principle (cf. 2.1.1) of SI engines with external mixture formation, the combustion of the mostly homogeneous air fuel mixture is initiated by an electric ignition spark from a spark plug. After the initiation of the combustion, a flame front is forming and propagating until it reaches the combustion chamber wall. In Figure 2-5, a qualitative pressure curve of the high-pressure process is shown. The figure also depicts a cumulative heat release curve (cumulative combustion curve). This curve shows the ratio of the combusted fuel $m_{B,V}$ to the admitted fuel m_B over the crank angle.

The ignition angle and the excess air ratio have a major impact on the heat release characteristic and hence on the pressure curve, the mean effective pressure and on the specific fuel consumption. The ignition angle is usually chosen so that the maximum pressure is reached shortly after the top dead centre (cf. Figure 2-6).

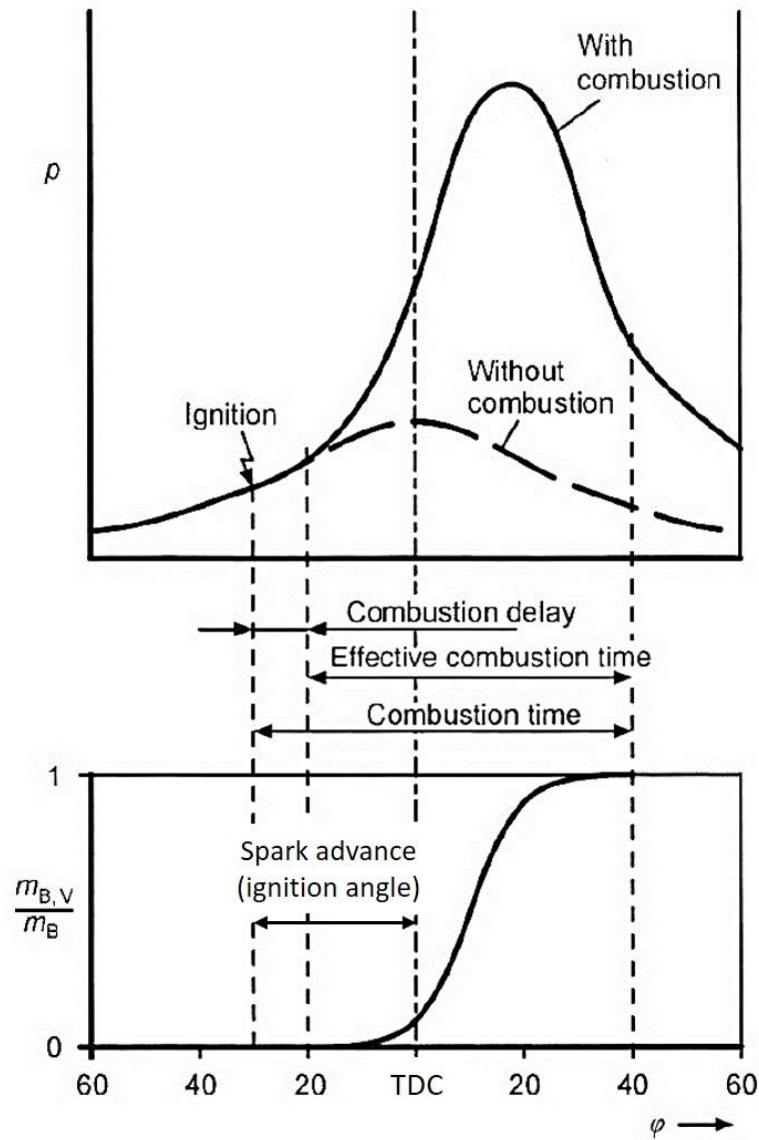


Figure 2-5: Cylinder pressure and cumulative heat release curve [35]

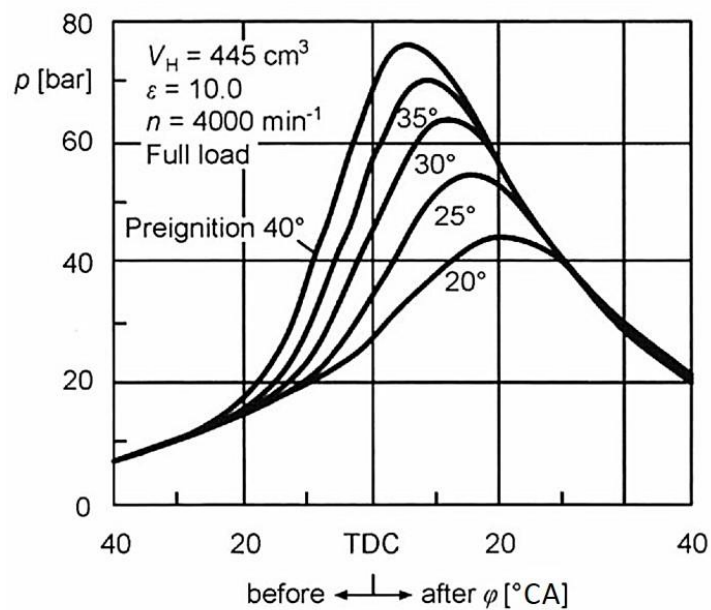


Figure 2-6: Influence of ignition angle on the pressure curve [35]

In Figure 2-7 the influence of the excess air ratio on the specific fuel consumption and the mean effective pressure can be seen. At roughly $\lambda = 1.1$ the minimum *sfc* can be achieved and at a λ around 0.9 the maximum *mep* can be accomplished (cf. 2.1.5).

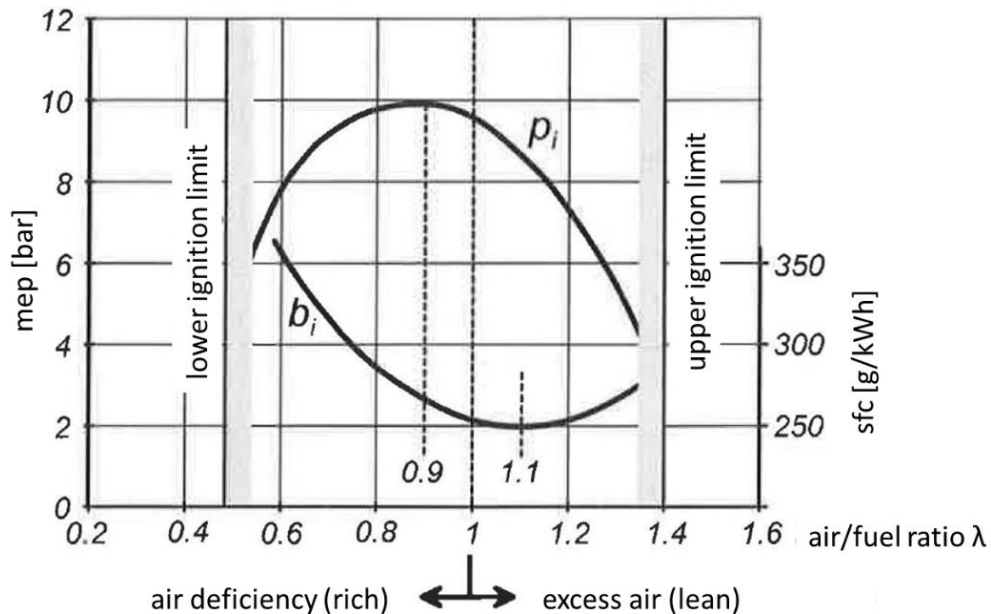


Figure 2-7: Influence of air fuel ratio to mean effective pressure and fuel consumption [2]

In the pressure curve, relatively large cyclical fluctuations can be investigated from working cycle to working cycle. The main reasons for those cyclical fluctuations are temporal and local fluctuations in the turbulent flow resulting in a varying combustion start.

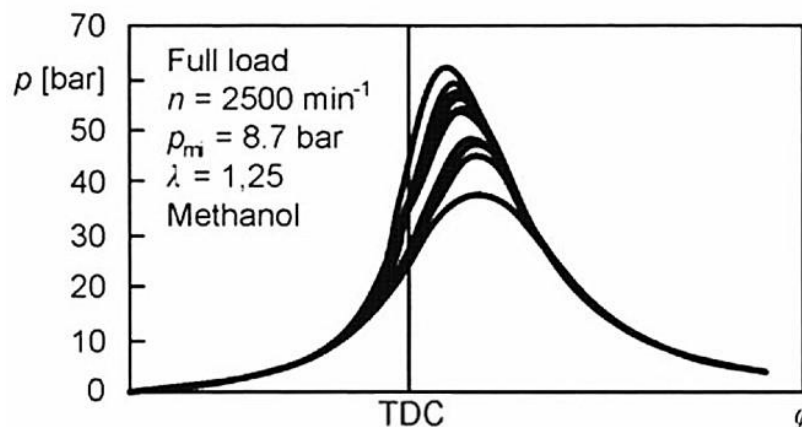


Figure 2-8: Cyclical fluctuations [35]

2.1.9 Exhaust emissions ([2],[3])

The exhaust emissions of SI engines contain, next to the non-toxic components N_2 , CO_2 , H_2O and in case of excess air O_2 , the pollutants CO , HC and NO_x . The concentrations of the pollutants CO , HC and NO_x depend primarily on the air-fuel ratio λ (Figure 2-9). These typical curves are basically found in every SI engine, only the height of the proportions and details of the curve depend on the respective engine and the operating point.

Out of the exhaust emissions the air-fuel ratio can be calculated. The formulas are not presented in this thesis but reference is made to the corresponding publications [1] and [6].

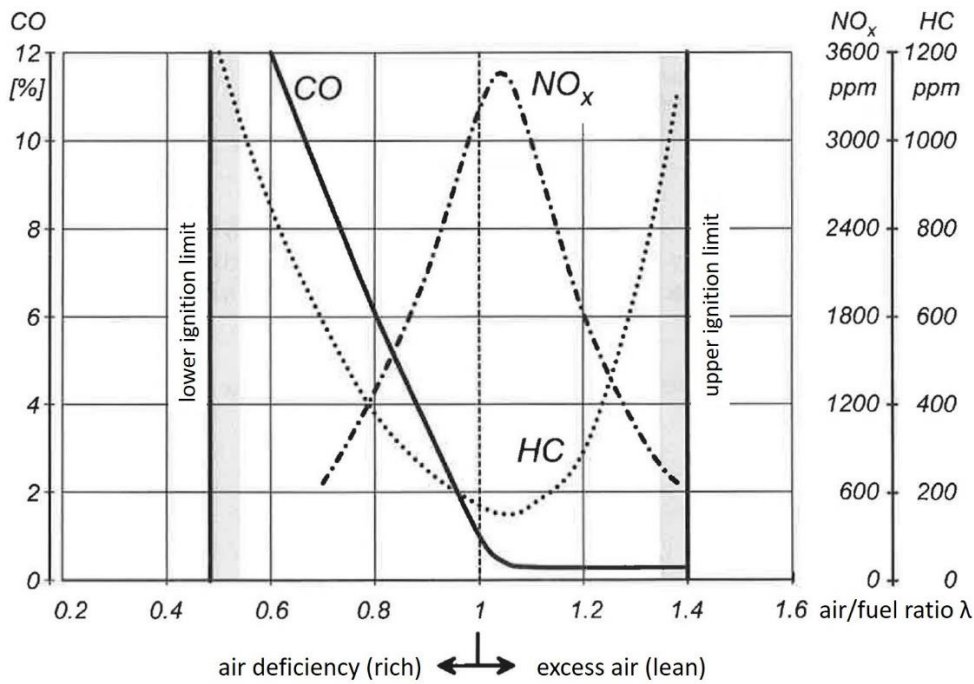


Figure 2-9: Emission behaviour of an SI engine depending on excess air ratio [2]

2.1.10 Mixture formation ([3],[13])

The external mixture formation on hand-held power tools is in most cases done by diaphragm carburettors (Figure 2-10). Those carburettors offer the possibility to work in high inclination angles as well as upside-down. The fuel pump is designed as a diaphragm pump (4) and is driven by the pulsating pressure of the crankcase of the engine. It delivers the fuel to a diaphragm control, consisting of diaphragm (18), control lever (17) and inlet valve (14), which keeps the fuel level in the carburettor constant. Otherwise, the carburettor is equipped with an adjustable main jet (11,13) and an adjustable idle jet (12,14), as well as a cold start device (7). The requirements for such carburettors lie less in maintaining an exact excess air ratio, but more in ensuring operation.

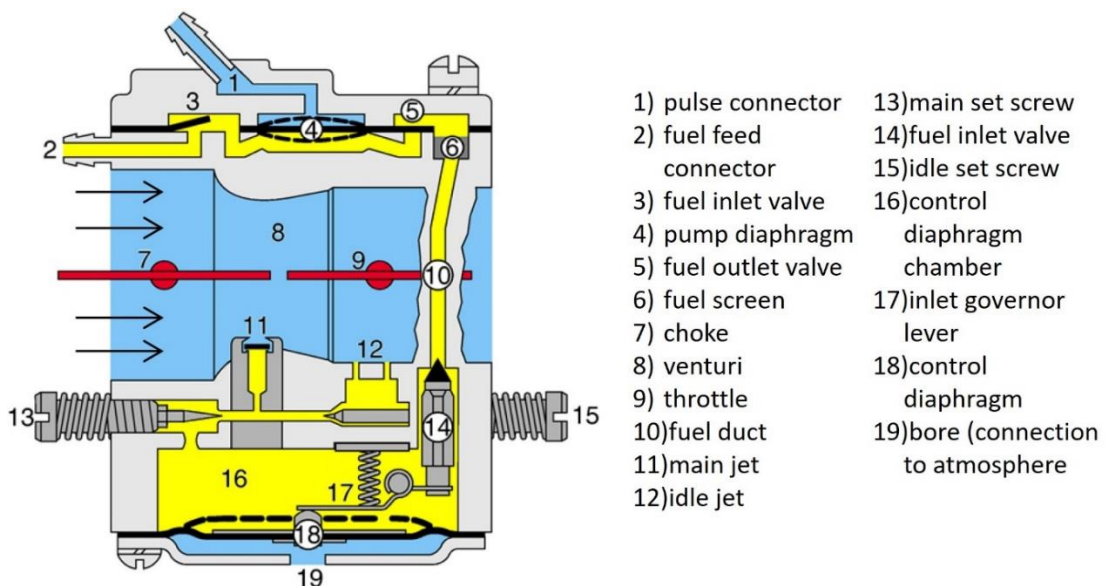


Figure 2-10: Diaphragm carburettor [13]

In order to gain higher controllability of the excess air ratio, STIHL designed an electronically controllable diaphragm carburettor (M-tronic carburettor). In contrast to a conventional diaphragm carburettor, the M-Tronic carburettor eliminates both, the main set screw and the idle set screw. The fuel metering from the control diaphragm chamber into the venturi is controlled via an electronically controllable solenoid valve (1), as can be seen in Figure 2-11.

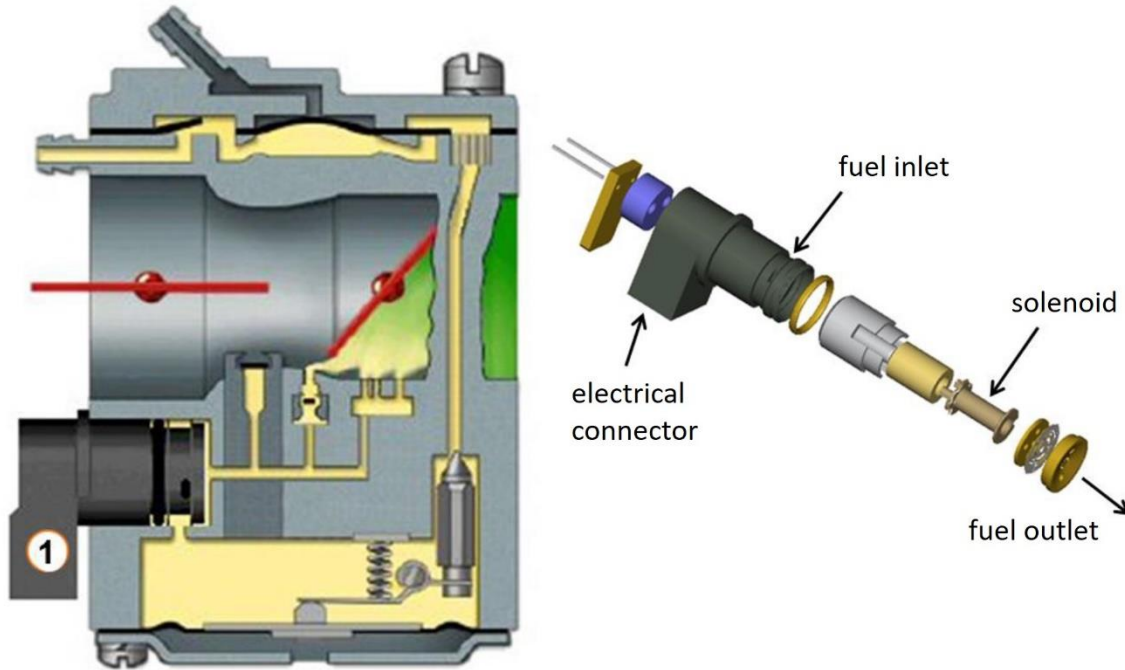


Figure 2-11: STIHL M-tronic carburettor [13]

2.1.11 Ignition ([2],[35])

In SI engines the combustion process is initiated by an electrical discharge. The electrical discharge in the combustion chamber is triggered near the end of the compression phase. An ignition coil is required as high-voltage source and a spark plug is needed as an electrode in the combustion chamber.

The simplest system is the battery coil ignition (Figure 2-12). Before the ignition, the current flows from the battery via the primary winding of the ignition coil and the closed breaker contact to ground, generating a magnetic field in the coil. At ignition time, the breaker contact opens and interrupts the primary current. The breakdown of the magnetic field induces a very high voltage in the secondary winding of the ignition coil, which is fed to the individual spark plugs via the ignition distributor.

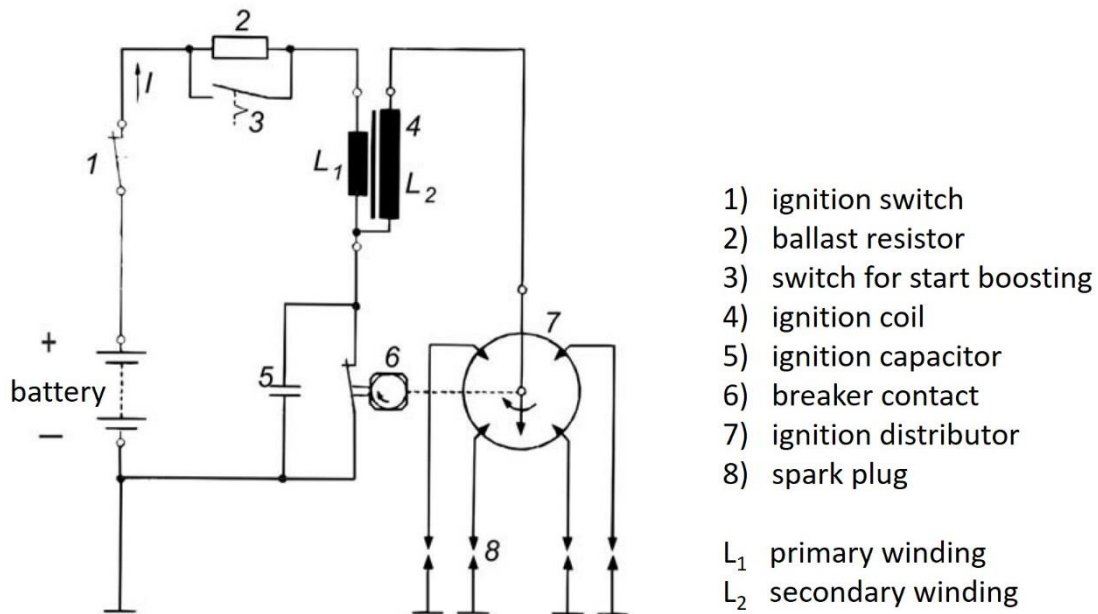


Figure 2-12: Coil ignition [2]

The magneto ignition (Figure 2-13) is used for systems that do not have a battery (hand-held power tools, small engines for mopeds, etc.). The ignition energy is generated by a permanent magnet which rotates at crankshaft speed or at half crankshaft speed. This generates an alternating magnetic flux in the ignition armature with an approximately sinusoidal course, which induces voltage in the primary and secondary windings. Therefore, when the breaker contact is closed, the current flows in the primary circuit. As with battery ignition, this current is interrupted at the moment of ignition and, thereby, generating the ignition voltage in the secondary winding.

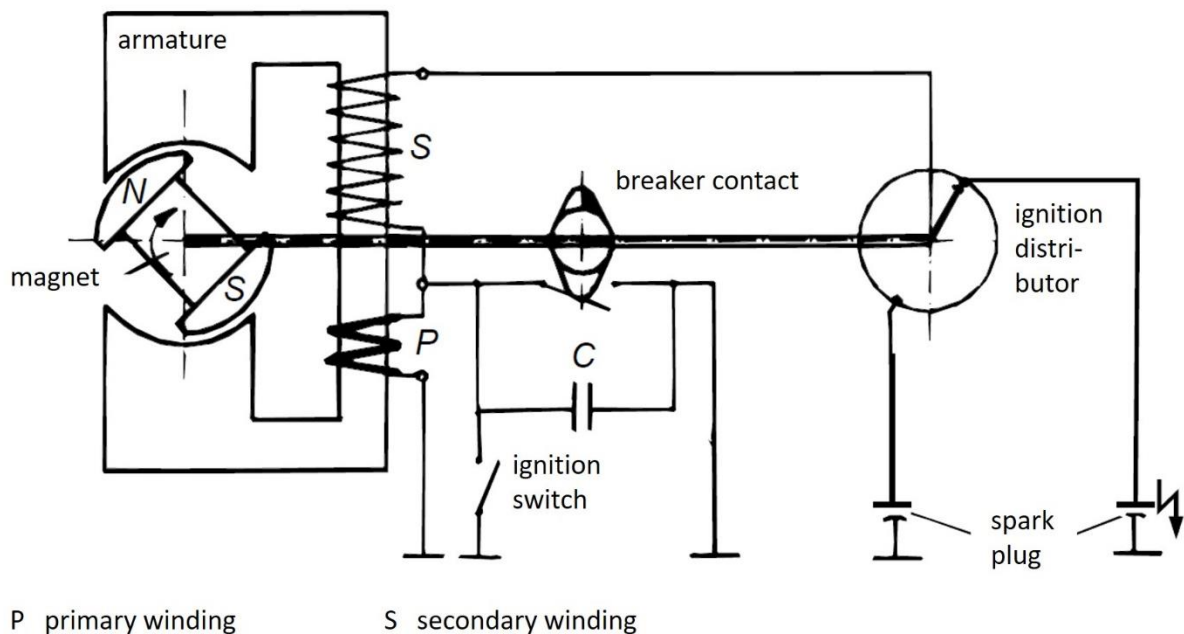


Figure 2-13: Magneto ignition [2]

2.2 Brushless direct current motor ([10],[11],[22],[24])

Brushless DC motors, or more precisely called brushless permanent magnet synchronous motors, possess electromagnets and permanent magnets. The electromagnets are on the non-rotating part of the motor, which is usually in the motor housing for conventional motors, with the permanent magnets on the rotor which is around the motor shaft. Hub motors have the permanent magnets on the rotating part on the outside and the electromagnets on the fixed center part. The electromagnets are on both types organised in groups of three and powered sequentially for the creation of a rotating field to drive the permanent magnets.

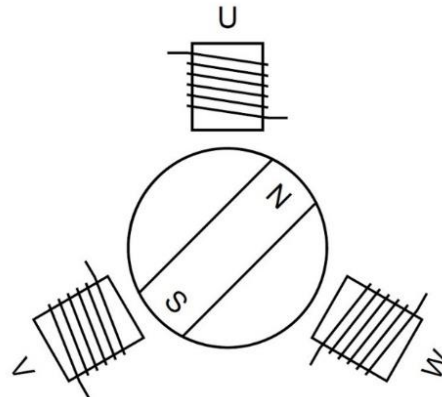


Figure 2-14: BLDC motor [22]

2.2.1 Torque, Power and Efficiency

A current-carrying wire placed in a magnetic field is experiencing a force. This force F is a product of the current I in the wire, the length l of the conductor, and the magnetic flux density B from the magnetic field.

$$F = B * I * l \quad (2-25)$$

In order to generate torque T , the current-carrying conductor is moving in a circular path of the radius r . Hence, the torque characteristic of the motor depends on the number of conductors and on the current flowing through them.

$$T = F * r \quad (2-26)$$

The mechanical power P_{mech} is then calculated from the torque T and speed n . The electrical power P_{el} is a product of the voltage U and the current I .

$$P_{\text{mech}} = T * 2\pi * n \quad (2-27)$$

$$P_{\text{el}} = U * I \quad (2-28)$$

Since every energy conversion has losses, the mechanical power P_{mech} and the electrical power P_{el} are not equal. The ratio of those two is forming the efficiency. Depending if the electrical machine is working as a motor or generator this efficiency is calculated as follows:

$$\eta_{\text{motor}} = \frac{P_{\text{mech}}}{P_{\text{el}}} \quad (2-29)$$

$$\eta_{\text{generator}} = \frac{P_{\text{el}}}{P_{\text{mech}}} \quad (2-30)$$

2.2.2 Number of poles and electrical turn

The number of poles of permanent magnet pairs is an important characteristic of the BLDC motor. If the number of pole pairs is one, then the mechanical turn of the shaft is equal to the electrical turn. In most cases, this number is larger than one and one mechanical turn equals two, three or more electrical turns. One electrical turn is defined as a full 3-phase cycle of the motor electromagnets. This full 3-phase cycle causes the rotor to rotate to the next permanent magnet pole. For a given rate of change on the winding phase, an increase of the pole pairs provokes the motor to spin more slowly.

2.2.3 Commutation

Brushless DC motors do not use, compared to conventional DC motors, brushes for commutating the electromagnets. The commutation instead is done by the motor controller. The controller applies current to each of the three motor windings in sequence to get the rotor spinning. In order to generate a rotating magnetic field in the motor windings, two methods have to be distinguished:

- Trapezoidal commutation
- Sinusoidal commutation

In each of the two commutation methods, a method is provided that detects the actual position of the rotor for synchronisation of the generated rotating field. The actual position is detected by hall sensors, encoders or in a sensorless mode (only for trapezoidal).

2.2.3.1 Trapezoidal commutation

On the trapezoidal commutation, the controller is applying current to two of the three motor conductors. One wire is supplied with current in turn direction, the other with current in alternating direction. The six possible current flow combinations result in a change in the rotors magnetic field every 60 degrees of an electrical turn. In order to apply current to the correct winding, the controller must be aware of the rotor position in relation to the electromagnets. This can be done by using three Hall sensors to detect the position of the rotor. Figure 2-15 shows the state of the Hall sensors and the corresponding direction of the current in each motor winding. Furthermore, in Figure 2-15, the output torque curve can be seen. This torque curve shows six torque ripples per electrical rotation. Those torque ripples are due to the trapezoidal commutation where only two phases at a time are powered and a position information from the Hall sensors is provided every 60 degrees of electrical cycle. At high speeds those torque ripples are less, moreover, the 6-step commutation has a better power density compared to sinusoidal commutation.

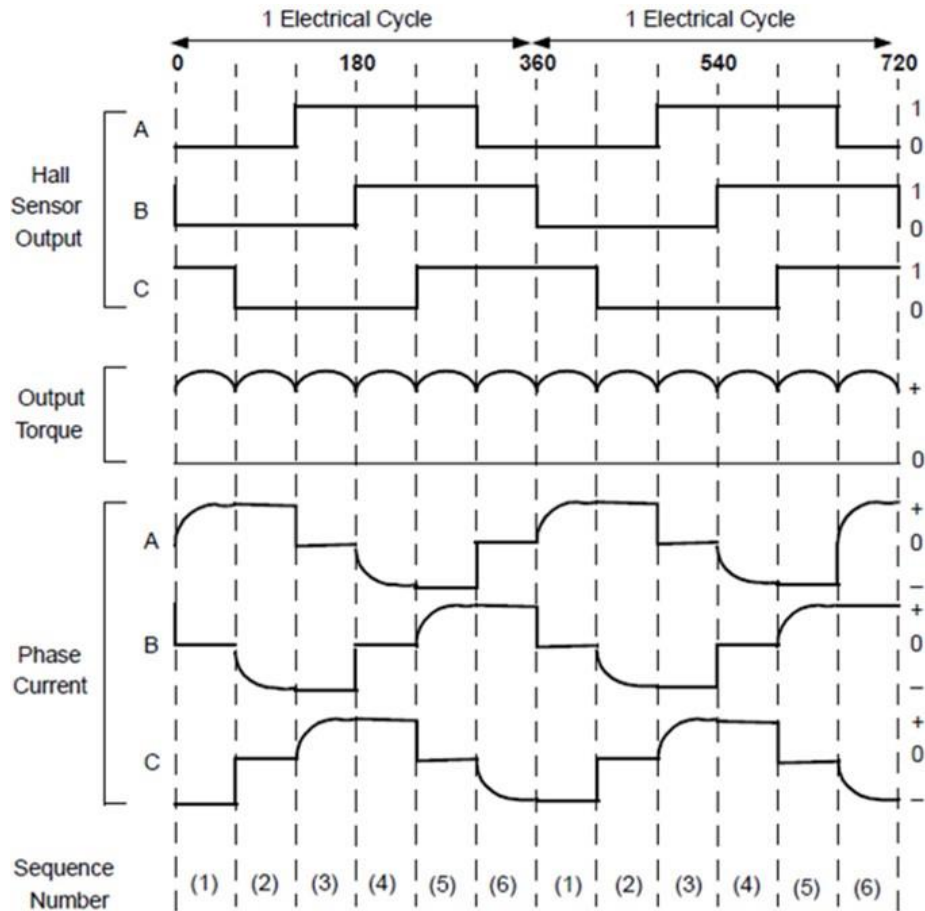


Figure 2-15: Hall sensor sequence, output torque and direction of current [37]

2.2.3.2 Sinusoidal commutation

Since sinusoidal commutation was not examined in this master thesis, reference is made to the literature for further information [22].

2.3 Hybrid drive ([9],[11],[36])

A hybrid drive contains at least two propulsion units, which often have a separate energy supply. In many cases, the hybrid drivetrain is a combination of a combustion engine and an electric drive system. Other possible systems are, e.g., flywheel concepts or air pressure motors. In order to distinguish between the various hybrid configurations, three different categories have become established in the automotive field: the parallel, the serial and the power-split or combined hybrid (Figure 2-16).

2.3.1 Parallel hybrid

On the parallel hybrid systems both, the ICE and the EM, are driving the system. The parallel hybrid can be further categorised, depending on how the ICE and EM are connected, respectively how they are driving the system. In the simplest version, the ICE and EM are directly coupled with the possibility of disconnecting. On some parallel hybrid configurations, the ability to drive the system via the ICE or EM only is given. The main advantages of the parallel hybrid are the compact design, low complexity and high-power-density.

2.3.2 Serial hybrid

Serial hybrid systems feature no mechanical transmission between the ICE and the drive. The ICE is coupled to an EM which is working as an electric generator to charge the ESS. A second EM is powered by the ESS and is driving the system. So, the ESS is working as an energy buffer and as power supply for driving the EM. The main advantage of this system is that the ICE can run on constant speed, thus at its highest possible efficiency.

2.3.3 Combined hybrid (power-split)

The combined hybrid system includes a power-split device, which allows power paths from the ICE and the EM to the drive. Hence, the ICE and the EM can drive independently or synergetically. The idea behind this is to decouple the power demanded from the user of the power supplied by the system. Therefore, the combination of the parallel hybrid and the serial hybrid configuration is possible.

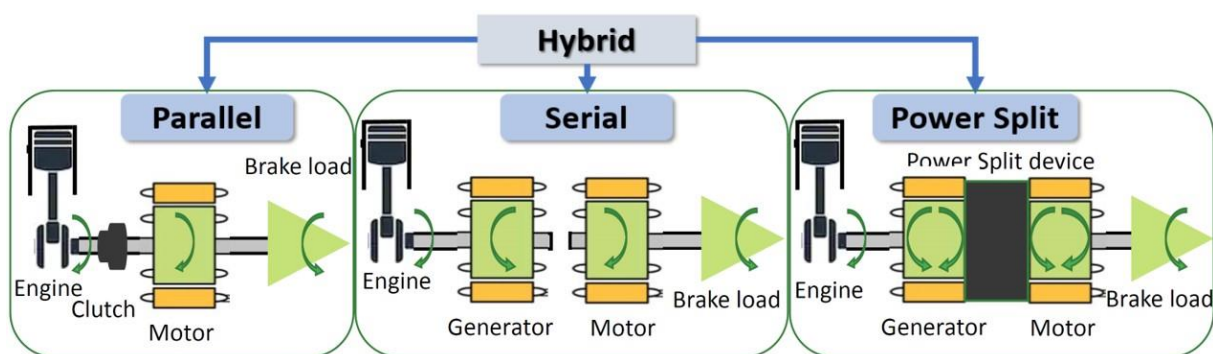


Figure 2-16: Different hybrid configurations [36]

3 Test carrier and controller

In this section, the utilised test carriers and their technical data are presented. Furthermore, the ECUs for controlling the ICE and the EM are described.

3.1 STIHL 4-Mix engine

The utilised combustion engine is a four-stroke spark-ignition engine with external mixture formation out of a leaf blower (Figure 3-1).



Figure 3-1: 4-Mix engine from STIHL BR 600 leaf blower [16]

The engine is equipped with a conventional diaphragm carburettor and a magneto ignition. Unlike conventional four-stroke engines, the STIHL 4-Mix engine is mixture lubricated. Hence, the engine is fuelled with the same gas/oil mixture as conventional two-stroke engines. A complete lubrication of the crank drive is ensured via a special by-pass channel in the cylinder head. [32]

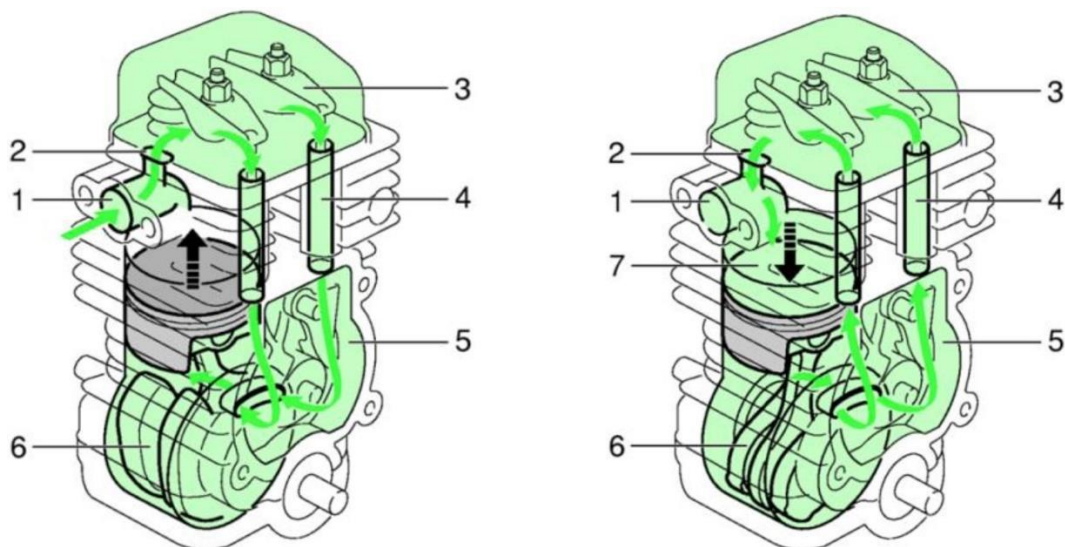


Figure 3-2: Mixture lubrication on the STIHL 4-Mix engine [13]

During the upward movement of the piston (7), a negative pressure is building up in the crankcase (6) (right side in Figure 3-2). The negative pressure is sucking fuel-oil mixture from the carburettor through the intake channel (1) via the by-pass bore (2) into the valve train (3). From the valve train the lubricant enters the crankcase (6) through the channels of the pushrods (4) via the cam wheel housing (5). [13]

If the piston (7) moves downwards, the fuel-oil mixture is conveyed back into the intake port (1) and then into the combustion chamber by the resulting overpressure in the crankcase (left side in Figure 3-2). In this way, the oil constantly circulates in the engine, wetting all moving engine parts and providing appropriate lubrication. [13]

Due to the special crankcase breathing, position-independent operation is possible. In addition, components such as oil pump, oil reservoir, oil pan and oil filter are omitted, which keeps the maintenance effort low compared to conventional four-stroke engines. Only the valve clearance has to be checked from time to time. [13]

The technical data of the ICE is listed below.

cylinder	single cylinder air cooled
displacement	64.8 cc
max. power	2.8 kW
max. speed	9000 rpm
lubrication	mixture lubrication

Table 3-1: Technical data STIHL BR 600 [30]

3.2 STIHL BLDC motor

The used brushless direct current motor is supplied by STIHL (Figure 3-3). The stationary part of the EM, the stator, is in the middle of the motor, the rotating part, the rotor, is on the outside. The technical specifications of the EM are listed in the following table.

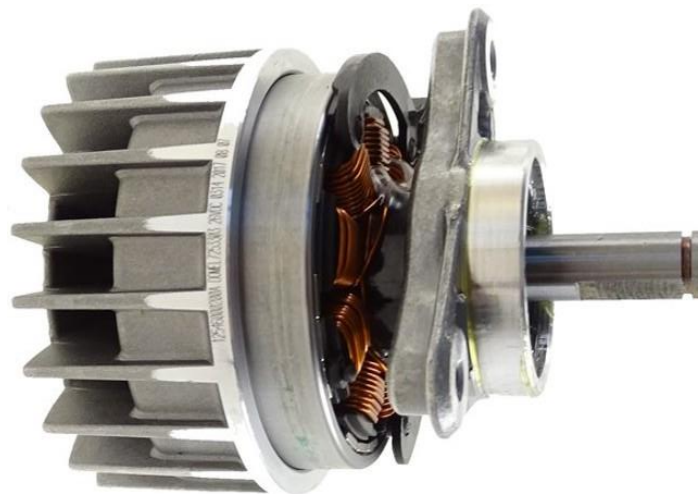


Figure 3-3: BLDC motor supplied by STIHL [5]

configuration	three phases in delta configuration
voltage	36 V
max. power	1.8 kW
max. speed	12000 rpm
number of pole pairs	3
number of windings	9

Table 3-2: Technical data STIHL BLDC motor

3.3 MoTeC

The MoTeC M150 ECU is used to control the modified ICE (cf. 4.2.2), specifically to control the battery coil ignition and the M-tronic carburettor. The ECU has several injector, ignition and auxiliary outputs, as well as different digital and analog inputs. Only a small amount of those capabilities is needed to control the modified ICE.



Figure 3-4: MoTeC M150 [14]

3.4 RoboteQ

The RoboteQ SBL2360 is an ECU for controlling brushless DC motors. The maximum supply voltage is 60 V and the peak output current is 60 A. It uses Hall sensors or Encoders to measure speed and travelled distance. The motor can be operated in different modes (open or closed loop speed mode, position mode or torque mode). It supports trapezoidal and sinusoidal commutation (cf. chapter 2.2.3). [21]



Figure 3-5: RoboteQ SBL2360 [20]

3.4.1 Motor control modes [22]

On the open loop speed mode, the controller gives power proportional to the operator's command. The speed of the motor is not measured, thus, when an external load is applied, the motor slows down.

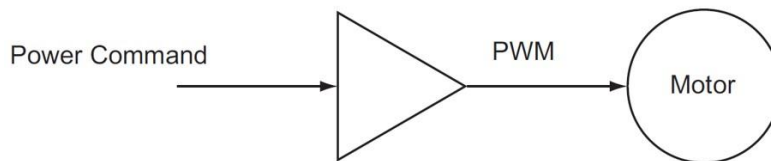


Figure 3-6: Open loop mode [22]

The closed loop speed mode ensures that the operator's requested motor speed is met precisely. If a change in the load occurs, the controller automatically adapts the power output to keep the motor at a constant speed.

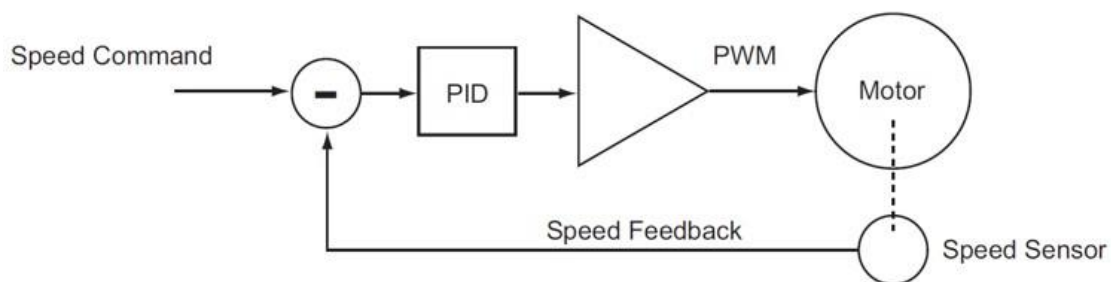


Figure 3-7: Closed loop speed mode [22]

For the closed loop torque mode, the motor is controlled in order to reach the desired amount of torque, with the speed being neglected. This constant torque is achieved by the usage of the motor current for the feedback.

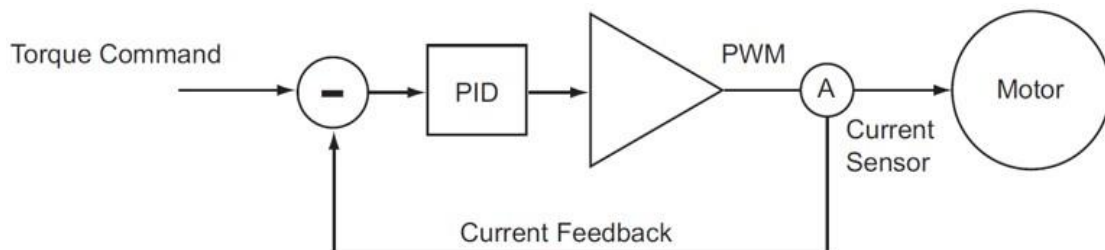


Figure 3-8: Closed loop torque mode [22]

The closed loop position modes are not described in this master thesis, since they were not examined, but reference is made to the literature for further information [22].

4 Test-bench setup

In this chapter, the test-bench setup, starting from the design until the final measuring setup, is displayed.

4.1 Design

4.1.1 Boundary conditions

The goal of this design was a simple engine mounting and connection to the brake that fulfil the following boundary conditions:

- Able to mount the ICE and auxiliary parts
- Able to hold the hybrid system (ICE + EM)
- Simple to manufacture
- Simple height adjustment for alignment of ICE to brake
- Easy accessibility to the engine
- Possibility to implement a cooling system for the ICE
- Low inertia of the rotating parts (coupling parts and clutch)

A centrifugal clutch that disconnects the ICE from the eddy-current brake of the test bench should ensure an easy starting of the ICE. The centrifugal clutch has to disengage while the engine is idling and to engage when the engine is revving up. Furthermore, some damping between the ICE and the eddy-current brake shall smoothen the torsional vibrations coming from the combustion engine.

4.1.2 Three different engine setups

As aforementioned, the design must be able to keep the ICE only configuration, the modified ICE and the hybrid system. All the three different configurations reveal that using the four original engine mounting points is possible (cf. Figure 4-1). Two additional mounting points for the intake box are needed. All six mounting points are roughly on the same plane which opens up the possibility to use a straight plate together with distance bushings for bolting the engine. Furthermore, a cut-out in the mounting plate for the crankshaft is needed (cf. Figure 4-6).

Figure 4-2 displays the differences between the reference ICE and the modified ICE. A change is made from the original diaphragm carburettor to the M-tronic carburettor. The M-tronic carburettor is utilised to gain the possibility of a fuel cut-off which is needed for the operational strategy of the hybrid system (cf. [36]). In addition, the magneto ignition is swapped for a battery coil ignition. The change of the ignition system is done as a preparation step for the hybrid system (see Figure 4-3 incl. the corresponding description above it)

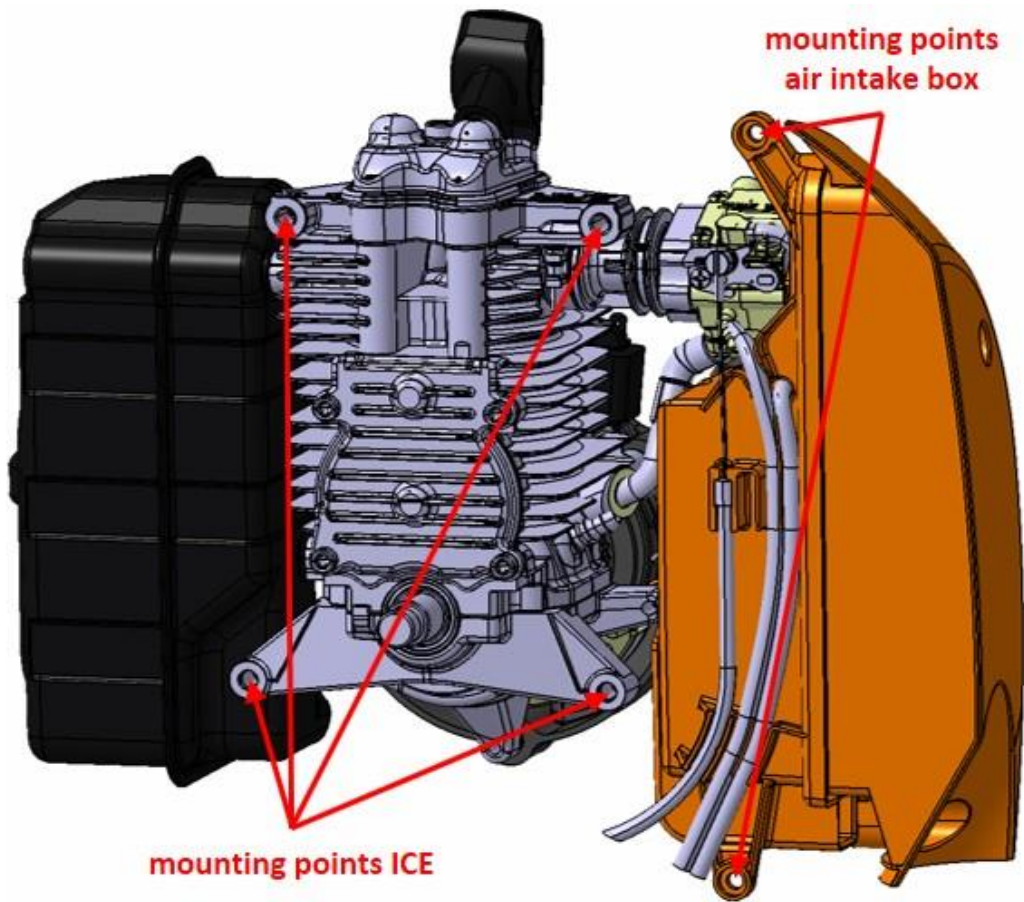


Figure 4-1: Mounting points ICE and air intake box

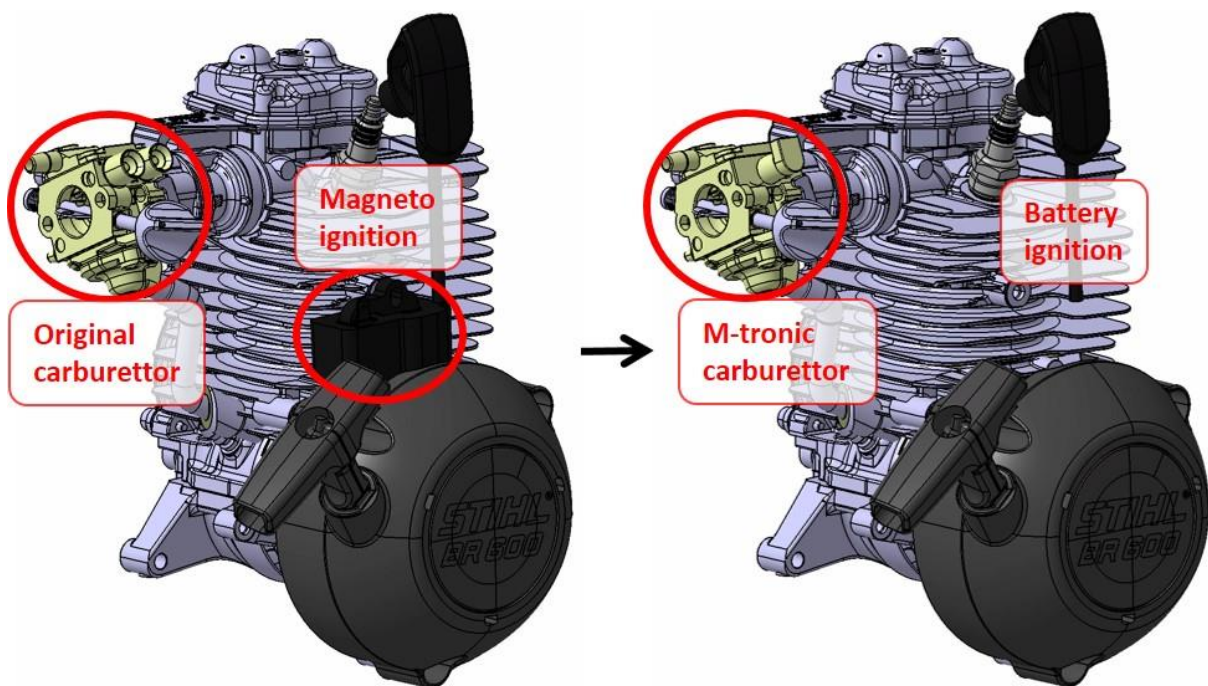


Figure 4-2: Differences between reference ICE and modified ICE

In Figure 4-3, the required changes for joining the EM with the ICE are shown. In order to mount the EM rotor on the crankshaft, the pull starter and the flywheel are removed. Since the removed flywheel, together with its permanent magnets and the removed ignition module, are generating the energy for the ignition system, the magneto ignition system can no longer be used. Due to this, the change to the battery coil ignition was inevitable for the hybrid system.

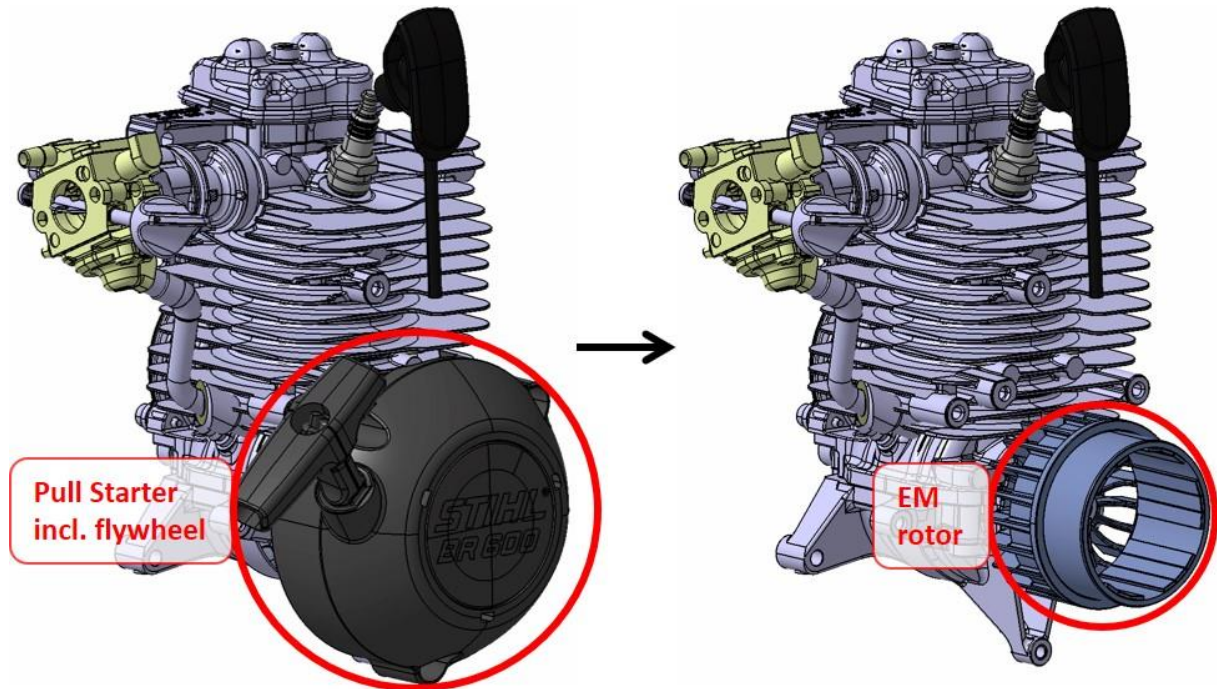


Figure 4-3: Changes from modified ICE to hybrid system

4.1.3 Test bench

The test bench is equipped with an eddy-current brake for breaking the torque of the ICE, respectively the torque of the hybrid powertrain. A threaded plate enables the installation of the engine mounting plate, as well as the fixation of auxiliary parts. An alignment part from another project was already bolted to the threaded plate and should stay in position.

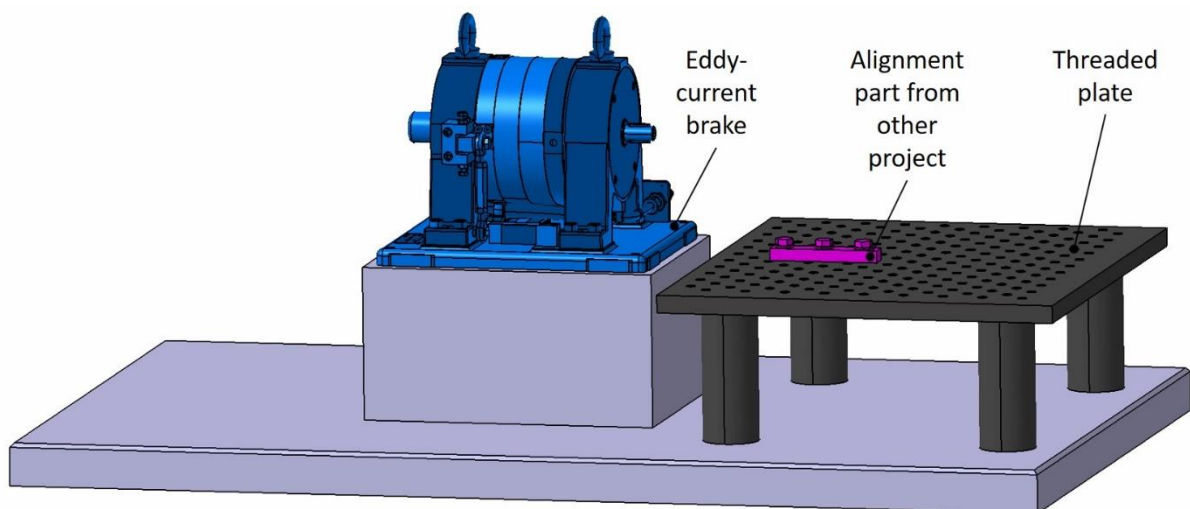


Figure 4-4: Test bench

The eddy-current brake and the threaded plate are fixed and cannot be moved. Those frame conditions led to the following design for setting up the engine on the test bench.

4.1.4 ICE mounting plate

As mentioned in chapter 4.1.2, the possibility to use a simple straight plate for mounting the engine is given. Another plain plate is building the base plate. Two additional stiffening plates reinforce the ICE mounting assembly (Figure 4-5). An opening in the mounting plate allows the crankshaft to pass through. This opening was enlarged to gain more space for the cooling fins. Due to the alignment part from another project that has to stay on the test bench (Figure 4-4), a cut out in the base plate was made. In Figure 4-6 the cut out in the base plate together with the alignment part are depicted.

All four plates have been cut by water jet cutting and welded into a robust structure for carrying out the measurements.

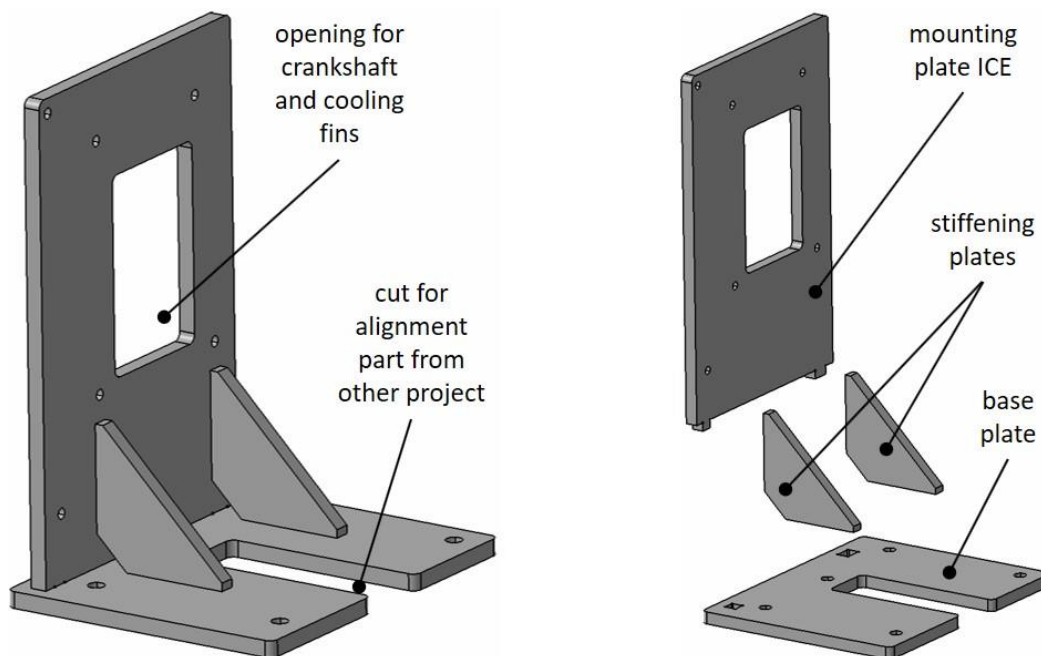


Figure 4-5: Assembly for mounting the ICE

Four bolts are screwed to the base plate to enable a height and angular adjustment of the ICE relative to the test bench. After adjusting the assembly, the four bolts are secured against self-loosening with locking nuts (Figure 4-6).

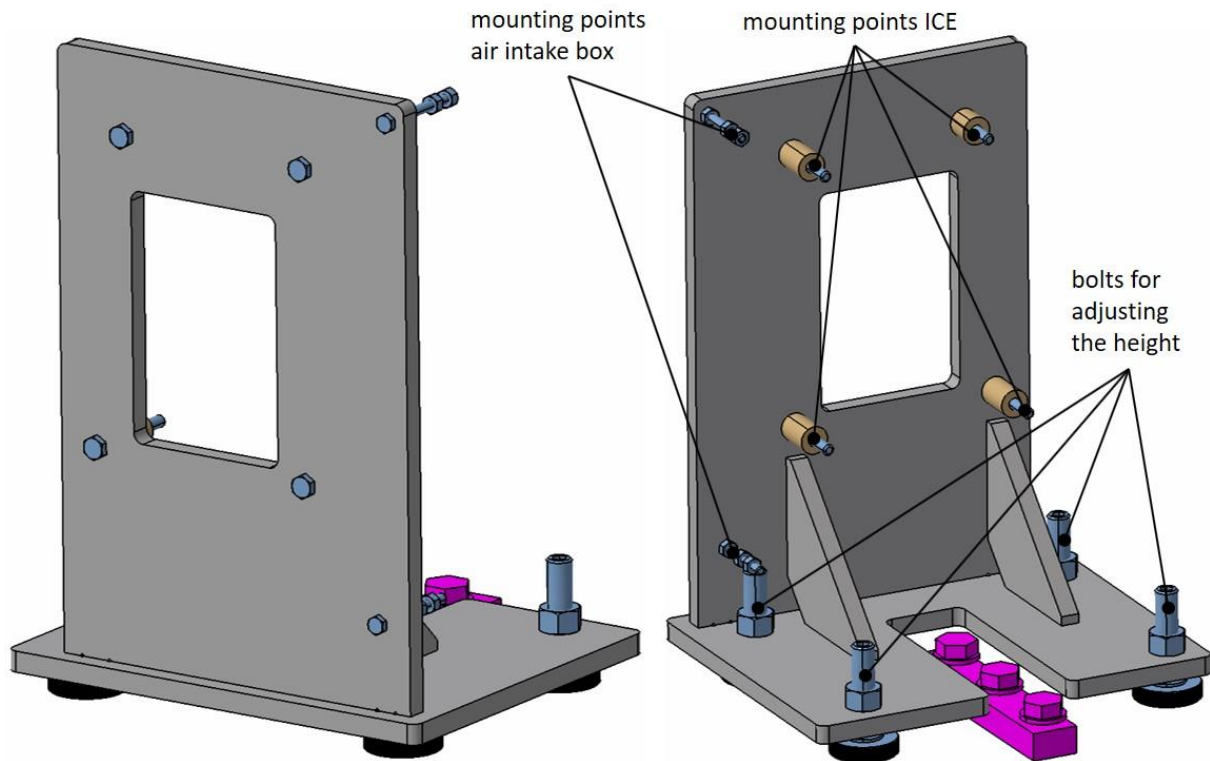


Figure 4-6: Assembly for mounting the ICE (incl. bolts)

Figure 4-7 presents the test bench together with the ICE mounting assembly. The assembly is able to move on the threaded grid plate to enable an easy alignment of the ICE. The crankshaft of the ICE and the shaft on the eddy-current brake are aligned so that they meet on the same axis. Once the whole assembly is aligned, it is clamped to the threaded grid plate with four clamping claws.

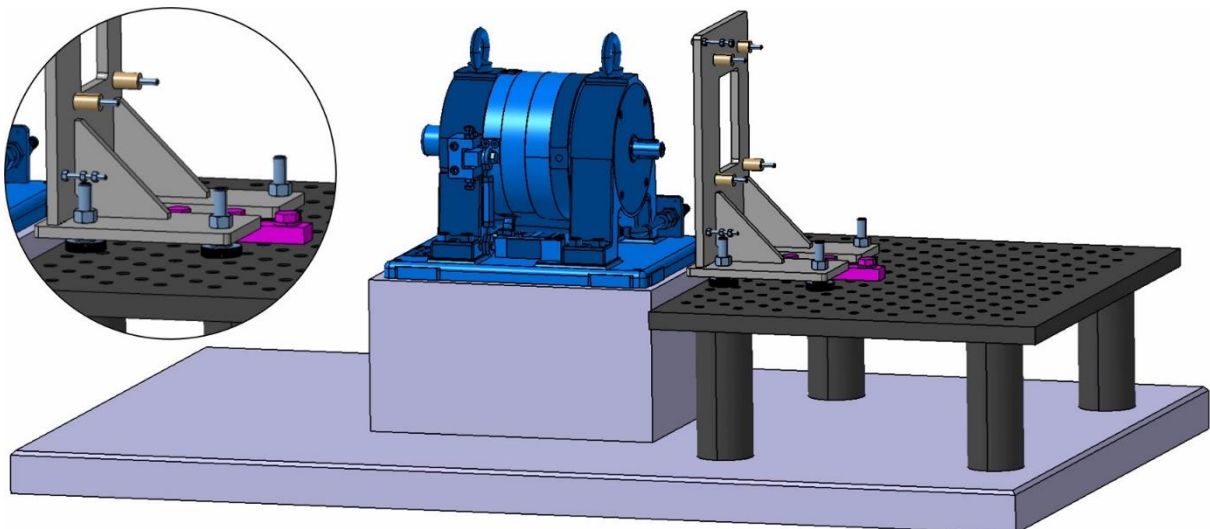


Figure 4-7: Test bench together with ICE mounting assembly

Figure 4-8 shows the ICE installed on the test bench. It can be seen that the shaft of the ICE and the shaft of the eddy-current brake are aligned in order to be coaxial.

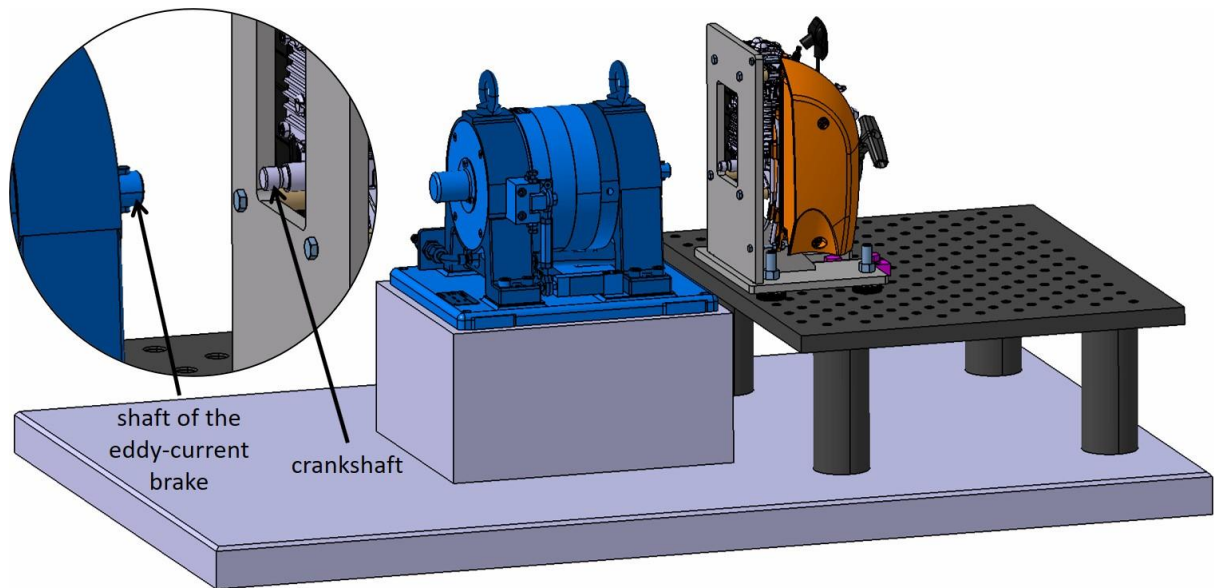


Figure 4-8: Test bench together with ICE

In Table 4-1, the bill of materials for this subassembly can be seen. The three different mounting plates are fabricated by water jet cutting. The further manufacturing steps and the welding of the parts were done in-house. Together with the ICE, the bolts and distance bushings, this is forming the first subassembly.

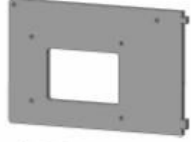




Num	Name	Quantity	Manufacturing	Material	Weight [g]	Comments / Pictures
1	BR 600 asm	1				
2	mounting plate 01	1	water jet cutting	steel	3620	
3	mounting plate 02	1	water jet cutting / thread	steel	2729	
4	mounting plate 03	2	water jet cutting	steel	301	
5	distance bush small	1	lathe	steel	17	
6	distance bush large	3	lathe	steel	26	
7	hexagon head screw M6 x 40	1		steel		DIN EN ISO 4014
8	hexagon head screw M6 x 50	3		steel		DIN EN ISO 4014
9	support screw M12 x 49	4		steel		testbench
10	nut M12	4		steel		DIN EN ISO 4032
11	hexagon head screw M5 x 50	2		steel		DIN EN ISO 4017
12	nut M5	6		steel		DIN EN ISO 4032

Table 4-1: BOM – ICE mounting plate

4.1.5 Connection between the crankshaft and the eddy-current brake

The crankshaft and the shaft of the eddy-current brake need to be connected in order to transfer the torque of the ICE, respectively the hybrid system. To ensure an easy start of the ICE with the pull starter, a centrifugal clutch is installed between the two shafts. This centrifugal clutch is also used on the hybrid system for the same reason of easy starting. The clutch must disengage the two shafts while the engine is idling and engage when the ICE is revving up.

Due to torque ripples generated by the internal combustion engine, a damper which smoothens the torsional vibrations is needed. The damping device is required to transfer the nominal and peak torque of the system, but also to have low inertia. Considering those requirements, an elastomer jaw coupling made out of aluminium is used.

In Figure 4-9 the clutch assembly (connection between the ICE and eddy-current brake) is depicted as exploded drawing.

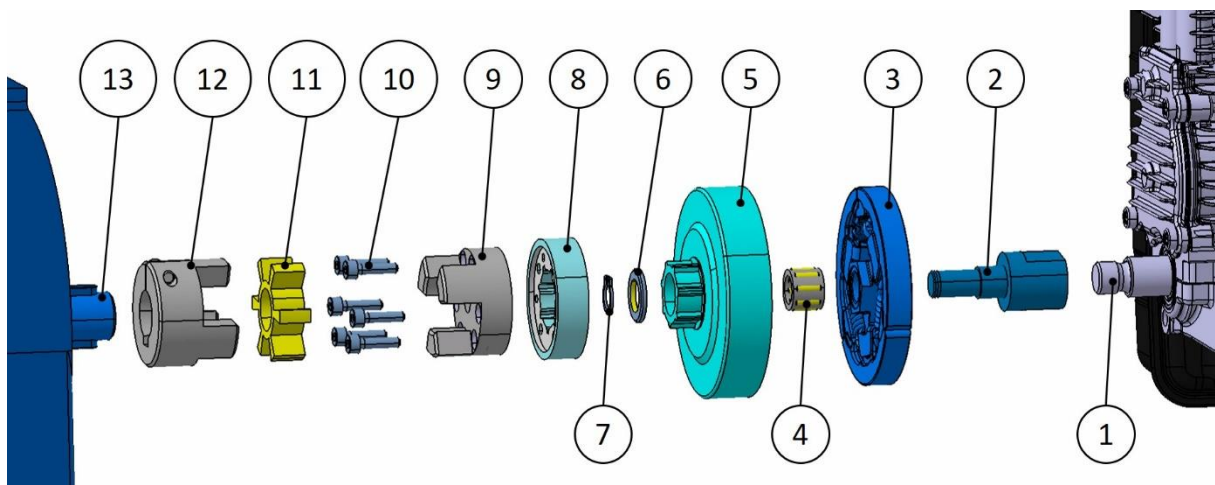


Figure 4-9: Connection between crankshaft and eddy-current brake

The one end of the crankshaft (1) has a right-handed thread, usually used for mounting the blower wheel of the tool. The centrifugal clutch (3), the needle bearing (4) and the bell housing (5) are parts from a chainsaw, provided by STIHL. In order to assemble those parts, an adaptor (2) was manufactured. The adaptor (2) is screwed to the crankshaft (1) and the centrifugal clutch (3) is screwed to the adaptor. Since the crankshaft (1) has a right-handed thread and the centrifugal clutch (3) is provided with a left-handed thread, the clutch (3) and the adaptor (2) are in addition welded together to prevent self-loosening. The bell housing (5) and the needle cage assembly (4) run directly on the adaptor (2). A washer (6) and a circlip (7) impede that the bell housing (5) can detach from the adaptor (2).

To join the bell housing (5) with the jaw clutch (9), an adaptor part (8) is needed because of the spline-shaft profile of the bell housing. This adaptor part (8) is manufactured by wire eroding to fit exactly to the spline-shaft profile of the bell housing (5). A shoulder for centering and six threads for bolting the jaw clutch (9) are machined in the adaptor part (8). Six boreholes laying on the same pitch circle are machined in the jaw clutch (9). The jaw clutch (9) is then bolted to the adaptor part (8) with cylinder head screws (10). The other jaw clutch (12) is featured with a feather key groove and a clamping bolt to mount it directly on the shaft of the eddy-current brake (13). The two jaw clutches (9, 12) are then connected with the elastic spider (11) to transfer the torque and to smoothen torsional vibrations.

Figure 4-10 shows the assembled connection between crankshaft and eddy-current brake.

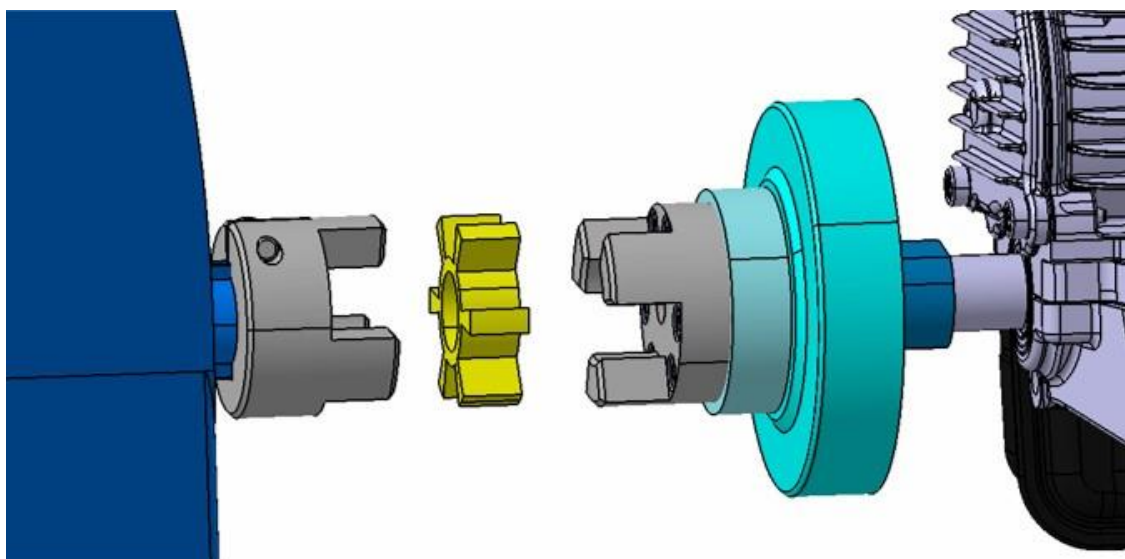


Figure 4-10: Connection between crankshaft and eddy-current brake (assembled)

In Table 4-2, all the parts needed for the small clutch assembly are shown. The centrifugal clutch, the bell housing and the needle bearing are all parts provided by STIHL. The adaptor was manufactured in-house. In order to meet the required tolerances of the spline-shaft profile for the adaptor part that fits on the bell housing, this part was manufactured by wire eroding. Further manufacturing steps on this part and the elastomer jaw coupling were done in-house.

Num	Name	Quantity	Manufacturing	Material	Weight [g]	Comments / Pictures
1	clutch bell housing	1				
2	clutch	1				
3	needle cage 10x16x12	1				
4	washer 10	1		steel		DIN EN ISO 7090
5	circlip 10	1		steel		DIN 471
6	adaptor	1	lathe, mill	steel	70	
7	adaptor to clutch bell housing	1	wire eroding / lathe, thread	steel	94	
8	elastomer jaw coupling GWE 5103-19 with elastomer spider - 98 SH A (red)	1	lathe, drill	aluminium & poly- urethane	120	
9	elastomer jaw coupling GWE 5102-19 with elastomer spider - 64 SH D-H (green)	1		aluminium & hytrel	53	
10	elastomer spider - 98 SH A (red) for elastomer jaw coupling GWE size 19	2		poly- urethane		
11	elastomer spider - 64 SH D-H (green) for elastomer jaw coupling GWE size 19	2		hytrel		
12	cylinder head screw M4 x 16	6		steel		DIN EN ISO 4762

Table 4-2: BOM – small clutch assembly

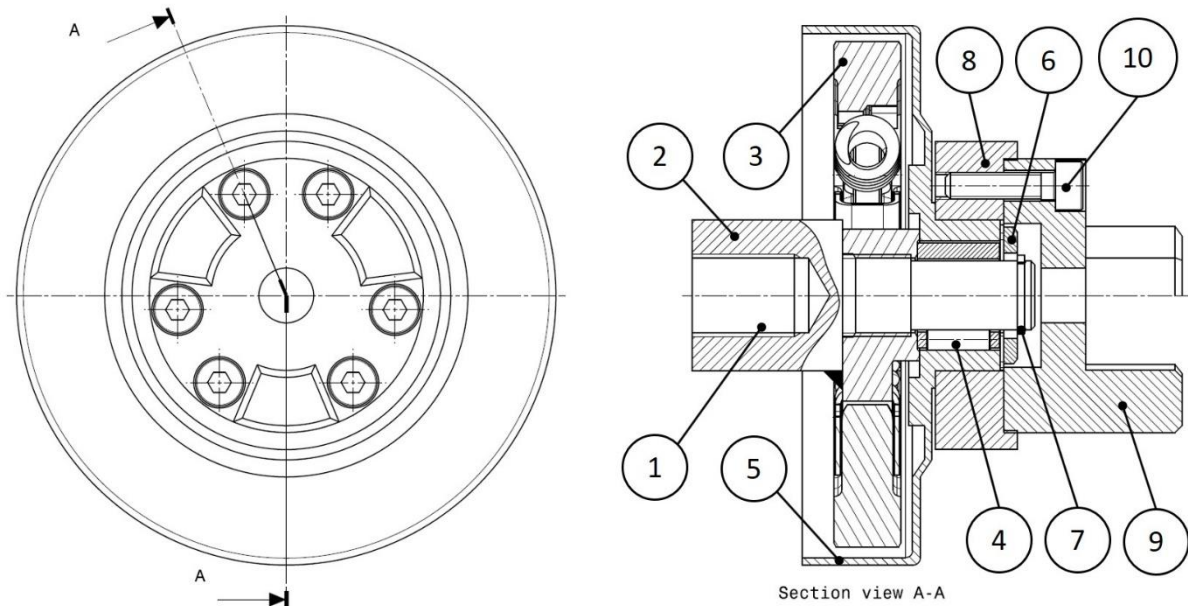


Figure 4-11: Sectional drawing of the clutch assembly

In Figure 4-11, a sectional drawing of this clutch assembly can be seen. The numbering corresponds to the numbering in Figure 4-9.

By means of the sectional drawing, the torque flow of the clutch assembly can be explained. In the right sectional drawing in Figure 4-12 the torque flow from stall till idle speed is displayed. Idle speed is around 2500 rpm. At 3500 rpm the centrifugal clutch (3) starts to engage with the bell housing (5). At 5000 rpm the centrifugal clutch is fully engaged and the torque is transferred to the eddy-current brake (left side in Figure 4-12).

Up to idle speed only the adaptor (2), the centrifugal clutch (3) and the needle bearing (4) are spinning. Therefore, no torque is transmitted to the eddy-current brake. From 3500 rpm upwards the centrifugal clutch starts to engage and to transfer torque to the brake. This means that the centrifugal clutch (3) starts to interact with the bell housing (5). The bell housing (5) has a rigid connection to the adaptor part (8). On the adaptor part (8) the jaw clutch (9) is flange-mounted with six bolts (10) and transfers the torque with the aid of the elastic spider (11) and the jaw clutch (12) to the eddy-current brake (13).

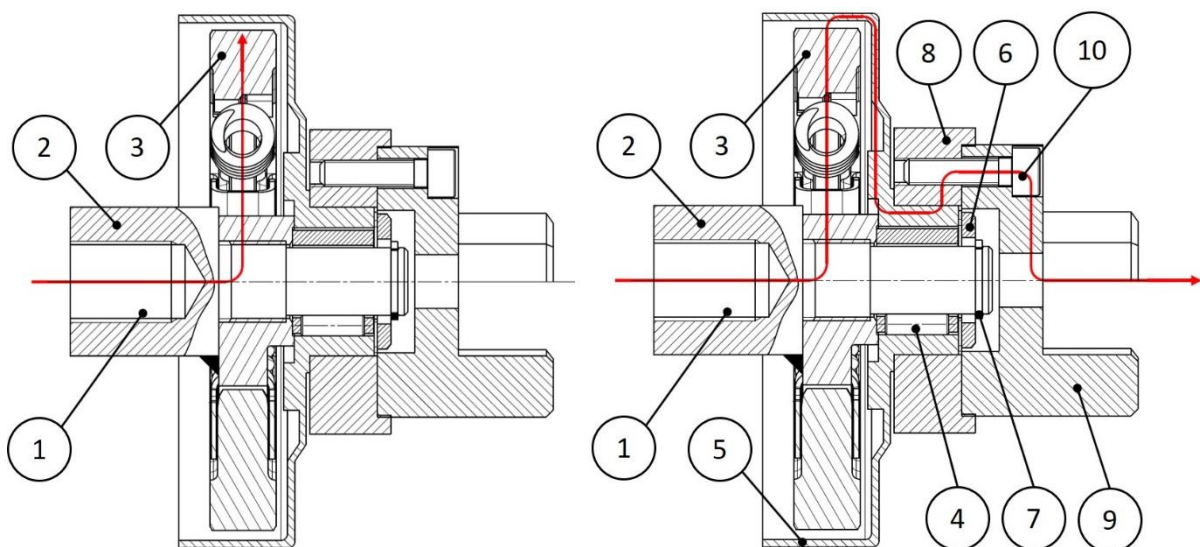


Figure 4-12: Sectional drawing of the clutch assembly including the torque flow

As mentioned above, the elastomer jaw coupling is required to transfer the nominal and peak torque of the system, but also to have low inertia. The low inertia opens up the possibility to drive dynamic load cycles. This was not examined in this master thesis, but the design has to fulfil this requirement (cf. chapter 1.3). To gain this very low inertia, the smallest possible elastic jaw coupling was chosen (left side in Figure 4-13). Since this first design of the elastomer jaw coupling had to be made with a very small safety margin, a second design with a bigger elastomer jaw coupling was prepared (right side in Figure 4-13).

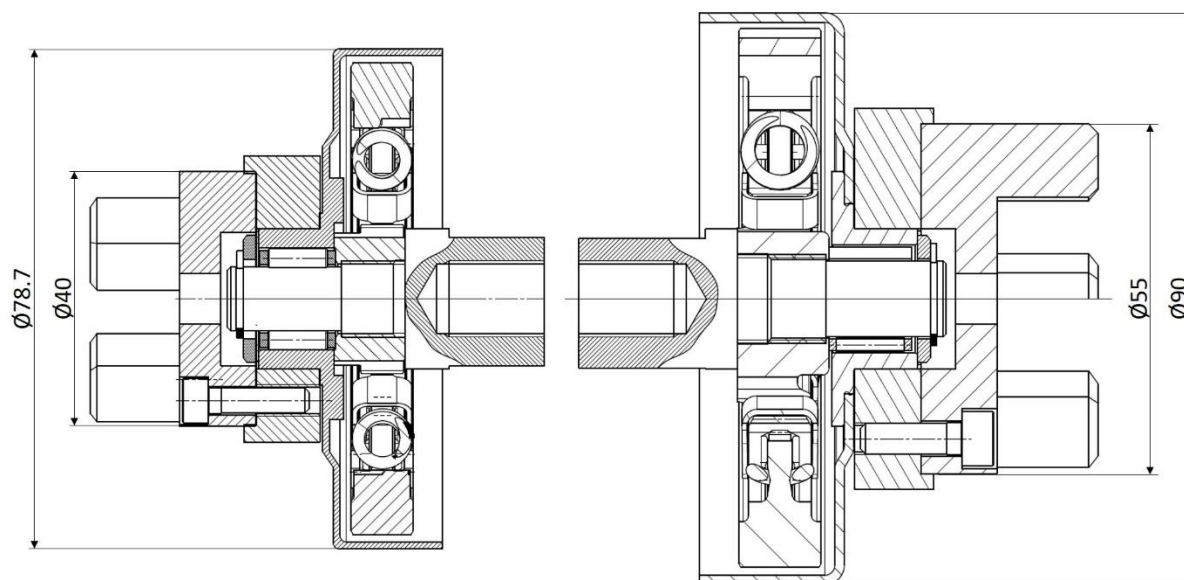


Figure 4-13: Comparison of the two clutch assemblies

The elastomer jaw couplings have different torque limits, depending on the shore hardness of the used elastic spider. In Table 4-3, the nominal torque and the peak torque of those couplings are listed.

	Shore hardness of elastic spider	Nominal torque	Maximum torque
Small elastomer jaw coupling (left side in Figure 4-13)	92 SH A	10	20
	98 SH A	17	34
	64 SH D	21	42
Big elastomer jaw coupling (right side in Figure 4-13)	92 SH A	35	70
	98 SH A	60	120
	64 SH D	75	150

Table 4-3: Torque rating of the elastomer jaw couplings [18]

The nominal torque of the combustion engine amounts to 3.8 Nm (cf. Figure 5-2). The instant torque peaks are up to 11 times higher than the nominal torque (cf. Figure 2-1), resulting in torque spikes around 42 Nm. The maximum torque that the small elastomer jaw coupling can transfer is 42 Nm (Table 4-3). Those 42 Nm get reduced if the alignment of the two shafts is poor, as well as it decreases when the temperature rises above ambient temperature (cf. Appendix - RINGFEDER Elastomer Jaw Couplings [18]). This means that there is no safety margin left with the small elastomer jaw coupling. Due to those factors, the small coupling lasted only for a very short time during the experiments and a change to the bigger coupling was inevitable.

In Table 4-4 the BOM for the large clutch assembly can be seen.

Num	Name	Quantity	Manufacturing	Material	Weight [g]	Comments / Pictures
1	clutch bell housing	1				
2	clutch	1				
3	needle cage 12x17x13	1				
4	washer 12	1		steel		DIN EN ISO 7090
5	circlip 12	1		steel		DIN 471
6	adaptor	1	lathe, mill	steel	92	
7	adaptor to clutch bell housing	1	wire eroding / lathe, thread	steel	197	
8	elastomer jaw coupling GWE 5103-24 <i>with elastomer spider - 98 SH A (red)</i>	1	lathe, drill	aluminium & poly- urethane	207	
9	elastomer jaw coupling GWE 5102-24 <i>with elastomer spider - 64 SH D-H (green)</i>	1		aluminium & hytel	81	
10	elastomer spider - 92 SH A (yellow) <i>for elastomer jaw coupling GWE size 24</i>	2		poly- urethane		
11	elastomer spider - 98 SH A (red) <i>for elastomer jaw coupling GWE size 24</i>	2		poly- urethane		
12	elastomer spider - 64 SH D-H (green) <i>for elastomer jaw coupling GWE size 24</i>	2		hytel		
13	cylinder head screw M5 x 16	8		steel		DIN EN ISO 4762

Table 4-4: BOM – large clutch assembly

Figure 4-14 illustrates the design for the ICE measurements with the big elastic jaw coupling. The next step for starting the measurements was to find a place for a speed and position sensor.

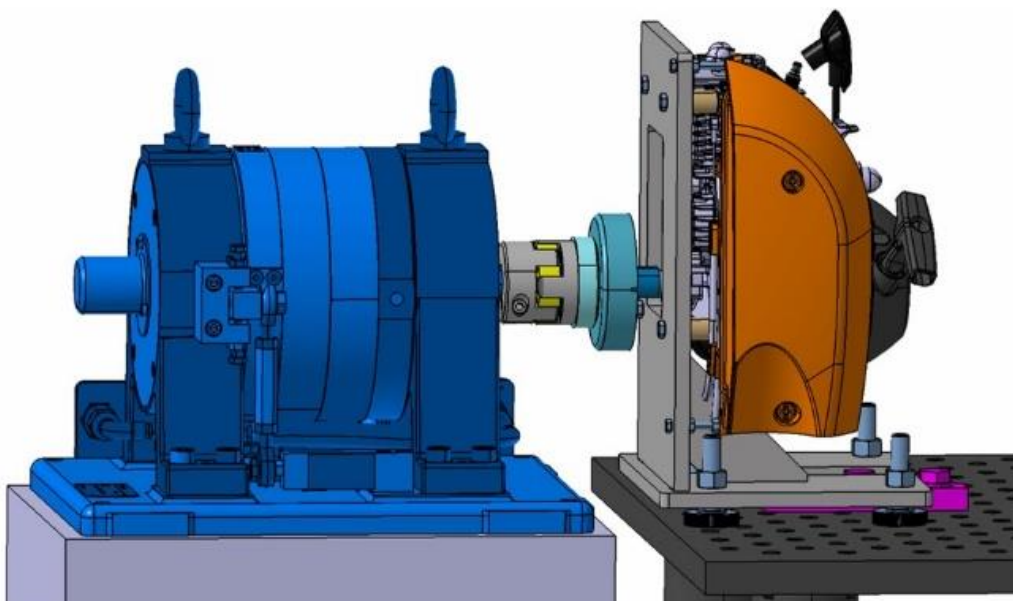


Figure 4-14: Baseline ICE setup with big elastomer jaw coupling

4.1.6 Magnetic speed sensor

A sensor for measuring the speed of the crankshaft and especially for finding the position of the TDC was needed. This sensor is crucial for the cylinder-pressure indication and for the ignition timing on the hybrid (cf. 4.2 Measuring setup). The selected sensor is a magnetic sensor. It is a passive device requiring no external power supply. The alternating output voltage is a result of the self-induced magnetic field caused by nearby moving ferrous metal parts [23]. As ferromagnetic part, a gearwheel made of steel is used. The gearwheel has 35 teeth with one missing tooth (35-1). The missing tooth is necessary to determine the TDC.

In Figure 4-15, the magnetic speed sensor (1) together with its mounting panel (2) is shown. The mounting panel (2) is bolted to the ICE mounting plate (4) with two bolts (5) and nuts (6). The gearwheel (3) is mounted on the crankshaft (7) with a retaining compound (Loctite 601) and secured with a headless screw.

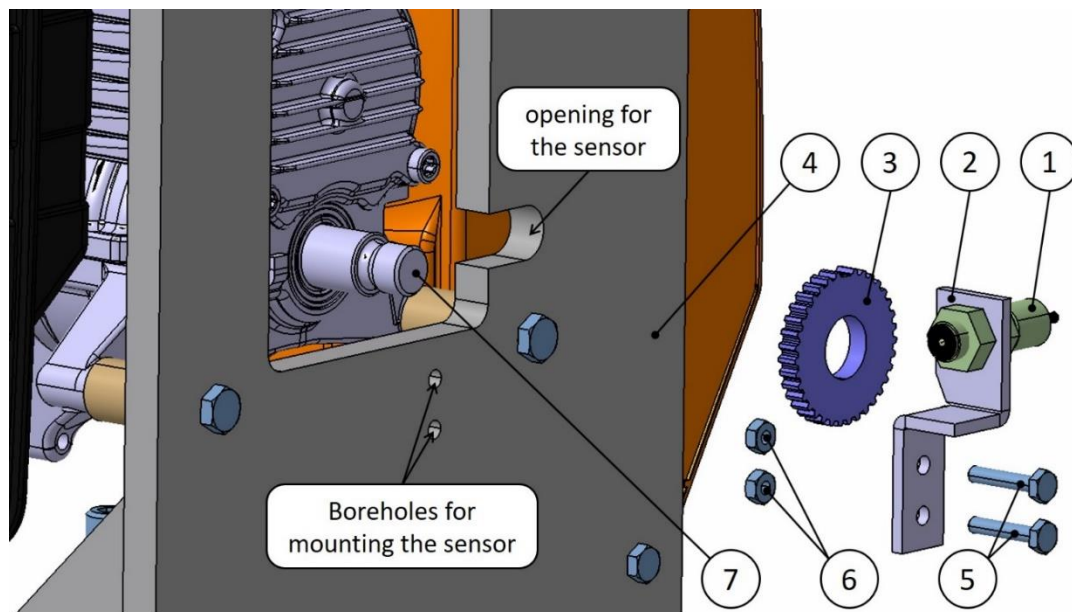


Figure 4-15: Magnetic speed sensor assembly

Figure 4-16 displays the mounted magnetic sensor together with the gearwheel installed on the crankshaft. With this sensor installed and adjusted, the first starts of the ICE were carried out.

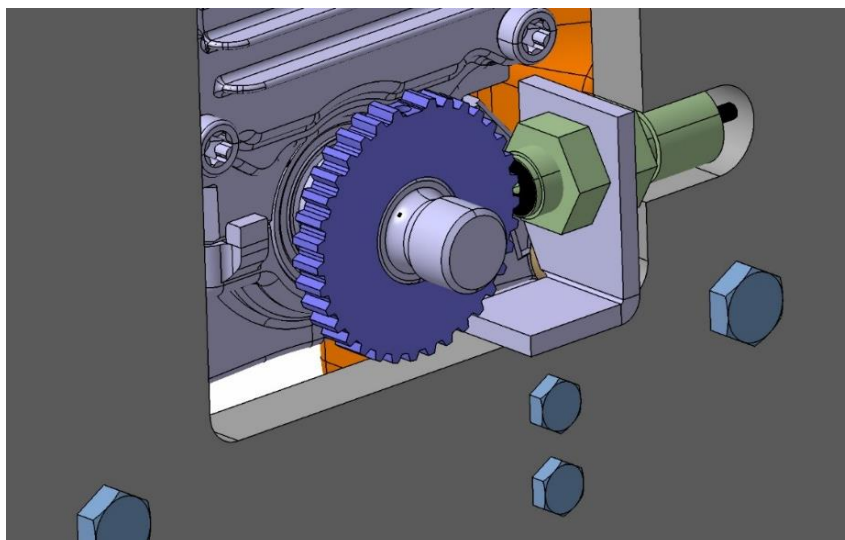


Figure 4-16: Magnetic speed sensor mounting

4.1.7 Cooling

After the first runs of the baseline ICE setup, high engine temperatures were detected and cooling had to be designed. For a better understanding of the problem, the full blower tool and its fan casing were investigated in terms of air cooling. When examining the fan housing, it was discovered that parts of the blower airflow are diverted to cool the engine (left side in Figure 4-17). Those airflows are redirected by the fan casing to escape to the exhaust side after cooling the engine (right side in Figure 4-17).

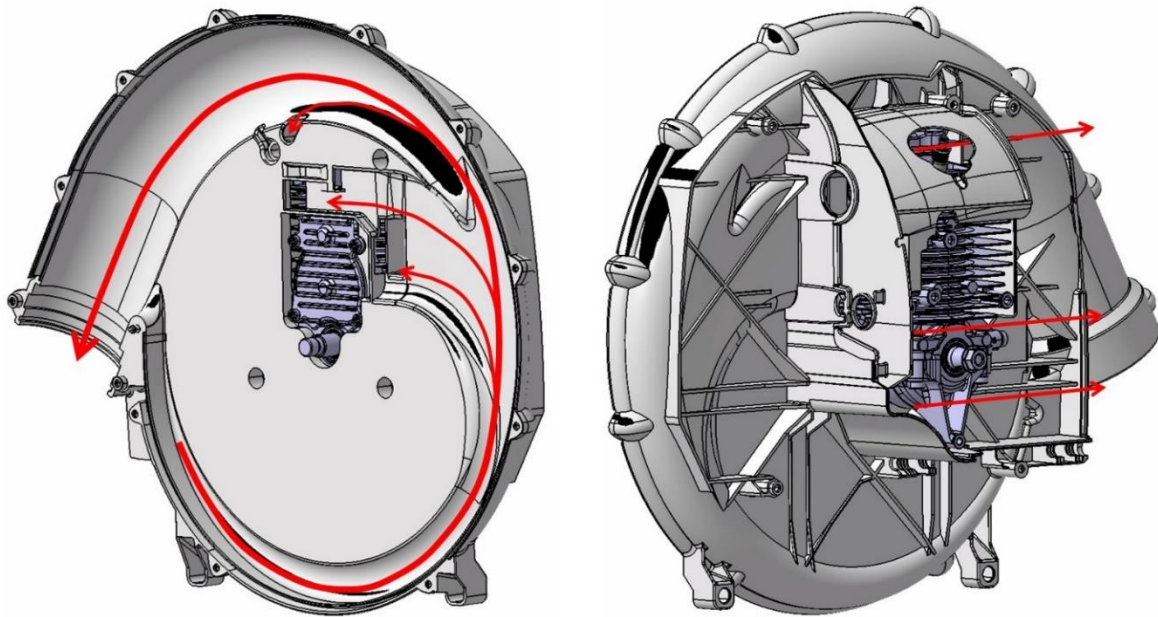


Figure 4-17: Fan casing of the full blower tool

Taking into account the knowledge gained about the cooling of the full blower, a cooling system for the combustion engine was designed. The cooling airflow is provided by an external fan together with plastic pipes to direct the flow to the engine (cf. Figure 4-20). The positioning of those plastic pipes is depicted in Figure 4-18 (red arrows on the right).

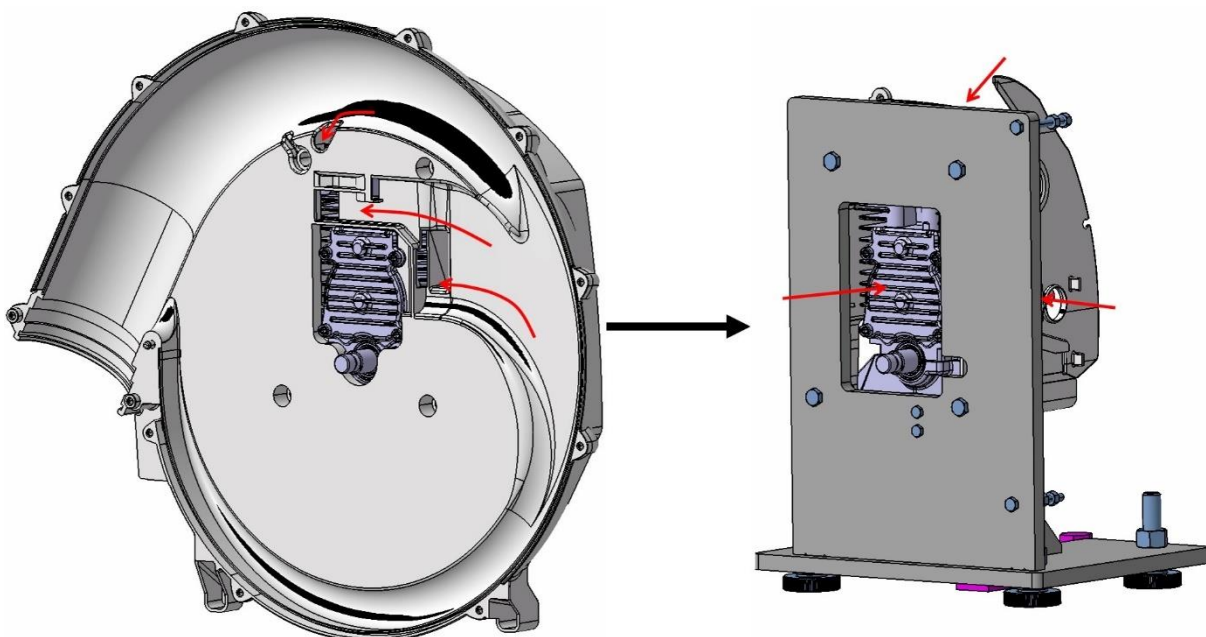


Figure 4-18: Cooling flow

In order to direct the airflow around the ICE, the fan casing was cut to get a small cooling shroud (Figure 4-19). Since the fan casing and the mounting plate are using the same bolt pattern, no additional bolts for the cooling shroud are required (cf. Figure 4-18).

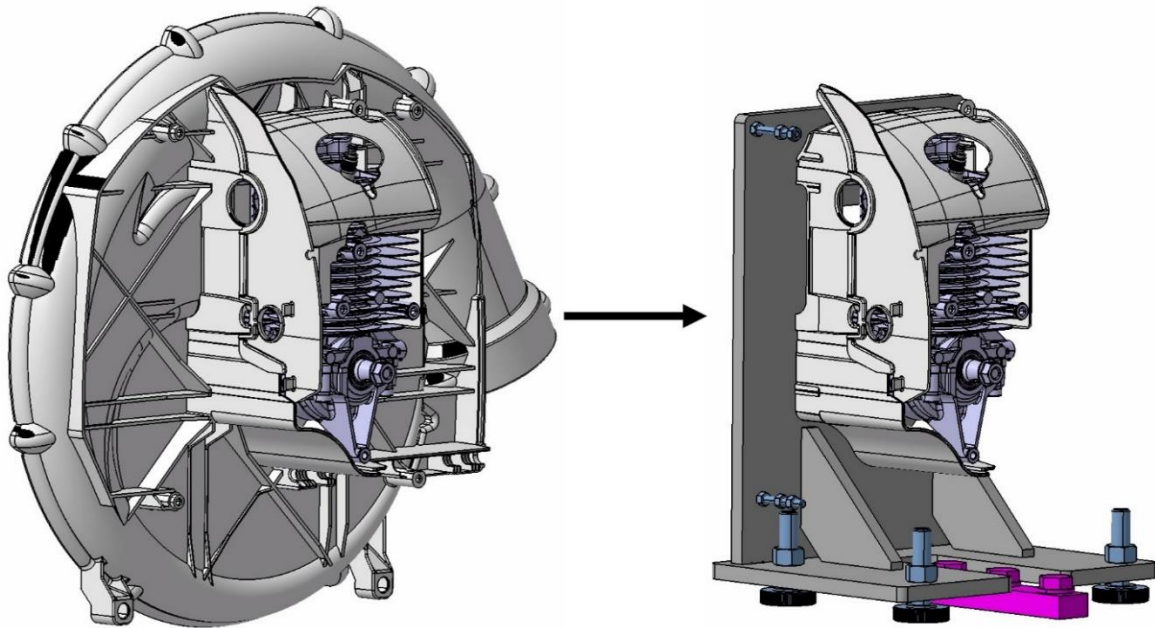


Figure 4-19: Cooling shroud

Figure 4-20 shows the three cooling pipes. The main airflow (1) is going to the front of the engine and to the clutch assembly for cooling the elastomer jaw coupling (cf. Appendix - RINGFEDER Elastomer Jaw Couplings [18] – temperature factor). One airstream is pointing at the top of the engine (2) and the last cooling pipe is blowing air from the intake side (3). Due to the cooling shroud, the hot air is escaping only to the exhaust side.

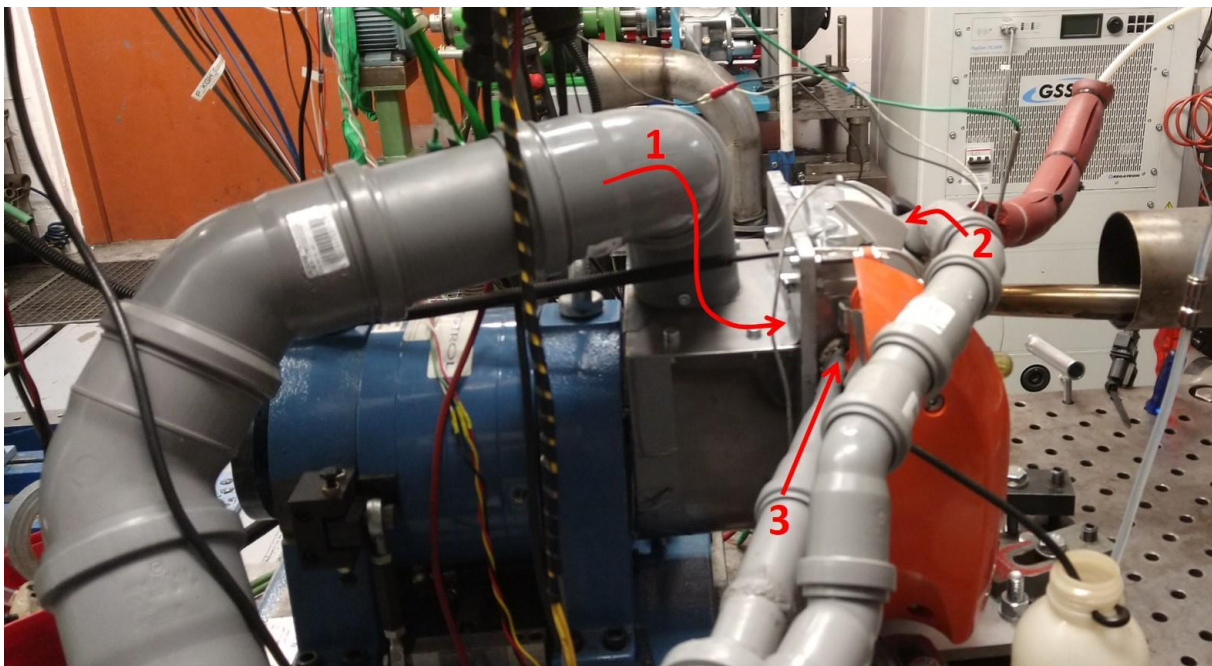


Figure 4-20: Cooling pipes

Since the power for the cooling is coming from an external source and not from the engine, it must be taken into account both in the simulation model and when building a prototype (cf. chapter 7 Outlook).

4.1.8 Electric Motor coupling – first design

The first design for coupling the EM to the ICE is kept small in size and weight to obtain the possibility of building a prototype. For this hybrid design, the pull starter is removed, as it is no longer needed. The flywheel and the ignition coil are removed as well and replaced by the battery coil ignition system (cf. Figure 4-3). The gained space on this side of the ICE is used to couple the EM. The rotor of the EM shall be directly fastened on the crankshaft. Therefore, the EM is disassembled to have the rotor and the stator separately. In order to mount the EM rotor (1) on the crankshaft (5) an adaptor part (2) is needed (Figure 4-21). The adaptor part (2) is provided by STIHL and fits to the cone and the feather key groove of the crankshaft (5). The adaptor (2) and the rotor (1) are connected with a press fit and secured with three bolts (3). This assembly consisting of rotor (1), adaptor (2) and bolts (3) is put on the crankshaft (5) and tightened with the nut of the flywheel (4) (cf. Figure 4-23).

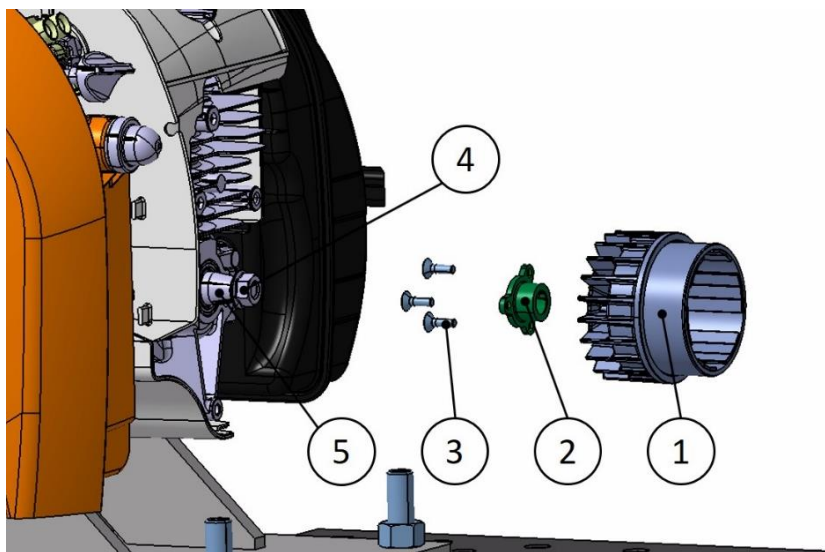


Figure 4-21: Coupling of the EM rotor to the crankshaft

In order to mount the stator (1) on the ICE, a mounting plate (2) is required (Figure 4-22). The stator (1) is centred on the mounting plate (2) and tightened with three bolts (3), washers (4, 5) and nuts (6). The stator (1) and the mounting plate (2) are then bolted in the place where the pull starter used to be, with three threaded rods (7). To keep the required distance between the ICE and the stator (1), three distance bushings (8) of the same length are used. The assembly is afterwards fastened with three washers (9) and nuts (10).

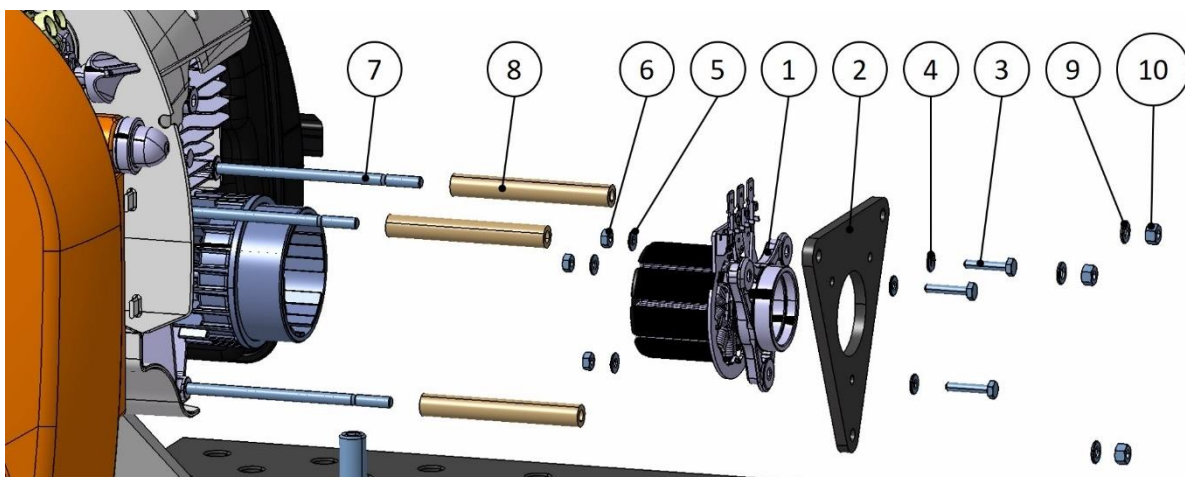


Figure 4-22: Coupling of the EM stator to the ICE

The air gap between the rotor and the stator is 0.3 mm in the assembled state of the EM. Due to this small air gap, a possibility for aligning the rotor and the stator had to be discovered. Since the crankshaft (1) has a center hole on this engine side, a possible way for the alignment was found (Figure 4-23). The shaft of the EM (2), which is no longer needed, is used for the alignment. A cone fitting to the center hole of the crankshaft (1) was machined to the EM shaft (2). Furthermore, a threaded sleeve (3) was machined and pressed into the stator (4). The same threading was machined to the EM shaft (2) and the shaft got bolted to the threaded sleeve (3). Thus, the EM shaft (2) is centred in the stator (4) via the threaded sleeve (3) and the needle sleeve (5). By loosening the nuts (6) and screwing the shaft (2) until it touches the center hole of the crankshaft (1) the EM stator is aligned. The nuts (6) are tightened and the EM shaft (2) is screwed away from the crankshaft (1). To prevent the EM shaft (2) from contacting the crankshaft (1) while the ICE is running, the shaft (2) is secured with a locking nut (7).

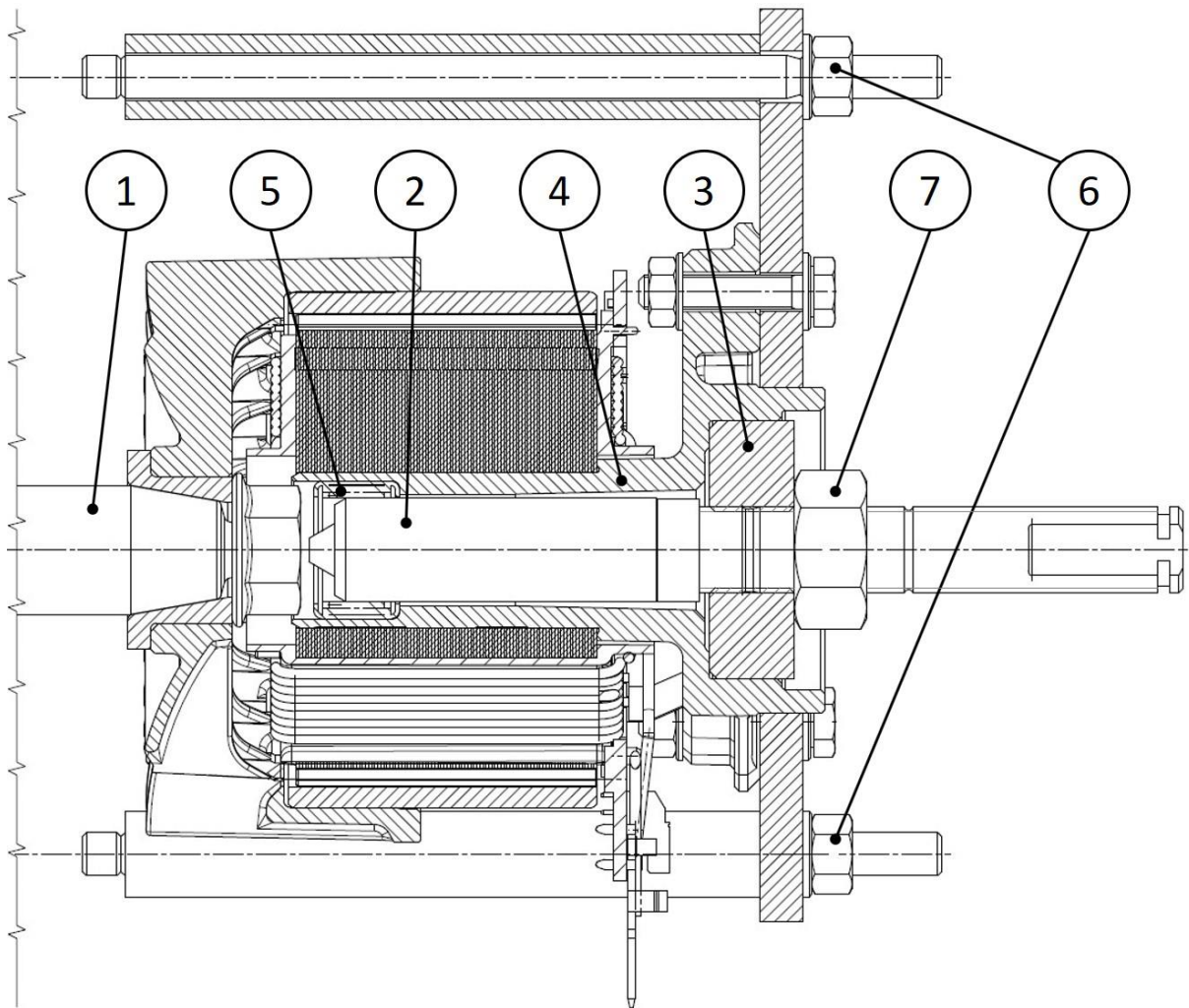


Figure 4-23: EM alignment

The bill of materials for the first EM design (Table 4-5) shows all the required parts and manufacturing steps. The EM and the rotor connector are provided by STIHL. After disassembling the EM, the shaft is machined in-house and the rotor is machined to fit to the rotor connector. The mounting plate, distance bushings and threaded sleeve are machined in-house as well. Together with the bolts, nuts and washers this is forming the fourth subassembly.

Num	Name	Quantity	Manufacturing	Material	Weight [g]	Comments / Pictures
1	EM r06i2	1				
2	EM r06i2 rotor	1	lathe, drill	steel		
3	rotor connector	1	drill	steel		
4	countersunk head screw M4 x 16	3		steel		DIN EN ISO 10642
5	mounting plate EM	1	cut, drill	steel	195	
6	distance bushing	3	lathe	steel	32	
7	threaded rod M5 x 100	3		steel		DIN 976
8	washer 5	3		steel		DIN EN ISO 7089
9	nut M5	3		steel		DIN EN ISO 4032
10	hexagon head screw M4 x 20	3		steel		DIN EN ISO 4017
11	washer 4	6		steel		DIN EN ISO 7089
12	nut M4	3		steel		DIN EN ISO 4032
13	threaded sleeve	1		steel	51	
14	EM r06i2 shaft	1	lathe	steel	71	
15	nut M10	1		steel		DIN EN ISO 4032

Table 4-5: BOM – EM, first design

4.1.9 Electric Motor coupling – second design

The second design was prepared for the purpose of test bench investigation, where the weight and size are not relevant. On this design, the EM stays assembled and the shaft of the EM rotor (1) is connected to the crankshaft (2) (cf. Figure 4-24). To allow some misalignment between the crankshaft (2) and the shaft of the EM rotor (1), and to avoid distortion of the bearings, an elastic jaw coupling (3, 4, 5) is used. The jaw clutch (3) is joined with an adaptor part (6) and three bolts (7). This assembly fits to the crankshaft (2) and is secured with a nut (8) (similar to Figure 4-21). The other jaw clutch (5) is pressed to the shaft of the EM rotor (1). The EM stator (9) is bolted to the mounting plate (10) with three bolts (11), washers (12) and nuts (13). For the final connection of the two shafts, three threaded rods (14) and three distance bushings (15)

are used to keep the mounting plate (10) in the correct distance. The whole assembly is then tightened with three washers (16) and nuts (17) (similar to Figure 4-22).

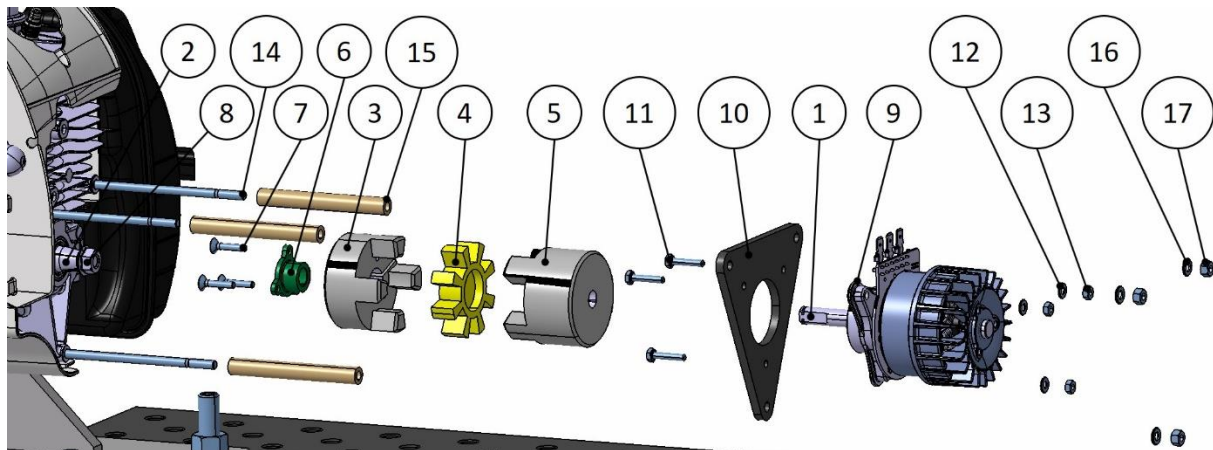


Figure 4-24: Coupling of the EM to the ICE

Table 4-6 is showing the BOM for the second EM design. The elastomer jaw coupling was ordered and the further manufacturing steps were done in-house in order to be joined with the rotor connector from STIHL. Together with the mounting plate, distance bushings and the remaining small parts this is forming the fifth subassembly.

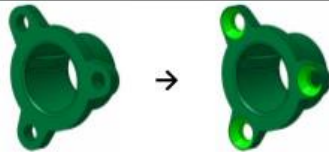
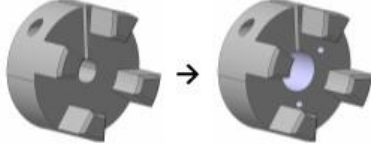


Num	Name	Quantity	Manufacturing	Material	Weight [g]	Comments / Pictures
1	EM r06i2	1				
2	rotor connector	1	drill	steel		
8	elastomer jaw coupling GWE 5103-24 <i>with elastomer spider - 98SHA (red)</i>	1	lathe, drill	aluminium & poly-urethane	127	
9	elastomer jaw coupling GWE 5102-24 <i>with elastomer spider - 64SHD-H (green)</i>	1		aluminium & hytel	205	
4	countersunk head screw M4 x 16	3		steel		DIN EN ISO 10642
5	mounting plate EM	1	cut, drill	steel	195	
6	distance bushing	3	lathe	steel	32	
7	threaded rod M5 x 100	3		steel		DIN 976
8	washer 5	3		steel		DIN EN ISO 7089
9	nut M5	3		steel		DIN EN ISO 4032
10	hexagon head screw M4 x 20	3		steel		DIN EN ISO 4017
11	washer 4	6		steel		DIN EN ISO 7089
12	nut M4	3		steel		DIN EN ISO 4032

Table 4-6: BOM – EM, second design

4.2 Measuring setup

In this subchapter, the setup for the measurements and the used measurement equipment for capturing the data is explained.

4.2.1 Reference ICE

The reference ICE (cf. 3.1) together with the designed and manufactured parts are mounted on the test bench. In Figure 4-25, the measurement setup for the reference measurements of the ICE is displayed.

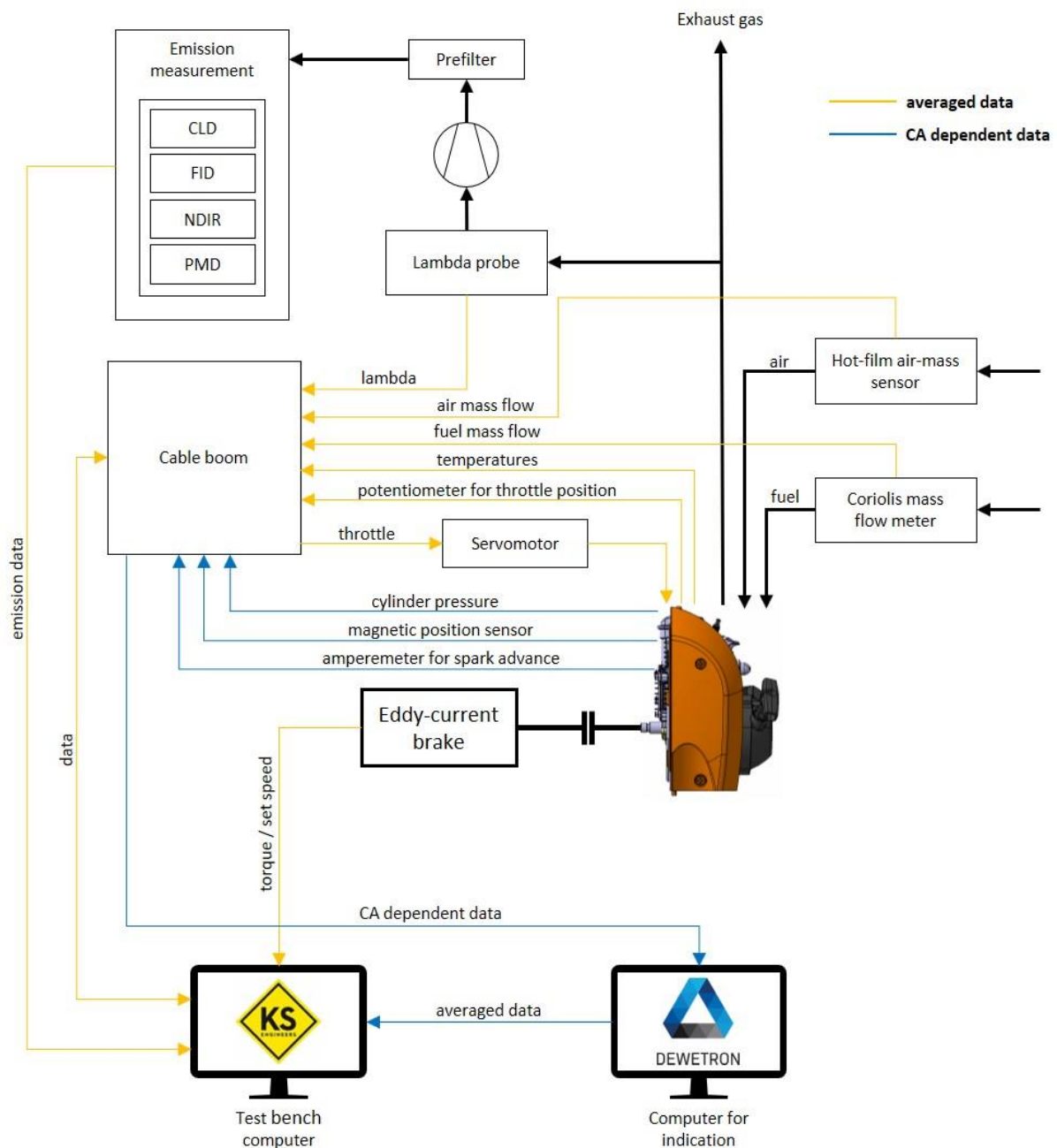


Figure 4-25: Measurement setup for reference ICE

All the necessary sensors and actuators for carrying out the measurements have been installed and/or connected to the test bench (see table below).

sensors and measuring devices	Lambda probe
	Hot-film air-mass sensor
	Coriolis mass flow meter (fuel)
	Thermocouples for spark plug, intake air and exhaust gas temperature
	Potentiometer for the throttle position
	Magnetic sensor for TDC and CA
	Piezoresistive sensor for cylinder pressure
	Amperemeter for spark advance
actuator	Servomotor for adjusting the throttle
emission measuring system	CLD for NO _x measurements
	FID for HC measurements
	NDIR for CO and CO ₂ measurements
	PMD for measuring oxygen content

Table 4-7: Sensors and actuators for carrying out measurements

As it can be seen from Figure 4-25, the measured data is divided into two groups:

- averaged data
- CA dependent data

4.2.1.1 CA dependent data

The CA dependent data are captured with a DEWE-800 from DEWETRON. For measuring the CA, a magnetic sensor together with a gear wheel (Figure 4-27) is used. The gearwheel has one missing tooth which is necessary to determine the TDC. The TDC alignment is required for the pressure indication system. In order to detect the offset between the TDC and the missing tooth, a capacitive probe is used. The probe is screwed to the ICE instead of the spark plug. Then the engine is brought to a constant speed with the usage of an additional electric drive and the signal of the capacitive probe is recorded on the DEWE-800. Hence, the geometrical TDC of the engine is determined.

The pressure indication of the combustion chamber is done with a piezoresistive pressure sensor (Figure 4-26). To capture and analyse this signal, the software DEWEsoft 7 is utilised. From the pressure signal the MFB, combustion abnormalities, peak pressure and other combustion properties may be investigated. By averaging the data over several cycles, the IMEP, IMEP_COV and 50% MFB are calculated.

A current clamp for measuring the ignition signal over the crank angle is employed. Via this ignition signal, the spark advance is determined.

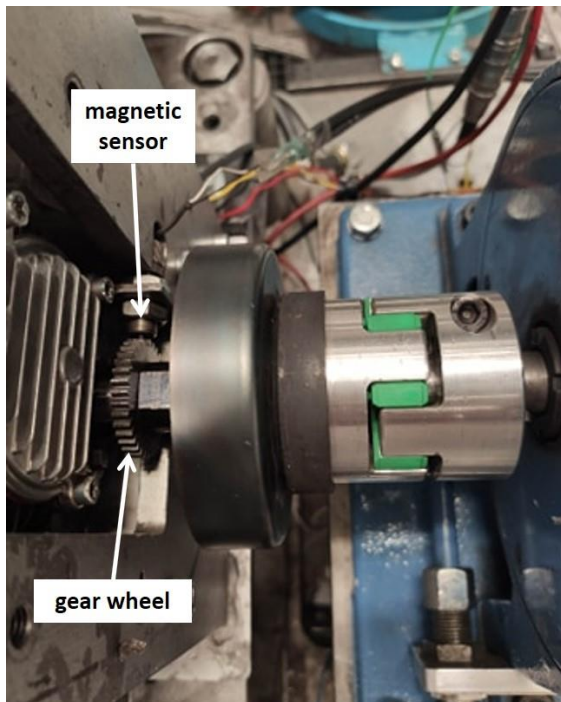


Figure 4-27: Magnetic sensor and gear wheel

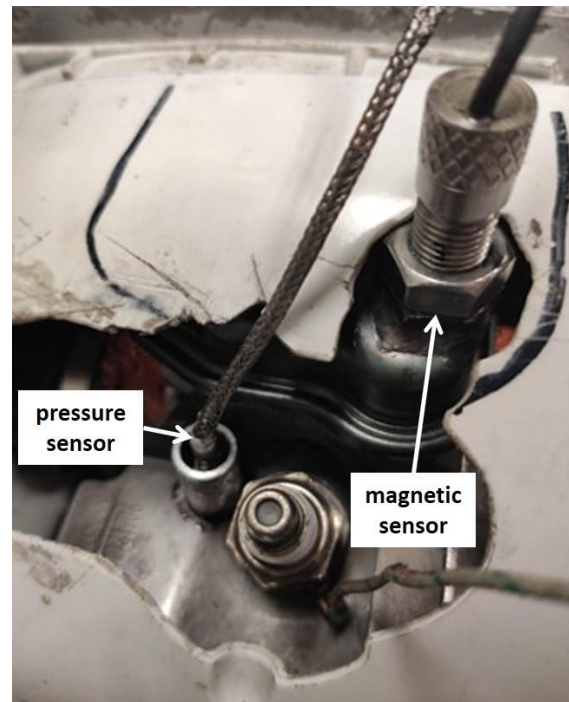


Figure 4-26: Pressure sensor and magnetic sensor for synchronisation

4.2.1.2 Averaged data

The software Tornado from KS Engineers is capturing the data with a sampling rate of 10 – 100 Hz over the period of one measuring point. The measured data is averaged and saved. The averaged data from DEWE-800 is sent to Tornado and saved as well.

Tornado is controlling the speed of the engine via the eddy-current brake. At the eddy-current brake from the company Magtrol, the torque is measured with the aid of a force gauge. The other averaged data are measured with the sensors from Table 4-7. For monitoring the measured data of the lambda probe, the air-fuel ratio is calculated from the air and fuel mass flow. The emissions are measured with the exhaust gas analysers according to Table 4-7.

4.2.2 ICE with modified carburettor and ignition system

On the modified ICE, the measurement setup is the same as on the reference ICE with the enhancement of the ECU MoTeC M150. The ECU is able to control the ignition timing and also the excess air ratio when using the M-tronic carburettor.

Instead of the original magneto ignition, a battery coil ignition is implemented. This change is done in preparation for the hybrid system (cf. Figure 4-3). The ignition coil is mounted on the test bench and controlled by MoTeC. In order to control the spark advance, the ECU needs the speed, respectively the CA signal from the magnetic sensor (cf. 4.1.6).

To gain the possibility of a fuel cut-off and to control the excess air ratio, the original carburettor is changed to the M-tronic carburettor (cf. 2.1.10). For controlling the air fuel ratio, the ECU needs the throttle position, the CA signal and a synchronisation signal. The throttle position is determined by a potentiometer mounted on the carburettor. The CA signal and the synchronisation signal are each detected with a magnetic sensor. For the CA signal the same sensor as for DEWETRON is used (Figure 4-27). The synchronisation signal is taken from a

magnetic sensor pointing at a rocker arm of the valve train (Figure 4-26). This synchronisation signal is required to distinguish between the gas cycle TDC and the combustion TDC. The air fuel ratio is then controlled via a PWM signal from the ECU.

Figure 4-28 displays the measurement setup for the modified ICE. In comparison to the setup of the reference ICE, the MoTeC ECU and an application computer are added.

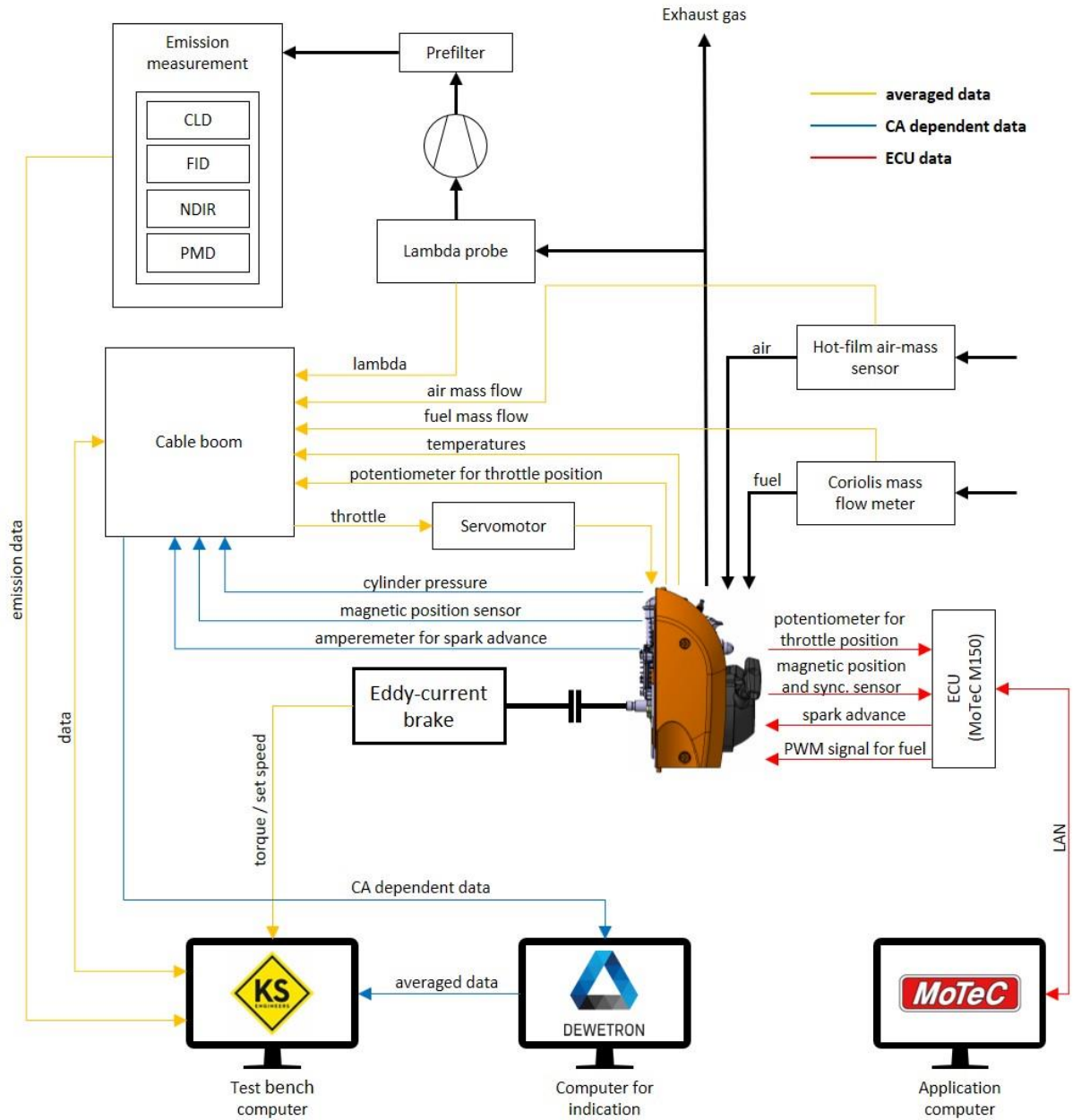


Figure 4-28: Measurement setup for modified ICE

4.2.3 Parallel Hybrid System

For the measurements on the parallel hybrid system, another ECU and a battery simulator as power source are required (Figure 4-29). The ECU from RoboteQ can control the speed or the torque of the EM via three hall sensors for feedback. Since the eddy-current brake is controlling the speed of the system, a speed control of the EM is not possible.

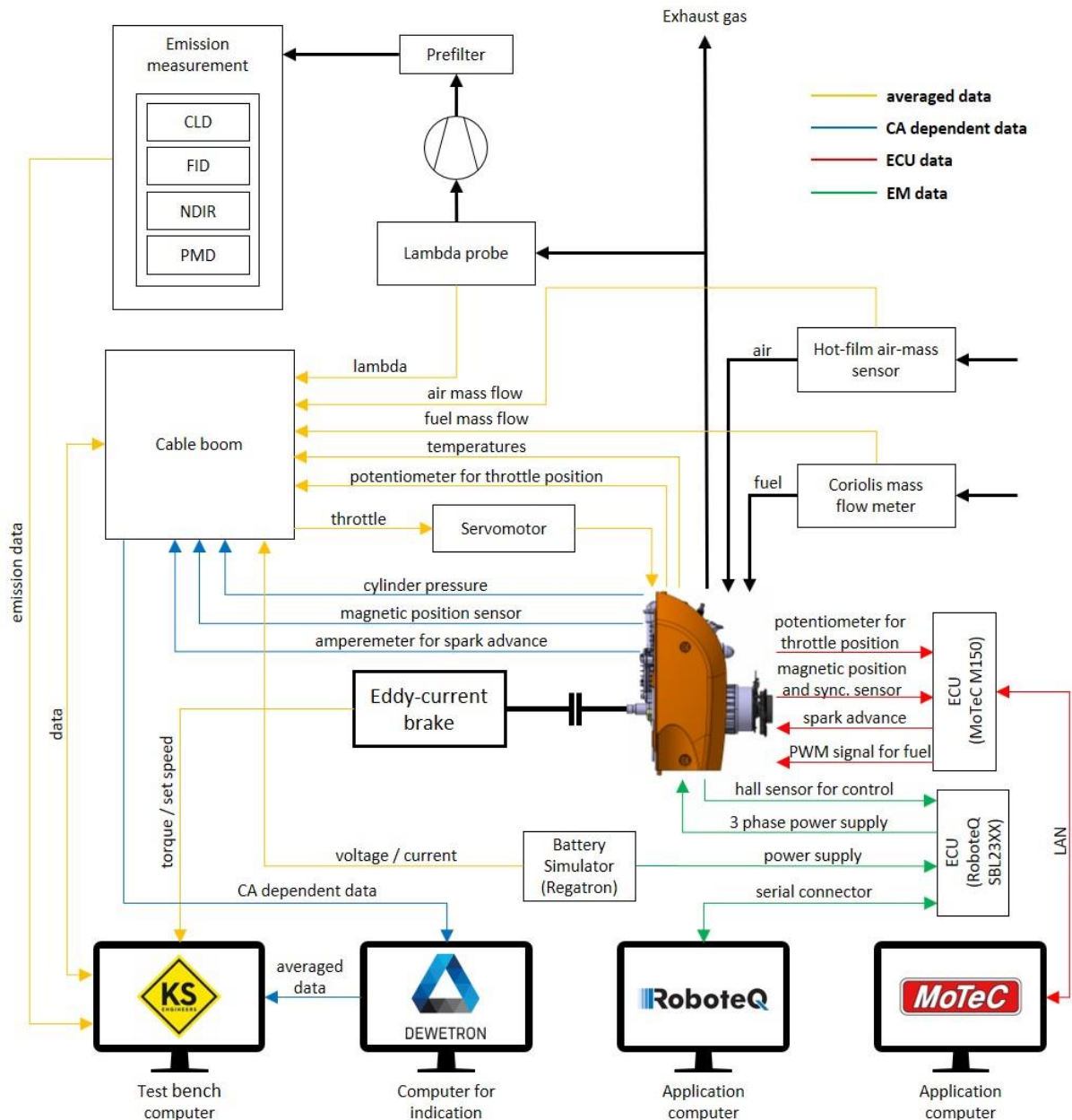


Figure 4-29: Measurement setup for hybrid system

The battery simulator from Regatron is connected to Tornado with a serial connector. This connection provides data for the voltage and the current drawn by the EM. From those numbers, together with the torque and speed measurement, the electric motor efficiency is calculated.

5 Experimental Investigations

In the following chapter, the executed experimental investigations and the within acquired results are presented. The experimental investigation starts with comparing the WOT curve of the utilised ICE, to the WOT curve provided from STIHL for the same engine. After the comparison with the STIHL data, the ICE is characterised. For the characterisation of the ICE, engine maps are generated to compare the different variants with each other. Following the ICE characterisation, two hybrid designs are tested and measurements are carried out on the second design.

All the measurements were executed with the premixed STIHL MotoMix fuel which has a mixing ratio of 1:50 oil to gasoline (for further information see [31]).

5.1 WOT comparison with STIHL data

For validating the ICE and the test-bench setup, a comparison with the data from STIHL was done. STIHL provided a WOT curve of the engine. For the comparison, a WOT curve with the original magneto ignition and a WOT curve with the battery coil ignition were measured.

5.1.1 Test setup

For the first WOT curve, only small changes on the engine have been made in order to meet the reference data of STIHL. A pressure sensor was mounted in the combustion chamber (cf. Figure 4-26) and the air intake box was modified in order to connect the engine to the air mass flow measurement system of the test bench (Figure 5-1). Those two changes will remain also for all the other measurements carried out.

Beside those two modifications, the ICE is unchanged as it was delivered from STIHL. This configuration is referred to as magneto ignition in the results.



Figure 5-1: Modified air intake box

To evaluate if the change from the magneto ignition to the battery coil ignition has an impact on the engine, a WOT curve was measured. The ignition timing was set according to the original ignition timing for this engine. Thus, exactly as with the original magneto ignition. Apart from this, the ICE features the same changes as mentioned before (pressure sensor and air intake box.).

5.1.2 Results

By comparing the three WOT curves in Figure 5-2, only small differences in the high rpm torque are found. Those differences are in an acceptable range and are explainable with the implemented ignition change on the engine and, therefore, small deviations in the spark advance (cf. 5.2.2 Results ignition change). The constant offset in the fuel consumption and in the BSFC can be explained with the used fuel and a richer air-fuel ratio in the measurements of STIHL. The fuel used in the STIHL measurements is a mixture of gasoline (95 octane) and two-stroke oil, while for the herein executed measurements the premixed STIHL MotoMix was used. The NCV of gasoline (95 octane) amounts to 42 MJ/kg, while the NCV of STIHL MotoMix adds up to 44.5 MJ/kg ([2],[31]).

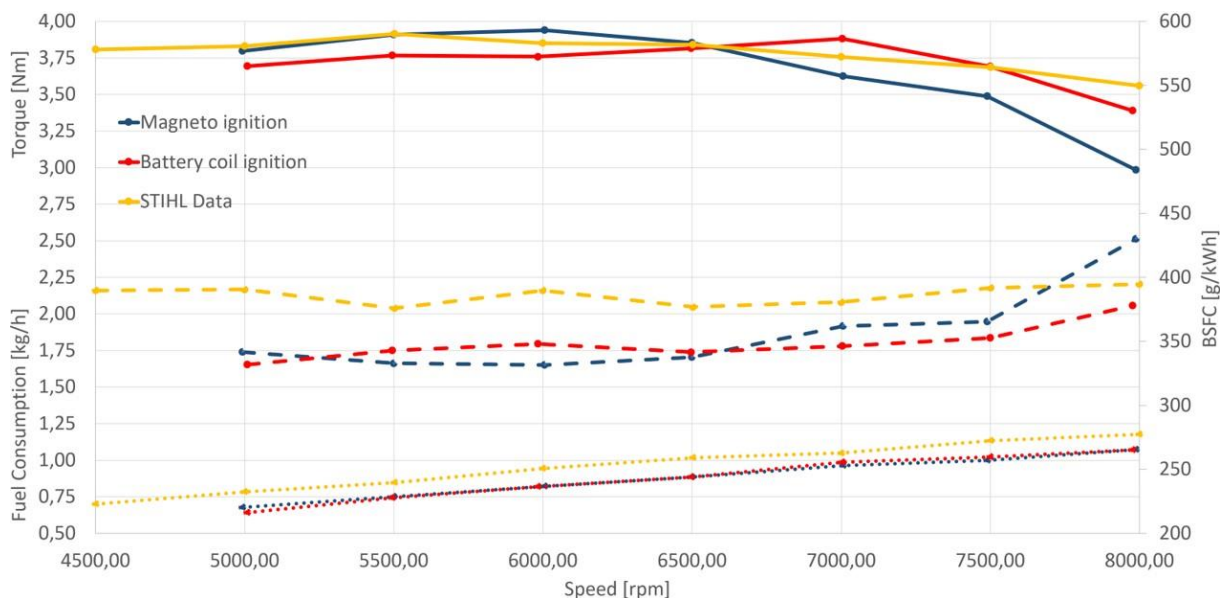


Figure 5-2: WOT comparison

The results obtained suggest that the changes done to the ICE (pressure sensor and air intake box) have only a minor impact. Furthermore, the swap from the magneto ignition to the battery coil ignition seems to affect the engine's behaviour only slightly at high speeds, but further investigations are carried out (see subchapter 5.2).

5.2 ICE characterisation

In this subchapter, the ICE is characterised for three different purposes. The first purpose of the ICE characterisation is to check if the change of the magneto ignition to the battery coil ignition changed the behaviour of the engine. The second purpose is to test if the swap from the original carburettor to the M-tronic carburettor does alter the engine behaviour. Finally, the third reason for the ICE characterisation is to create engine maps in order to refine the simulation model.

5.2.1 Test setup ignition change

The first maps were created with the original carburettor and the original magneto ignition as a reference. Then the ignition system got changed to the battery coil ignition. The spark advance of the battery coil ignition is set according to the ignition timing values supplied by STIHL for this engine. Thus, it is set exactly as with the original magneto ignition. This is done in order not to change the behaviour of the ICE.

5.2.2 Results ignition change

As mentioned above, the engine performance shall stay the same and, therefore, the ignition timing of the battery coil ignition is set to the manufacturer values. By measuring the spark advance with an amperemeter, similar values were identified at WOT on both ignition systems. Only on the point at 8000 rpm a difference of about 3 degrees CA was found between the two ignition systems. Since the spark advance has a major impact on the heat release characteristics, two heat release curves at WOT and 8000 rpm are compared (figure below). This point is also showing the highest difference in the torque of the WOT comparison (Figure 5-2).

Figure 5-3 depicts the WOT heat release curve of the ICE with the magneto ignition and with the battery coil ignition. A difference in the amperemeter 50% MFB of about 3 degrees CA can be seen. Furthermore, the peak firing pressure with the magneto ignition is about 4 bar lower and a few degrees CA earlier than with the battery coil ignition. These differences are also visible in the IMEP which is 0.6 bar lower in the measurements with the magneto ignition.

Those results are delineating the major influence that the spark advance has on the heat release characteristics, hence, on the pressure curve, and furthermore, on the IMEP and BMEP. Since the differences are generally small, it can be stated that the change of the ignition system has only a minor influence on the characteristics of the ICE. Furthermore, the battery coil ignition which will be used for the measurements on hybrid system shows very similar values at WOT compared to the data from STIHL.

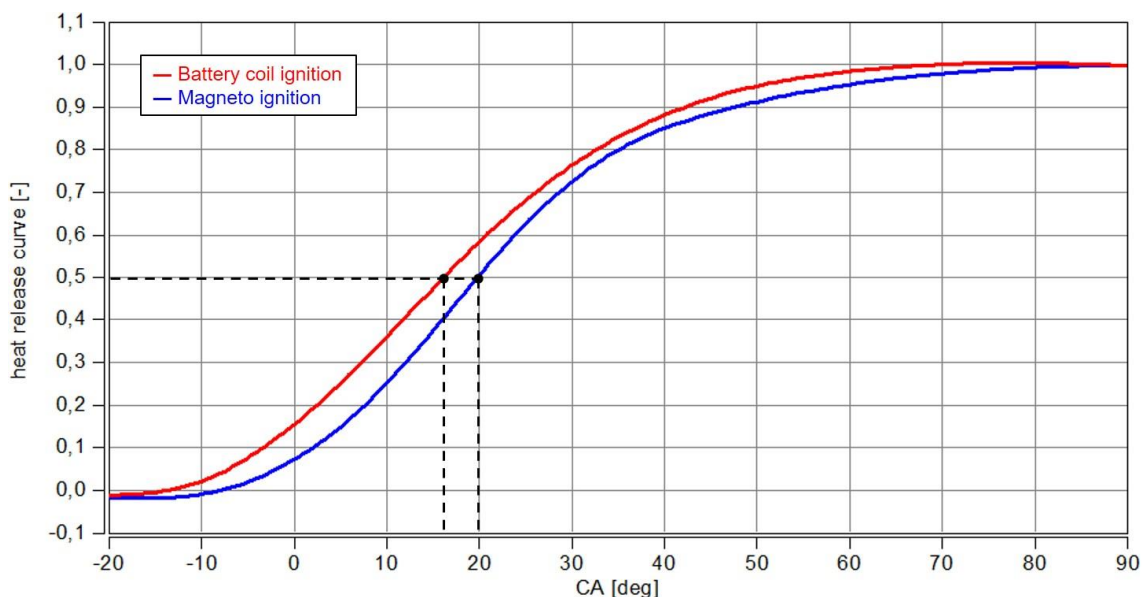


Figure 5-3: Heat release curves at 8000 rpm WOT

In addition, the spark advance is also an important factor for the fuel consumption. To compare the fuel consumption, two BSFC maps are created (Figure 5-4 and Figure 5-5).

Both fuel consumption maps are showing a very similar behaviour of the iso lines. The region of the lowest BSFC is at WOT, as it was expected. The fuel consumption is quite low for a combustion engine for hand-held power tools. This can be explained by the use of the external cooling and, compared to the STIHL measurement, with the different fuel (cf. 5.1.2). The small areas of a higher BSFC at 2.25 Nm and 5500, respectively 6000 rpm are due to the factory setting of the original carburettor (cf. Figure 5-6).

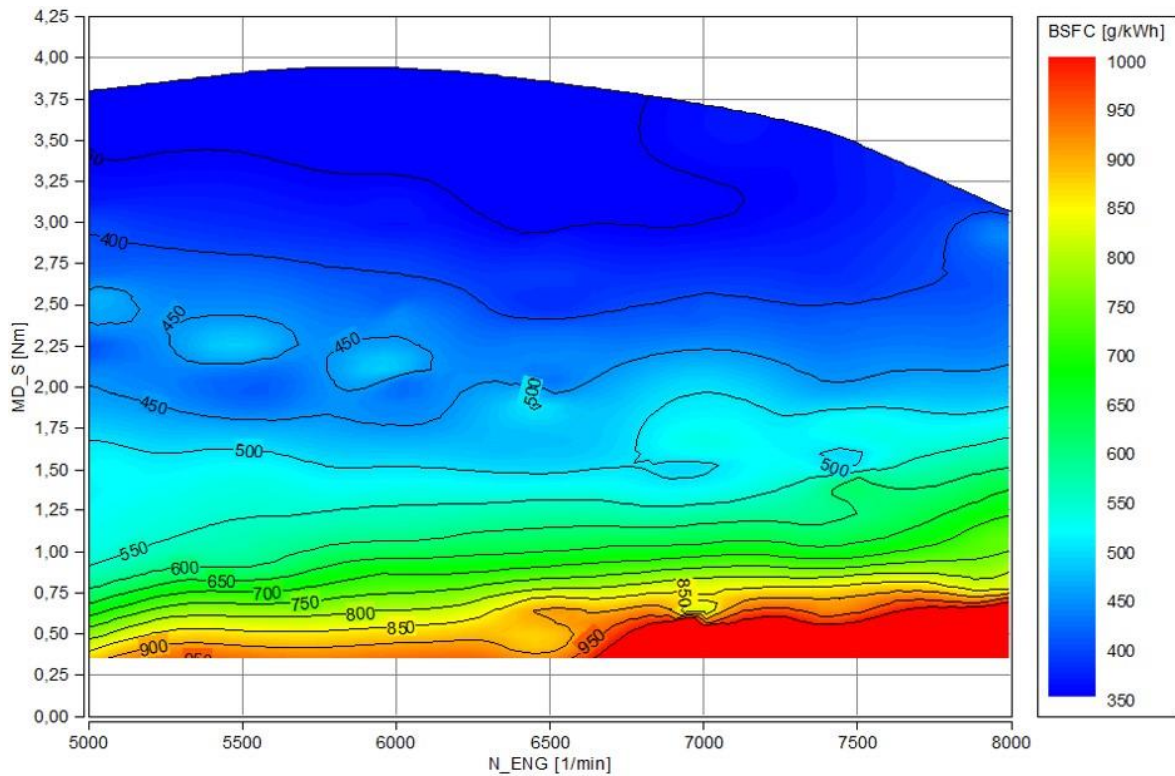


Figure 5-4: BSFC map magneto ignition

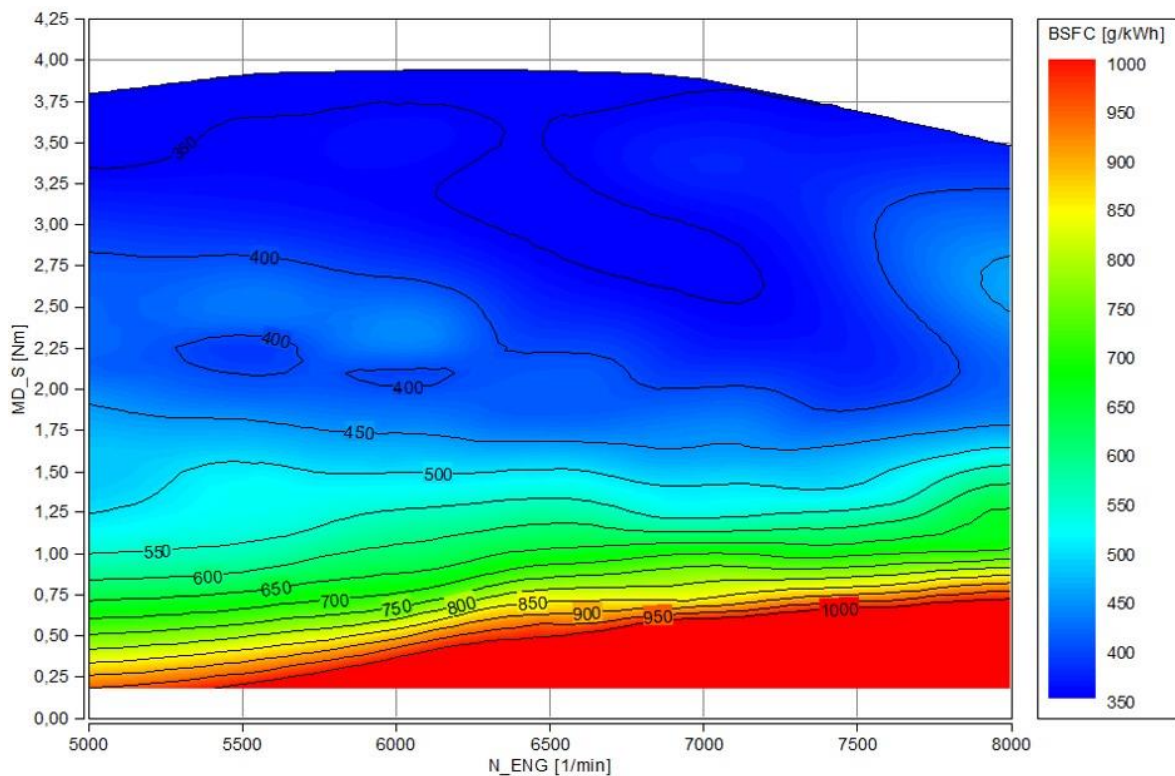


Figure 5-5: BSFC map battery coil ignition

The two BSFC maps are not only for the purpose of comparison, they are also very important to increase the accuracy of the simulation model.

5.2.3 Test setup carburettor change

The second comparison is showing the swap from the original carburettor to the M-tronic carburettor. Same as with the ignition change, the engine behaviour shall not alter due to the carburettor change. For both carburettor measurements the magneto ignition is used in order not to distort the gained results.

The M-tronic carburettor features a solenoid valve (Figure 2-11) which is able to control the excess air ratio and opens up the possibility of a fuel cut-off which was the main intention to use this carburettor. The fuel cut-off is needed in order to drive load cycles with the hybrid system where the option of an EM only operation is required. The driving of load cycles was not investigated in this master thesis, but the system shall provide the opportunity to do so (cf. chapter 7 Outlook).

The experimental investigations carried out on the M-tronic carburettor are confined to setting the excess air ratio to $\lambda = 0.8$ because of the original carburettor having roughly the same settings. Furthermore, the STIHL 4-Mix engine possesses its optimum performance at $\lambda = 0.8-0.85$. For those adjustments of the air-fuel ratio, the solenoid valve is controlled by the programmable ECU (MoTeC). The ECU is controlling this solenoid valve via a PWM signal. Since, the solenoid valve is generally open, the ECU is closing the valve in order to regulate the excess air ratio. The solenoid valve cannot be closed for too long, as lubrication of the valve train and crank drive must be ensured (cf. 3.1 – lubrication).

5.2.4 Results carburettor change

At first, the two generated excess air ratio maps (Figure 5-6 and Figure 5-7) are compared. The map created with the original carburettor shows that it is presumably only optimised for certain operating regions. Due to this, some points on the map reveal a slightly richer or leaner air-fuel mixture in comparison to the optimum $\lambda = 0.8-0.85$. The map measured with the M-tronic carburettor depicts a quite homogeneous air-fuel ratio because it was tuned using the MoTeC ECU. While tuning the M-tronic carburettor, fluctuations of lambda especially on points with higher torque were investigated. As these fluctuations could not be adequately controlled, the investigations on the M-tronic carburettor were terminated. Since the main reason for utilising the M-tronic carburettor was the fuel cut-off, no benefits are gained with this carburettor for the herein executed measurements on the hybrid system. Thus, for the measurements on the hybrid powertrain, the original diaphragm carburettor was used (cf. chapter 5.3).

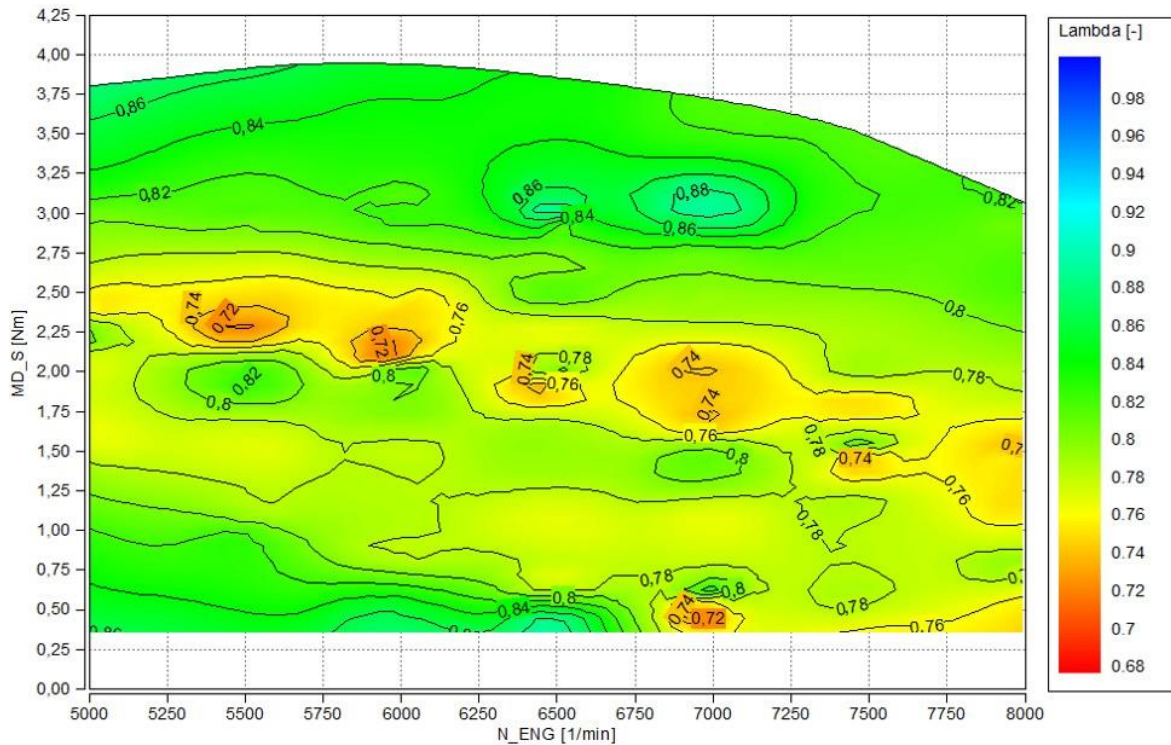


Figure 5-6: Lambda map with original carburettor

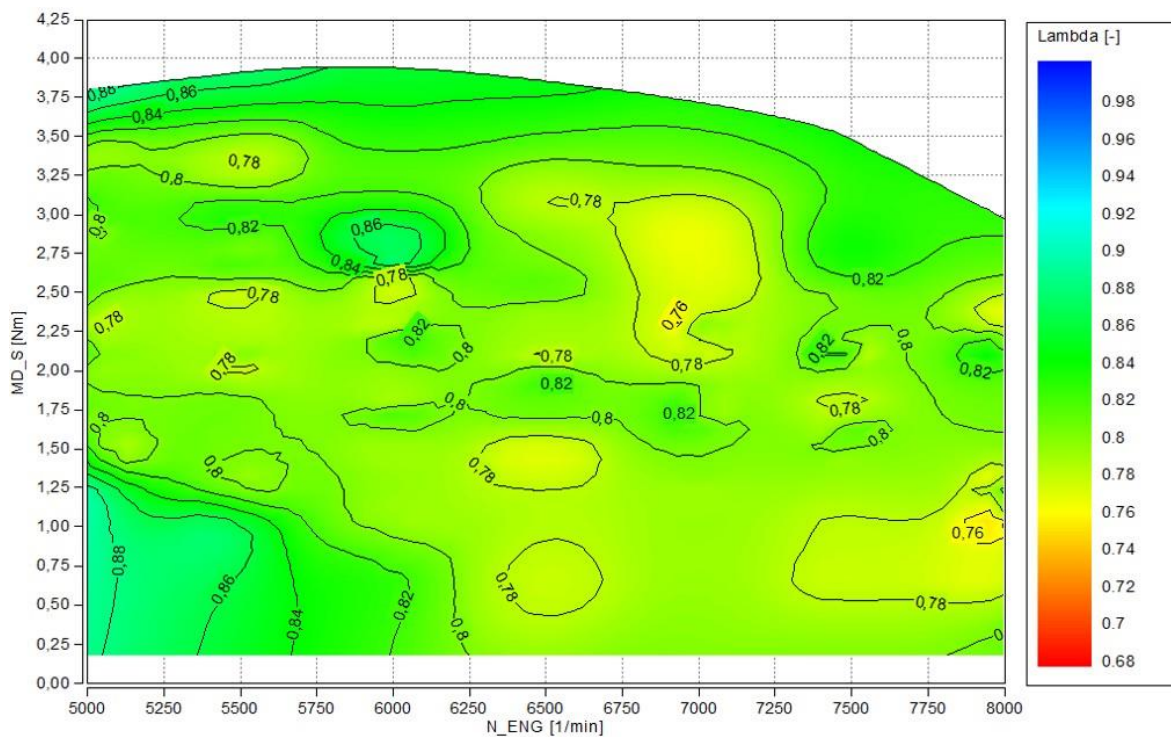


Figure 5-7: Lambda map with M-tronic carburettor

In order to find the best operational points in terms of specific fuel consumption, BSFC maps are created (Figure 5-8 and Figure 5-9). Both maps are showing the same tendency of a low BSFC at WOT, as expected. The map of the original carburettor is showing small areas of a higher BSFC at 2.25 Nm from 5500 up to 7500 rpm. Those areas are due to the factory settings of the original carburettor (Figure 5-6). The gained results are important for the hybrid system as the strategy is to run the ICE at its best operational line, thus highest efficiency (cf. Figure 1-8). Furthermore, the maps will be used to refine the simulation model.

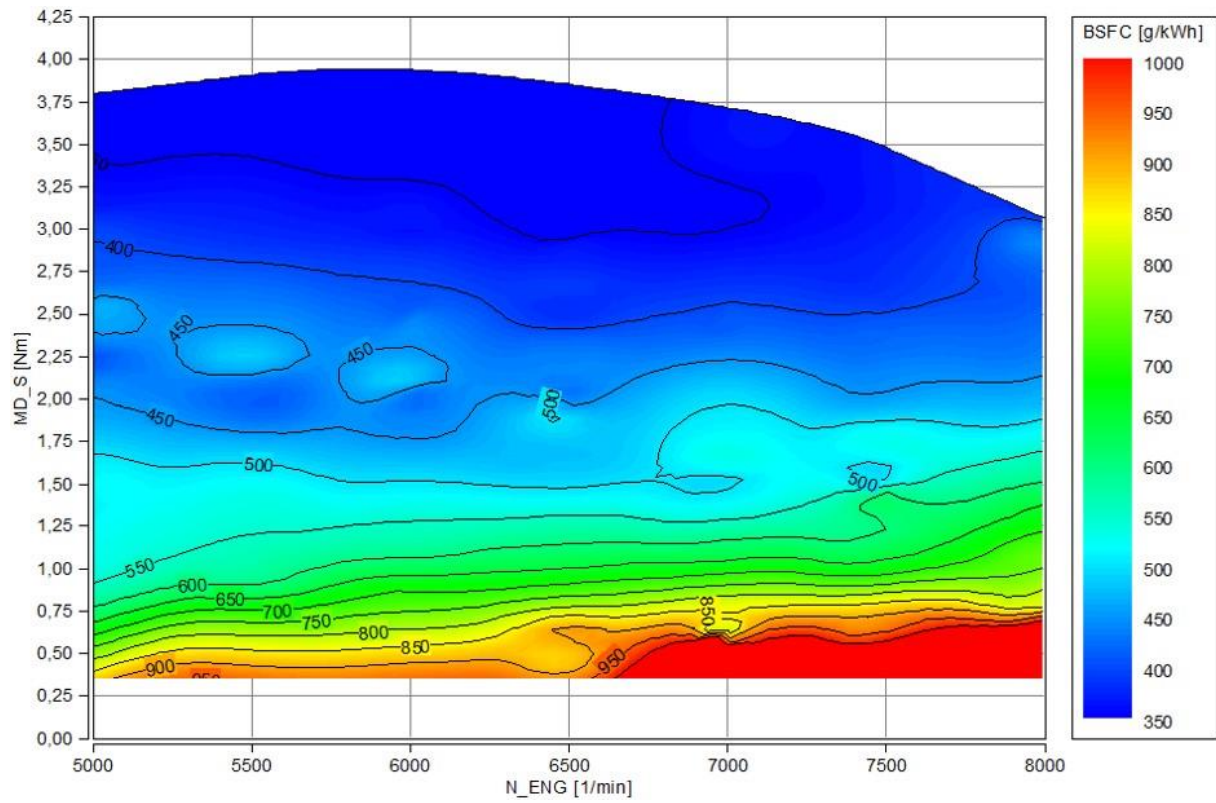


Figure 5-8: BSFC map with original carburettor

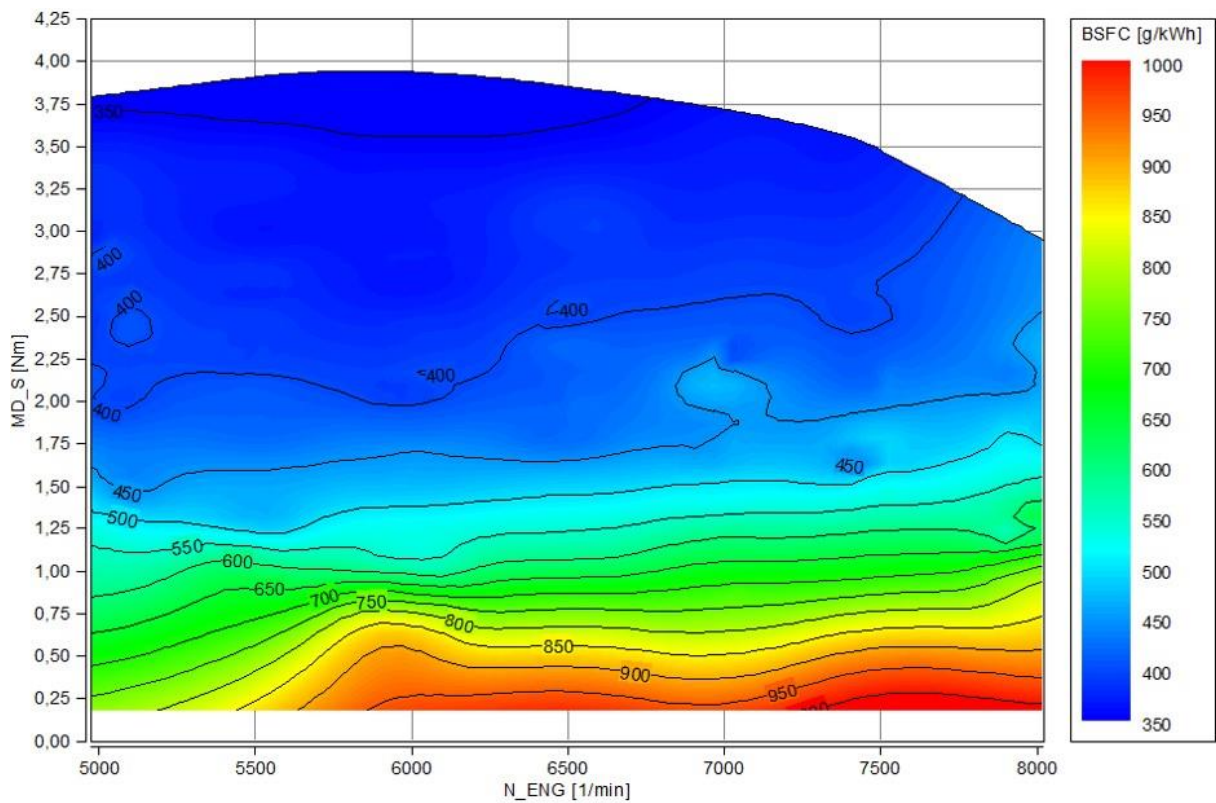


Figure 5-9: BSFC map with M-tronic carburettor

In Figure 5-10, the CO and HC emission maps for the M-tronic carburettor (a, b) and for the original carburettor (c, d) are shown. Similar to the fuel consumption, the emissions have their best regions at WOT. Since the excess air ratio is quite rich, the CO emissions are making the biggest part of the pollutants.

In the CO and HC emission maps of the original carburettor (c, d), the pattern of the lambda map can be recognised (Figure 5-6). This pattern is showing in the middle torque area a lambda between 0.72 and 0.74, thus a richer air-fuel ratio than in the rest of the map. Due to these richer areas the CO and HC emissions are higher in those points. A similar behaviour can be seen at 7000rpm and low torque where lambda is rich and therefore the CO and HC emissions are higher compared to the rest of the maps.

The CO and HC emission maps measured with the M-tronic carburettor reveal a pattern that is again very similar to the lambda map (Figure 5-7). In the low torques the lambda is going from lean to rich, hence the HC and CO emissions are moving from lower to higher values. These correlations are excellently displayed at 6000 rpm between 2.5 and 3 Nm. In this area the lambda is jumping from 0.78 to 0.86. Since the CO emissions are highly dependent on the air-fuel ratio, a jump from 400 to 200 g/kWh can be seen. The HC emission are showing similar tendencies, but not so clearly. In general, the emission maps of the M-tronic carburettor are conform to the identified lambda fluctuations, as described at the beginning of chapter 5.2.4. This applies in particular to the high torque range.

It must be mentioned that the delineated emission maps are showing the brake specific emissions. This means that the values in these maps are dependent on the output power, hence they are high in the low power range, compared to the volumetric exhaust emissions.

The NO_x emissions are, due to the rich air-fuel ratio of $\lambda = 0.8$, which results in a low combustion temperature, very small, therefore negligible and not shown.

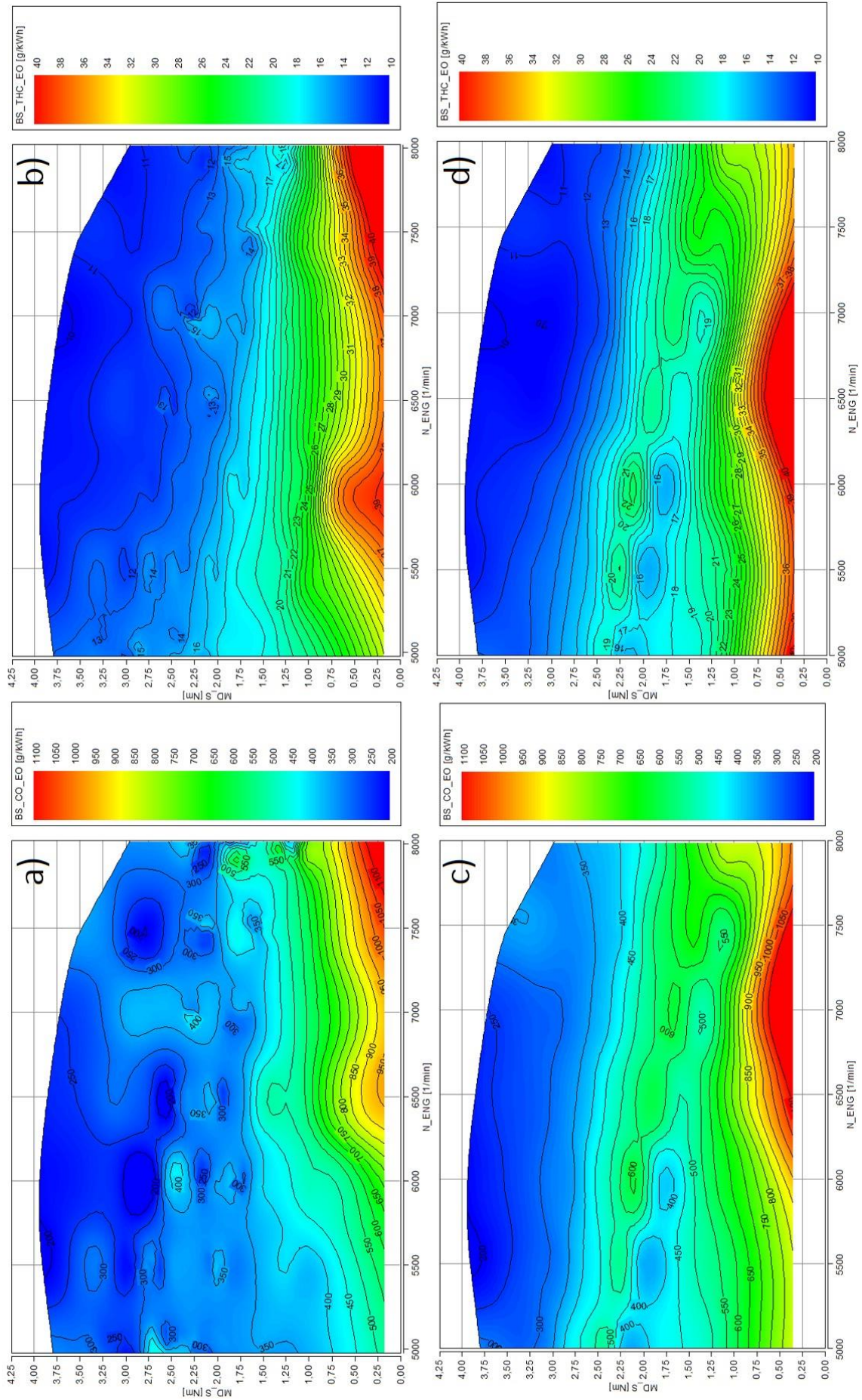


Figure 5-10: Brake specific CO and HC emissions

5.3 Parallel Hybrid System

Two different designs were examined on the parallel hybrid system. On both designs the ICE and the EM are directly coupled with no intermediate clutch (cf. 4.1.8 and 4.1.9). In line with these framework conditions, the test setup was defined as follows.

5.3.1 Test setup

In order to determine if the EM is able to start the ICE, measurements on the start-up have been carried out (5.3.3.1 Results from start-up). For those measurements, the engine was dragged without igniting.

To investigate whether the operating strategy from chapter 1.3 (left side in Figure 5-11) having the ICE at constant throttle and using the EM as a torque balancer is working with the built system, measurements were carried out using the method depicted on the right side in Figure 5-11.

To start those measurements, the EM is powered and starts to rotate which cranks up the ICE. Once the engine is started, it is revving up the system to 5000 rpm (speed at which the centrifugal clutch is fully engaged). The torque of the EM is set to zero and the ICE is set to a certain throttle angle. With these settings, the first point, where only the ICE delivers torque, is measured. For the next measurement points, the speed and the throttle angle are held constant and a positive or negative EM torque, in 0.5 Nm steps, is added. This results in one reference point where only the ICE delivers torque and in some points where the EM adds or subtracts torque (maximum six points).

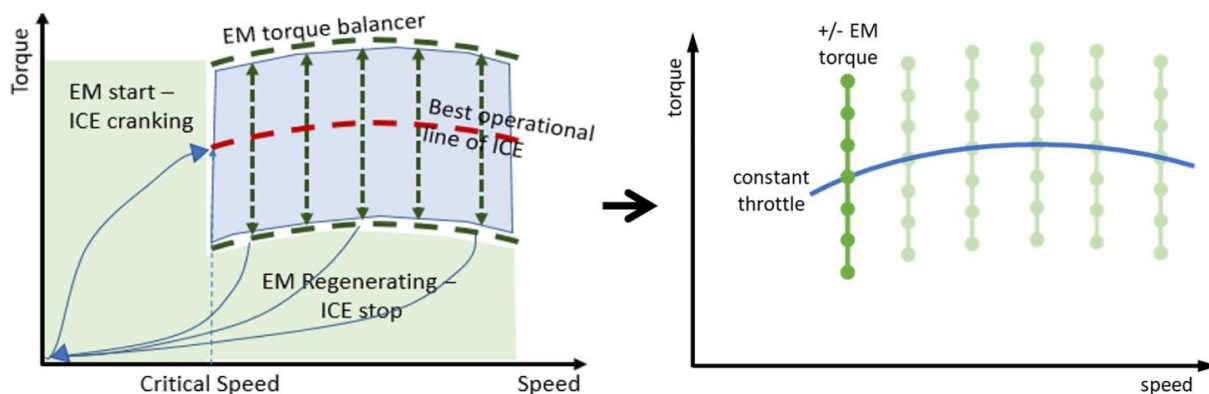


Figure 5-11: Operating strategy [36] and method for hybrid powertrain measurements

For the measurements, the ICE is equipped with the original diaphragm carburettor and the battery coil ignition controlled by MoTeC. The M-tronic carburettor was not used for the measurements, hence no fuel cut-off was possible. Since only steady-state points are measured, a fuel cut-off is not required. This means that no benefit would be gained with the M-tronic carburettor.

For controlling the EM, the RoboteQ ECU and the Regatron battery simulator were used. The battery simulator acts as a current source or an electrical load for the EM, depending if torque is added or subtracted. The EM torque is controlled by the RoboteQ ECU in a closed loop torque mode (cf. 3.4.1) and features a trapezoidal commutation (cf. 2.2.3). With those settings, the measurements were executed as already described above with the ICE at constant speed and throttle angle, and the EM adding positive or negative torque.

5.3.2 First design results

On the first design with the separated EM rotor and stator, no measurements have been made due to the following problems:

- The rotor and the stator touched each other at high rpm. This was probably caused by wobbling of the rotor due to its cantilevering connection to the crankshaft (Figure 5-12). Another possible reason is the production accuracy of the rotor-connector (No. 3 in Table 4-5). Since on this part the cone and the woodruff key together are milled from the solid, production tolerances are difficult to be accomplished. In addition, the tolerances on the stator mountings (No. 6 in Table 4-5) may be too imprecise and cause misalignment.
- Too much heat was coming from the exhaust muffler, hence the rotor was getting too hot and the permanent magnets lost their full magnetic force. This was noticed after a few test-runs with this configuration.

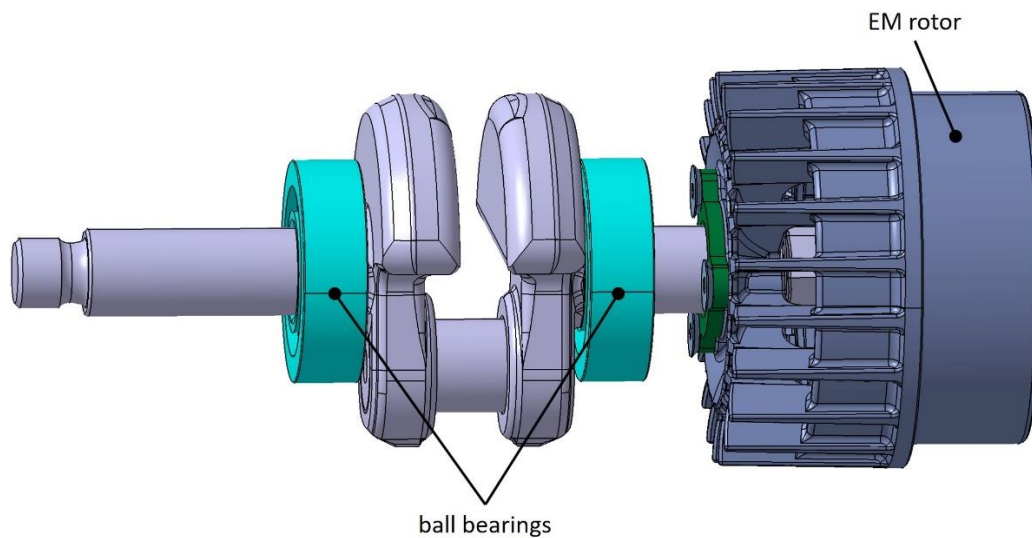


Figure 5-12: Crankshaft together with EM rotor

5.3.3 Second design results

The second design overcomes the two problems of the first design. For solving the problem of wobbling, the EM remains assembled with its shaft and bearings. In order to resolve the heat issue, the EM assembly is mounted with some distance to the ICE, and exhaust muffler respectively, to avoid thermal problems at the permanent magnets.

5.3.3.1 Results from start-up

In the course of the hybrid system measurements, the data of the start-ups have been recorded. The start-up of the hybrid system is the time from when the EM is powered, until the ICE is firing. In this case, the ICE was only spinning and not fired in order to have a closer look at the start-up process and its required power and energy. Over this time period the speed, phase current, battery current and battery voltage were measured. Those time-based measurements have been carried out with the software of the RoboteQ ECU.

Figure 5-13 delineates the recorded data from the start-up measurements. The first graph a) is showing the speed during the acceleration phase of four different start-ups. On each start-up the EM is rotating the ICE until it reaches a speed of around 3800 rpm. This speed is rather high since this engine is usually started with a pull starter, which can reach speeds up to 1000 rpm. The high speed was chosen to have a worst-case scenario and to investigate possible termination conditions for the start-up. A higher speed for those experiments could not be selected because of the centrifugal clutch, which is starting to engage with the eddy-current brake at around 3500 rpm (cf. Figure 4-12 including the description above the picture). At 2000 rpm the compression release device stops working, thus up to this speed the engine must have started.

It can be noted that the acceleration phase in order to achieve the 3800 rpm lasts on average 0.71 seconds, while the whole start-up procedure takes up to 2.6 seconds. This is due to the EM needing this small amount of time to overcome the compression pressure of the ICE and set it into motion. In order to reach 1000 rpm, it takes 2.05 seconds. About 0.15 seconds later 2000 rpm, at which the decompressor stops, are reached. At latest by then, the ICE must have started.

Graph b) shows the phase current, battery current and battery voltage during the start. By multiplying the battery current with the battery voltage, the maximum required power for the start-up is identified (graph c)). In the fourth graph d) the average of the required EM power for starting is shown, with the maximum power roughly at 900 Watt. Furthermore, the cumulated energy consumption for the start-up is depicted in graph d). Assuming that the starting speed is somewhere close to 1000 rpm, the required power for the start-up is about 260 W and the consumed energy amounts to 210 J. The required power and energy consumption are giving a good view of the hybrid system starting process and help to increase the accuracy of the simulation model. Moreover, the gained data from the start-up are needed for further steps, such as the design of a suitable ESS.

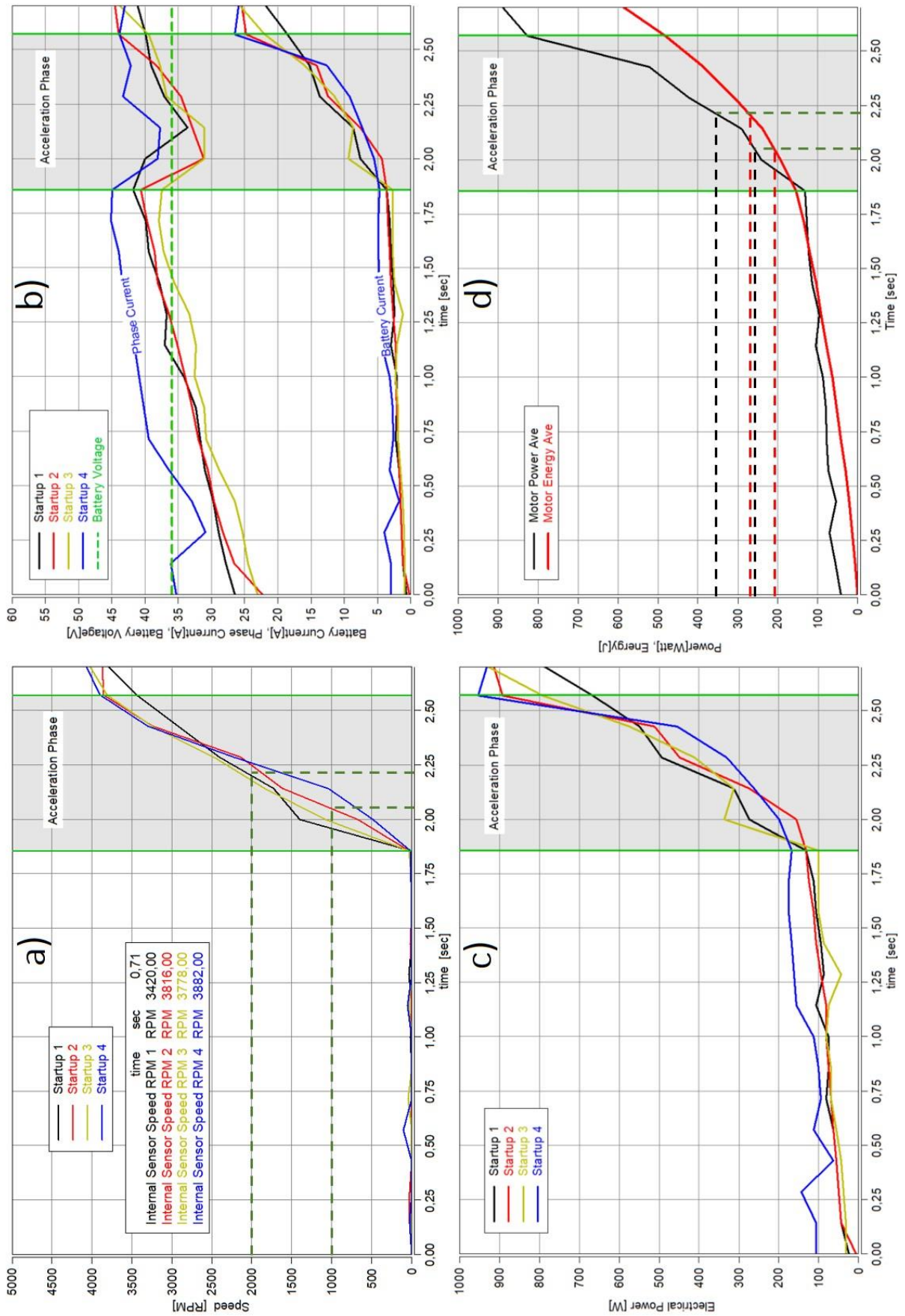


Figure 5-13: Start-up measurements of the hybrid system

5.3.3.2 Results from steady-state measurements

The first map resulting from the steady-state measurements is depicted in Figure 5-14. This map is showing the efficiency of the electric motor at different torque and speed. This efficiency is calculated from the EM power together with the current and voltage measured by the battery simulator. This means that the efficiency of the RoboteQ ECU and its power electronics is included. Not considered are the charging and discharging losses of an ESS.

The map is showing the EM efficiency, but shifted by the torque of the ICE at constant throttle angle (cf. Figure 5-11 Method for hybrid powertrain measurements). This means that the white line in the middle is showing the torque of the combustion engine alone. At this white line, the EM efficiency is zero, as it produces no torque. Below the white line the EM is working as a generator and above as a motor. On the measurement points where torque is added, the efficiency is between 0.76 and 0.95. It can be seen that the efficiency is going slightly down with the EM torque going up. This behaviour in general is common for electric motors. Furthermore, as the speed increases, the efficiency becomes higher, which is to be expected as the EM is running below its nominal speed where it can deliver its maximum torque. A similar behaviour can be noticed by looking at the region of the EM subtracting torque. As more torque is subtracted, the efficiency becomes slightly lower, and with increasing speed, the efficiency is getting higher. The range of the measured points is going from 0.67 to 0.95. In general, the efficiency in the area of negative EM torque is somewhat weaker compared to the region of torque being added. This can be explained by the fact that for recuperation below the nominal speed, a BLDC motor needs power electronics to balance the voltage difference between the motor and the battery.

Furthermore, in Figure 5-14 only slightly less than 50 points were measured, thus, the resolution is low, and, the area around 0 Nm EM torque and some of the isolines are wavy.

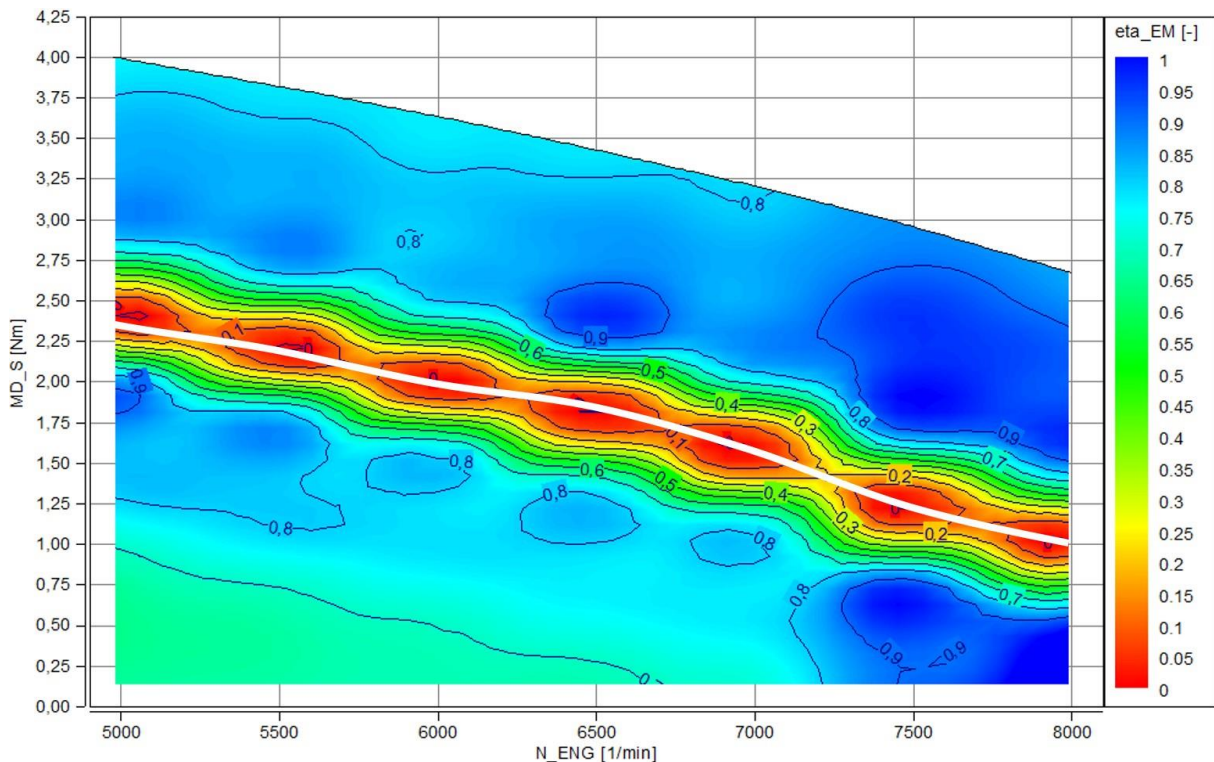


Figure 5-14: Efficiency of the EM

After the map of the electric motor efficiency was created, a combined efficiency of the EM and the ICE shall be calculated. This calculation is carried out in order to make a statement about the efficiency of this hybrid configuration and for a comparison with the efficiency map of the combustion engine.

In order to calculate a combined efficiency of the engine and the motor, two different cases must be distinguished. In the case where the EM is working as a motor, the combustion engine and the electric motor are producing torque to overcome the external load. This case is depicted on the left side in the figure below. The green arrows are showing the input energy into the hybrid system and the red arrow the output energy for driving the external load. The efficiency in this case is calculated according to equation (5-1).

In the second case, the EM is acting as a generator. Therefore, the power coming from the ICE is divided into mechanical power for the external load and mechanical power that is converted into electrical power by the EM. This working mode is illustrated on right side in the figure below. Similar to the above-described picture on the left, the green arrow is showing the input energy into the hybrid system and the red arrows are showing the output energy. The calculation of the efficiency in this case is done pursuant to equation (5-2).

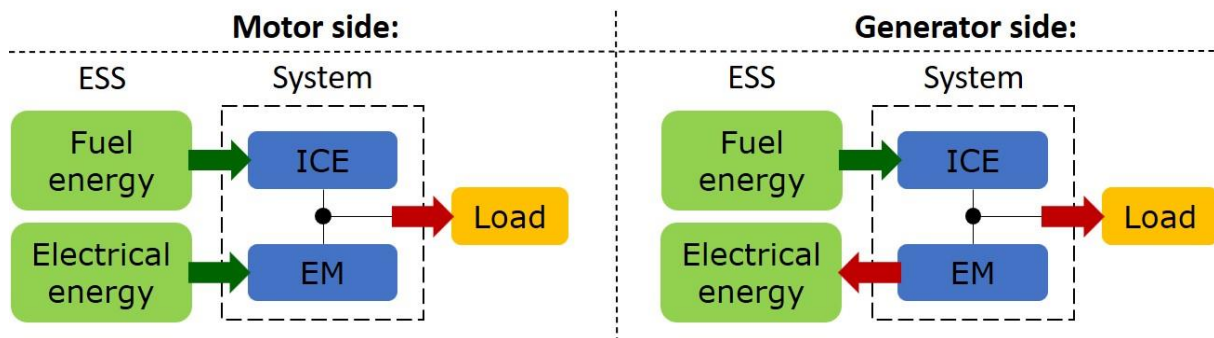


Figure 5-15: Power flow of the hybrid powertrain

$$\eta_{ICE+EM} = \frac{P_{mech}}{P_{fuel} + P_{el}} = \frac{T * 2\pi * n}{\dot{m}_{fuel} * H_u + U * I} \quad (5-1)$$

$$\eta_{ICE+EM} = \frac{P_{mech} + P_{el}}{P_{fuel}} = \frac{T * 2\pi * n + U * I}{\dot{m}_{fuel} * H_u} \quad (5-2)$$

Figure 5-16 illustrates the combined efficiency of the engine at constant throttle and the electric motor adding, respectively subtracting torque. The white curve is the torque curve of the ICE alone without any EM torque being added. Since the engine is throttled, the torque and the efficiency at this curve are going down with the speed increasing. The engine is throttled in order to simulate a smaller ICE. This is done because only one combustion engine is used for both measurements (ICE alone and hybrid system). Furthermore, the maximum torque of the hybrid system is than close to the maximum torque of the ICE and the two powertrains can be compared.

The efficiency of the throttled engine on the lower speeds is around 22% which is rather high for such a small ICE in part load. This can be explained by the external cooling, as this power does not have to be provided by the combustion engine. This actuality explains also the efficiency of the ICE alone (Figure 5-17), which is rather high for a combustion engine of a hand-held power tool. By looking above the white curve in Figure 5-16, an increase in the efficiency can be seen, due to the EM adding torque at high efficiency (cf. Figure 5-14). Below the white throttle line, the EM is working as a generator. This means that some of the mechanical energy of the crankshaft is converted into electrical energy. Due to the fact that every energy conversion has losses, the efficiency on the generator side is lower compared to the efficiency at the ICE throttle line.

Comparing the efficiency map of the herein investigated hybrid configuration (Figure 5-16) to the efficiency of the engine alone (Figure 5-17), it can be seen that in the whole map the efficiency can be slightly increased. In order to achieve this high efficiency, so to stay with the hybrid system on the very high or low torque points, a big battery would be required. The big battery would be needed to either supply the EM with electric energy or to storge electric energy, at any time. Since the battery for such a hand-held tool has to be small, the electric motor cannot drive or regenerate for a long period at a time. Thus, the potential benefits of the hybrid powertrain are on the high transients, as shown in the beginning (Figure 1-6 including description below). Furthermore, the load cycle of the power tool must fit to the hybrid configuration. This means that the average torque of the load cycle must meet the torque of the engine at the constant throttle curve. The engine is than working at a constant throttle curve and the motor is following the transient torque of the load cycle. Therefore, the hybrid powertrain has to reach the maximum required power of the load cycle, and the EM must be able to break the ICE to low torque points for following the load cycle (cf. Figure 1-6 – normalised torque).

In this operational strategy the EM shall add and subtract the same amount of energy over the whole load cycle. If this can be gained, the SoC of an ESS will be roughly the same at the beginning and the end of the load cycle. Due to energy losses in the EM, and in the ESS while charging and discharging, the torque of the ICE must be higher than the average torque of the load cycle.

Recapitulatory, a potential increase in the efficiency can be achieved by utilising the hybrid configuration. However, in order to determine whether this potential advantage in efficiency proves true, load cycles must be driven with the hybrid system.

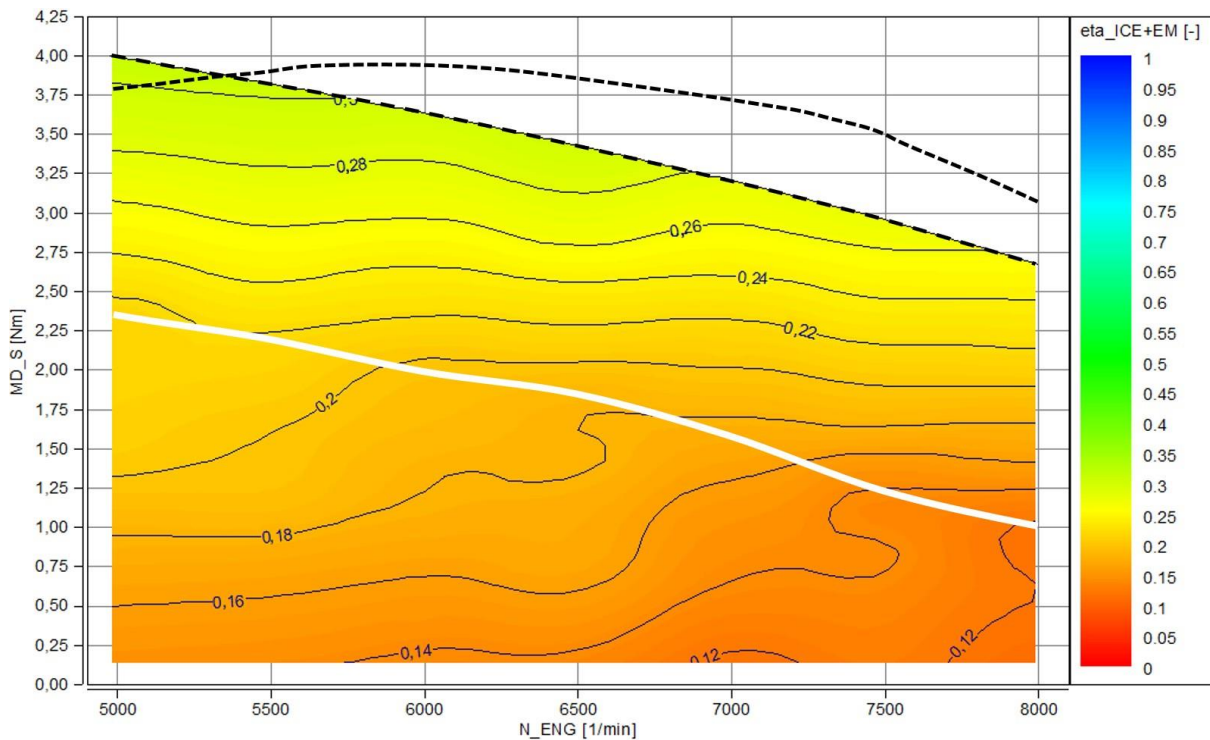


Figure 5-16: Combined efficiency of EM and ICE, including WOT curve of ICE

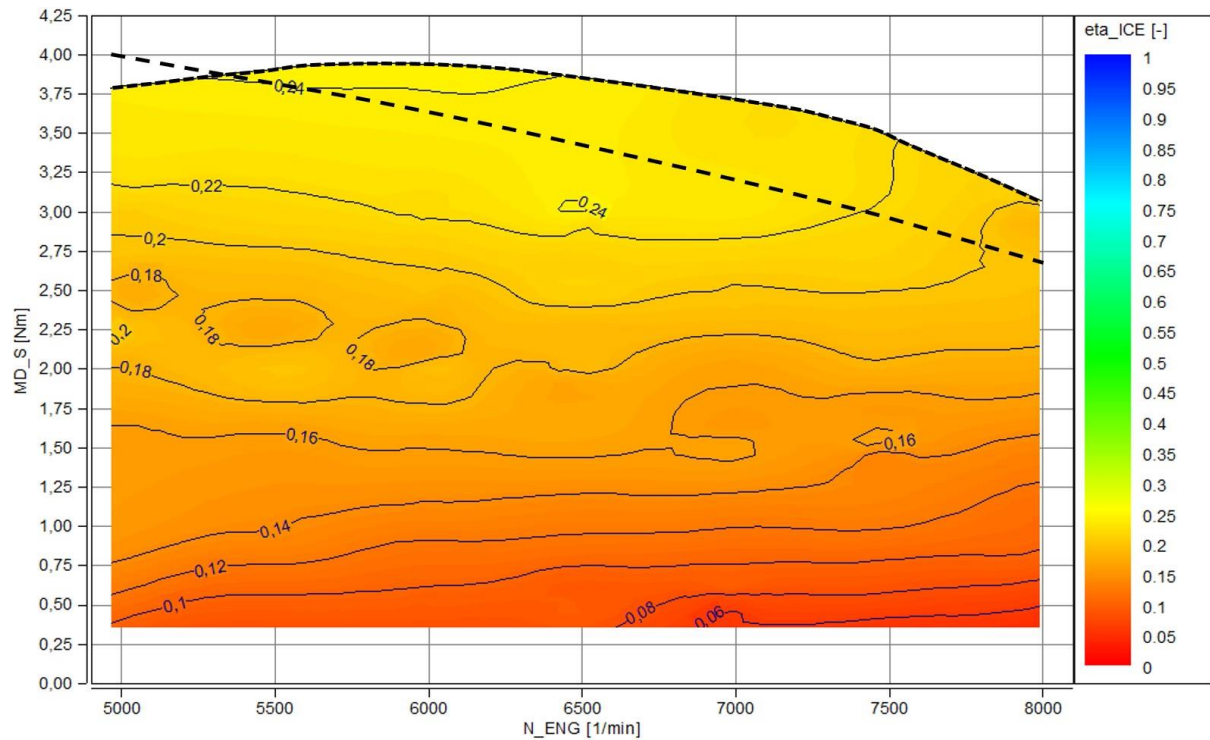


Figure 5-17: Efficiency of the ICE, including maximum torque curve of EM + ICE

6 Conclusions

Out of the first tests of the ICE alone together with the small clutch assembly mounted on the test bench, the high torque peaks of a single cylinder four-stroke engine could clearly be ascertained. Furthermore, it could be determined that this engine needs forced-air cooling blowing directly on the cooling fins.

The experiments on the ICE with the change from the magneto ignition to the battery coil ignition were showing only minor changes in the engine behaviour. Therefore, it can be concluded that this modification can be done without disturbances. Moreover, due to the measurements of BSFC maps, the best operational line at WOT could be confirmed and the simulation model can be refined. The swap from the original carburettor to the M-tronic carburettor could not be adequately controlled and needs further investigations or a different way of managing a fuel cut-off.

The investigations done with the first hybrid design are showing that the EM rotor, respectively the permanent magnets are temperature sensitive. Hence, the EM rotor requires some heat protection or cooling, or some more distance to the ICE, especially to the exhaust muffler. Another reason for this design not to work were the difficulties in keeping the air gap between rotor and stator due to wobbling of the rotor and production tolerances.

On the second hybrid design, the problems of the first design are solved. The experiments could confirm that the start-up of the ICE, by powering and controlling the EM is possible. Furthermore, the operational strategy of running the ICE with constant throttle and adding or subtracting torque with the EM is working. The efficiency of this hybrid configuration could be slightly increased compared to the ICE for stationary points. Since those hand-held power tools operate in a highly transient manner, load cycles must be driven in order to make a statement about achieving a higher efficiency with this hybrid powertrain.

7 Outlook

Subsequent to this master thesis, the measured data will be put into the simulation model in order to enhance its accuracy and to investigate possible efficiency benefits. Furthermore, with the aid of the simulation, the optimum hybrid powertrain for such a hand-held power tool shall be figured out. After the simulation, the next step on the test bench would be driving load cycles to investigate possible BSFC and emission improvements. Therefore, a different way for the fuel cut-off has to be found, or continuing investigations on the M-tronic carburettor are to be done. The cooling of the ICE requires further examination, especially if a demonstrator tool with this hybrid powertrain shall be built. Also, the dimensioning of an ESS is necessary for building a demonstrator.

References

- [1] Brettschneider, J.: "Berechnung des Luftverhältnisses von Luft-Kraftstoff-Gemischen und des Einflusses von Meßfehlern", Bosh Technische Berichte Band 6, 1979
- [2] Eichlseder, H.: „Kolbenmaschinen“, Lecture notes, Technische Universität Graz, 2014
- [3] Eichlseder, H.: „Verbrennungskraftmaschinen Vertiefte Ausbildung“, Lecture notes, Technische Universität Graz, 2012
- [4] Eifler, W., Schlücker, E., Spicher, U., Will, G.: "Küttner Kolbenmaschinen - Kolbenpumpen, Kolbenverdichter, Brennkraftmaschine", Springer-Verlag, 2009, 7. Auflage, ISBN 978-3-8351-0062-6
- [5] Flexparts GmbH. <https://www.flexparts.de/> [Online] [Cited: May 26th,2021] <https://www.flexparts.de/STIHL-Elektromotor-original-Ersatzteil-1254-600-0200-12546000200>
- [6] Groskopf, G.: "SWN 13040 Normnamen und Berechnungsformeln für motorische Größen", STIHL AG & Co. KG, (Hrsg.), 2016
- [7] Handelsblatt GmbH. <https://www.handelsblatt.com/> [Online] [Cited: April 1st, 2021] <https://www.handelsblatt.com/unternehmen/mittelstand/familienunternehmer/erfolgreiches-geschaeftsjahr-stihl-setzt-jetzt-auf-akku-motorsaegen/19715384.html>
- [8] Hearst Magazine Media, Inc. <https://www.popularmechanics.com/> [Online] [Cited: April 2nd,2021] <https://www.popularmechanics.com/home/tools/a28522787/battery-powered-chainsaws/>
- [9] Hirz, M.: "Innovative Power Trains", Lecture notes, Technische Universität Graz, 2020
- [10] Hughes, A., Drury, B.: "Electric Motors and Drives - Fundamentals, Types and Applications", Newnes, 2019, Fifth Edition
- [11] Khajepour, A., Fallah, S., Goodarzi, A.: "Electric and Hybrid Vehicles - Technologies, Modeling And Control: A Mechatronic Approach", Wiley, 2014, ISBN 9781118341513
- [12] Laimböck, F.: „Zweiradtechnik und Kleinmotoren“, Lecture notes, Technische Universität Graz, 1996
- [13] Mader, S.: "Potentialuntersuchung zur Regelung mager betriebener 4-Mix Motoren“, Master Thesis, Universität Stuttgart, 2016
- [14] MoTeC Pty Ltd. <https://www.motec.com.au/> [Online] [Cited: May 18th,2021] <https://www.motec.com.au/downloads/downloaddatasheets/CDS13150 M150 ECU.pdf>
- [15] Pischinger, R.; Klell, M.; Sams, Th.: „Thermodynamik der Verbrennungskraftmaschine“, 3. Auflage. In der Reihe: List, H. (Hrsg.): Der Fahrzeugantrieb. Springer

- Verlag Wien New York, ISBN 9783211992760, 2009
- [16] Raiffeisen-Lagerhaus GmbH. <https://lagerhaus.at/> [Online] [Cited: May 26th,2021] https://lagerhaus.at/shop/p/BaseProduct_1048014/27841984?standort=1&gclid=EAIaIQobChMI76_6z5rn8AIVmPhRCh3XyAAqEAQYASABEgK7VPD_BwE
- [17] RC-LowCAP. <https://rc-lowcap.at/> [Online] [Cited: May 12th,2021] <https://www.rc-lowcap.at/research/projects/>
- [18] RINGFEDER POWER TRANSMISSION. <https://www.ringfeder.com/de/> [Online] [Cited: May 6th, 2021] <https://www.ringfeder.com/globalassets/downloads/02-product-paper/product-paper-tech-paper-ringfeder-klauenkupplungen-gwe-tnm-tns-tnb-de-04-2020.pdf>
- [19] Robert N. Brady, “Internal Combustion (Gasoline and Diesel) Engines,” 2004, ISBN 9780121764807, <https://doi.org/10.1016/B0-12-176480-X/00089-9>
- [20] Roboteq, Inc. <https://www.roboteq.com/> [Online] [Cited: May 18th,2021] <https://www.roboteq.com/products/products-brushless-dc-motor-controllers/sbl2360t-detail>
- [21] Roboteq, Inc. <https://www.roboteq.com/> [Online] [Cited: May 18th,2021] <https://www.roboteq.com/docman-list/motor-controllers-documents-and-files/documentation/datasheets/sbl23xx-datasheet/829-sbl23xx-datasheet-1/file>
- [22] Roboteq, Inc. <https://www.roboteq.com/> [Online] [Cited: May 18th,2021] <https://www.roboteq.com/docman-list/motor-controllers-documents-and-files/documentation/user-manual/924-roboteq-controllers-user-manual-v2-1/file>
- [23] RS Components GmbH. <https://de.rs-online.com/> [Online] [Cited: May 10th,2021] <https://de.rs-online.com/web/p/bewegungssensoren/0285756/>
- [24] Schacht, H.: “Entwurf & Untersuchung eines neuartigen elektrischen Antriebs mit VKM-Unterstützung für ein Zweirad-Stadtfahrzeug“, Dissertation, Technische Universität Graz, 2019
- [25] STIHL Holding AG & Co. KG. <https://www.stihl.at/> [Online] [Cited: April 2nd,2021] <https://www.stihl.at/STIHL-Produkte/Motors%C3%A4gen/Benzin-Motors%C3%A4gen-f%C3%BCr-die-Forstwirtschaft/2122436-130/MS-881.aspx>
- [26] STIHL Holding AG & Co. KG. <https://www.stihl.at/> [Online] [Cited: April 2nd,2021] <https://www.stihl.at/STIHL-Produkte/Reinigungsger%C3%A4te/Blasger%C3%A4te-und-Saugh%C3%A4cksler/R%C3%BCckentragbare-Blasger%C3%A4te/295832-1720/BR-800-C-E.aspx>
- [27] STIHL Holding AG & Co. KG. <https://www.stihl.at/> [Online] [Cited: April 2nd,2021] <https://www.stihl.at/STIHL-Produkte/Motorsensen-und-Freischneider/Elektro-Motorsensen/21479-1593/FSE-81.aspx>
- [28] STIHL Holding AG & Co. KG. <https://www.stihl.at/> [Online] [Cited: April 2nd,2021] <https://www.stihl.at/STIHL-Produkte/Motorsensen-und-Freischneider/Akku-Motorsensen/276265-1650/FSA-130-R-ohne-Akku-und-ohne-Ladeger%C3%A4t.aspx>

- [29] STIHL Holding AG & Co. KG. <https://www.stihl.at/> [Online] [Cited: April 2nd,2021] <https://www.stihl.at/stihl-produkte.aspx>
- [30] STIHL Holding AG & Co. KG. <https://www.stihl.at/> [Online] [Cited: May 17th,2021] <https://www.stihl.at/STIHL-Produkte/Reinigungsger%C3%A4te/Blasger%C3%A4te-und-Saugh%C3%A4cksler/R%C3%BCckentragbare-Blasger%C3%A4te/2851-1720/BR-600.aspx>
- [31] STIHL Holding AG & Co. KG. <https://www.stihl.at/> [Online] [Cited: May 25th,2021] <https://www.stihl.at/spezialkraftstoff-stihl-motomix.aspx>
- [32] STIHL Vertriebszentrale AG & Co. KG. <https://www.stihl.de/> [Online] [Cited: May 17th,2021] <https://www.stihl.de/de/technologie/motorentechnik/4-mix-motor>
- [33] Stone, R.: “Introduction to Internal Combustion Engines”, Palgrave Macmillan, 2012, 4th edition, ISBN 978-0-230-57663-6
- [34] Trattner, A., Schmidt, S., Kirchberger, R., Eichlseder, H. et al., "Future Engine Technology in Hand-Held Power Tools," SAE Int. J. Engines 5(4):1912-1929, 2012, <https://doi.org/10.4271/2012-32-0111>
- [35] van Basshuysen, R., Schäfer, F.: „Internal Combustion Engine Handbook - Basics, Components, Systems and Perspectives”, SAE International, 2002, ISBN 0-7680-1139-6
- [36] Vogiatzis, D., Schacht, H., Schmidt, S., and Kirchberger, R., "A Concept Investigation Simulation Model on Hybrid Powertrains for Handheld Tools," SAE Technical Paper 2020-32-2316, 2020, <https://doi.org/10.4271/2020-32-2316>
- [37] Yedamale, P.: “Brushless DC (BLDC) Motor Fundamentals”, Technical Report - AN885, Microchip Inc., 2004

Figures

Figure 1-1: Requirements on hand-held power tools [34].....	3
Figure 1-2: Two-stroke powered chainsaw and four-stroke driven leaf blower [25],[26]	3
Figure 1-3: Electric brush cutter with power cord and battery powered grass trimmer [27],[28]	4
Figure 1-4: RC-LowCAP projects [17]	4
Figure 1-5: hybrid tool simulation model [36].....	5
Figure 1-6: Normalised speed and torque of a hand-held power tool [36].....	5
Figure 1-7: Parallel hybrid configuration [36]	6
Figure 1-8: Operating strategy for parallel hybrid system [36]	6
Figure 2-1: Curve of forces and moments vs. CA of a single cylinder four-stroke engine [2] ..	7
Figure 2-2: Cylinder pressure over swept volume [33].....	8
Figure 2-3: <i>bsfc</i> and <i>bmep</i> for different excess air ratios [35]	10
Figure 2-4: Mixture calorific value versus excess air ratio [15]	11
Figure 2-5: Cylinder pressure and cumulative heat release curve [35].....	13
Figure 2-6: Influence of ignition angle on the pressure curve [35].....	13
Figure 2-7: Influence of air fuel ratio to mean effective pressure and fuel consumption [2]...	14
Figure 2-8: Cyclical fluctuations [35]	14
Figure 2-9: Emission behaviour of an SI engine depending on excess air ratio [2]	15
Figure 2-10: Diaphragm carburettor [13]	15
Figure 2-11: STIHL M-tronic carburettor [13]	16
Figure 2-12: Coil ignition [2].....	17
Figure 2-13: Magneto ignition [2].....	17
Figure 2-14: BLDC motor [22].....	18
Figure 2-15: Hall sensor sequence, output torque and direction of current [37]	20
Figure 2-16: Different hybrid configurations [36]	21
Figure 3-1: 4-Mix engine from STIHL BR 600 leaf blower [16]	22
Figure 3-2: Mixture lubrication on the STIHL 4-Mix engine [13]	22
Figure 3-3: BLDC motor supplied by STIHL [5]	23
Figure 3-4: MoTeC M150 [14]	24
Figure 3-5: RoboteQ SBL2360 [20].....	24
Figure 3-6: Open loop mode [22].....	25
Figure 3-7: Closed loop speed mode [22].....	25
Figure 3-8: Closed loop torque mode [22].....	25
Figure 4-1: Mounting points ICE and air intake box	27

Figure 4-2: Differences between reference ICE and modified ICE	27
Figure 4-3: Changes from modified ICE to hybrid system	28
Figure 4-4: Test bench.....	28
Figure 4-5: Assembly for mounting the ICE	29
Figure 4-6: Assembly for mounting the ICE (incl. bolts).....	30
Figure 4-7: Test bench together with ICE mounting assembly	30
Figure 4-8: Test bench together with ICE	31
Figure 4-9: Connection between crankshaft and eddy-current brake.....	32
Figure 4-10: Connection between crankshaft and eddy-current brake (assembled)	33
Figure 4-11: Sectional drawing of the clutch assembly	34
Figure 4-12: Sectional drawing of the clutch assembly including the torque flow.....	34
Figure 4-13: Comparison of the two clutch assemblies	35
Figure 4-14: Baseline ICE setup with big elastomer jaw coupling.....	36
Figure 4-15: Magnetic speed sensor assembly	37
Figure 4-16: Magnetic speed sensor mounting	37
Figure 4-17: Fan casing of the full blower tool.....	38
Figure 4-18: Cooling flow	38
Figure 4-19: Cooling shroud.....	39
Figure 4-20: Cooling pipes	39
Figure 4-21: Coupling of the EM rotor to the crankshaft.....	40
Figure 4-22: Coupling of the EM stator to the ICE.....	40
Figure 4-23: EM alignment.....	41
Figure 4-24: Coupling of the EM to the ICE	43
Figure 4-25: Measurement setup for reference ICE	44
Figure 4-26: Pressure sensor and magnetic sensor for synchronisation.....	46
Figure 4-27: Magnetic sensor and gear wheel	46
Figure 4-28: Measurement setup for modified ICE	47
Figure 4-29: Measurement setup for hybrid system.....	48
Figure 5-1: Modified air intake box	49
Figure 5-2: WOT comparison	50
Figure 5-3: Heat release curves at 8000 rpm WOT.....	51
Figure 5-4: BSFC map magneto ignition.....	52
Figure 5-5: BSFC map battery coil ignition	52
Figure 5-6: Lambda map with original carburettor	54
Figure 5-7: Lambda map with M-tronic carburettor	54
Figure 5-8: BSFC map with original carburettor	55

Figure 5-9: BSFC map with M-tronic carburettor	55
Figure 5-10: Brake specific CO and HC emissions	57
Figure 5-11: Operating strategy [36] and method for hybrid powertrain measurements	58
Figure 5-12: Crankshaft together with EM rotor	59
Figure 5-13: Start-up measurements of the hybrid system	61
Figure 5-14: Efficiency of the EM	62
Figure 5-15: Power flow of the hybrid powertrain	63
Figure 5-16: Combined efficiency of EM and ICE, including WOT curve of ICE	65
Figure 5-17: Efficiency of the ICE, including maximum torque curve of EM + ICE	65

Tables

Table 3-1: Technical data STIHL BR 600 [30]	23
Table 3-2: Technical data STIHL BLDC motor	24
Table 4-1: BOM – ICE mounting plate	31
Table 4-2: BOM – small clutch assembly	33
Table 4-3: Torque rating of the elastomer jaw couplings [18]	35
Table 4-4: BOM – large clutch assembly	36
Table 4-5: BOM – EM, first design	42
Table 4-6: BOM – EM, second design	43
Table 4-7: Sensors and actuators for carrying out measurements	45

Appendix

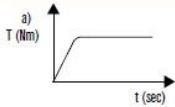
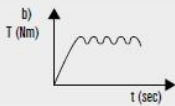
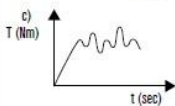
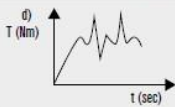
RINGFEDER Elastomer Jaw Couplings [18]

Dimensioning of the coupling



Drive side	Min. load factor S_A
E-Motor, turbine	1
Hydraulic motor	1,1
Combustion machine 4 and more cylinders, U-degrees $\leq 1:100$	1,2 (TVA)*
Combustion machine 1 to 3 cylinders, U-degree $> 1:100$	1,4 (TVA)*

S_A = Load factor of drive side: * We recommend for drivers with combustion machines to examine by a „TVA“ - torsiona vibration calculation which coupling is suitable for the application.

Torque characteristics at operating point on outside	Torque characteristics	Minimum load factor S_L
Constant, uniform without torque variation		1
Uniform with little variations, slight shocks		1,25
Non-uniform, also API-671, API-610 moderate shocks		1,5
Non-uniform, fluctuant, heavy shocks		1,75
Other torque characteristics		Own specification/ personal vibration calculation

S_L = Load factor of output side

Ambient temperature range [°C]	Temperature factor S_θ for elastic parts		
	RINGFEDER® GWE PUR, Hytel ¹⁾	RINGFEDER® TNM, TNS, TNB VkR, VkW, Vk60D	
		Pb72, Pb82 (NBR)	
-30 < ϑ < +30	1	1	
+30 < ϑ < +40	1,2	1,2	
+40 < ϑ < +60	1,4	1,4	
+60 < ϑ < +80	1,8	1,8	
+80 < ϑ < +100	2	-	
+100 < ϑ < +120	2,4	-	

S_θ = Temperature factor depending on elastic materials. The elastic material may not be used in temperature ranges marked with a dash (-).

¹⁾ The maximum permissible ambient temperature in the chapter 'Technical description (Jaw Couplings RINGFEDER® GWE)' must be strictly observed.

Dimensioning of coupling

The dimensioning of the elastic RINGFEDER® couplings is based on the nominal torque T_N and maximum impact torque T_{max} of the machines.

Equation 1)

$$T_N = 9550 \cdot P_N / n_N$$

T_N	= Nominal torque of machine	[Nm]
P_N	= Machine power	[kW]
n_N	= Operating speed	[min ⁻¹]

The following equation applies when subjected to the nominal torque:

Equation 2)

$$T_{KN} > T_N \cdot S_{\vartheta} \cdot S_f$$

T_{KN}	= Nominal torque of coupling	[Nm]	acc. to Paper data
T_N	= Nominal torque of machine	[Nm]	acc. to equation 1)
S_{ϑ}	= Temperature factor	[-]	acc. to table
S_f	= Service factor	[-]	$S_A \cdot S_L$
S_A	= Load factor of drive side		
S_L	= Load factor of output side		

Verifying the maximum torque of the coupling

The following equation applies for transient impact torques, which occur e.g. by starting an electric motor

Equation 3)

$$T_{Kmax} > T_{max} \cdot S_{\vartheta} \cdot S_Z$$

T_{Kmax}	= Maximum torque of the coupling	[Nm]	acc. to Paper data
T_{max}	= Maximum impact torque of machine *	[Nm]	

* e.g. when starting an electric motor: $T_{max} = T_{Kipp}$

T_{Kipp} = Tipping torque by starting with directly engaged asynchronous motor
e.g. $T_{Kipp} \sim 2,5 \cdot T$; observe details of motor producer

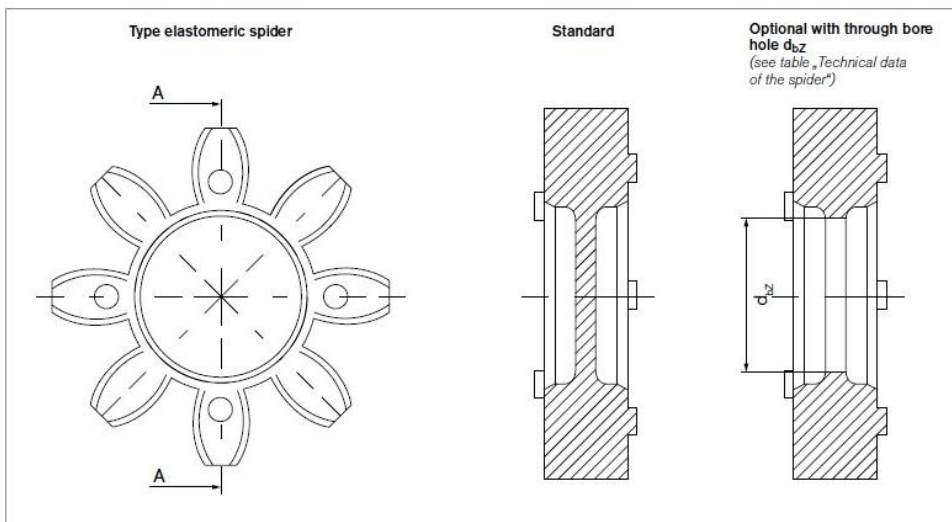
Start-ups per hour [1/h]	Start-up factor S_Z
< 120	1
120 - 240	1,3
>240	On request

S_Z = Start-up factor

Technical data of the elastic spider

Spider Hardness (Shore)	Colour	Material	Allowable temperature °C		Available for size	Typical applications; preferred characteristics
			Continuous temperature	Max. temp. short term		
80 SH A	blue	Polyurethane	-50 to +80	-60 to +120	5-19	Drives in electronic measuring systems; backlash-free when pre-compressed
92 SH A	yellow	Polyurethane	-40 to +90	-50 to +120	5-55	Main spindle drives; backlash-free when pre-compressed
*95/98 SH A	red	Polyurethane	-30 to +90	-40 to +120	5-75	Positioning drives; backlash-free when pre-compressed
64 SH D-H	green	Hytrell	-50 to +120	-60 to +150	7-38	Machine tool spindles, control drives, lead units, planetary gearboxes; heavy loads, torsionally stiff, high ambient temperature, water proof
64 SH D	green	Polyurethane	-20 to +110	-30 to +120	42-75	

* From size 65 to 95 SH A

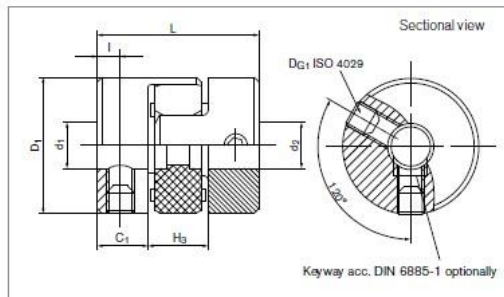


Technical data of the spider

Size	SH	1/min					Nm		Nm/rad	10 ³ Nm/rad	N/mm	optional d _{bz} *	mm			Degree
		(5102)	(5103)	η _{max} (5103.1)	(5104)	(5112)	T _N	T _{max}					C _{Tstat}	C _{Tdyn}	C _r	
5	80 SH A						0,3	0,6	3,2	10	82				0,12	1,1
	<p>TKN – Nominal torque of coupling (Nm): Continuous torque which can be transmitted throughout the entire speed range, taking into consideration operational factors such as ambient temperature, operating, impact and start-up factors.</p> <p>TKmax – Maximum torque of coupling (Nm): Torque which can be transmitted >10⁵ time as a peak load or 5 x 10⁴ times as an alternating load during the entire life of the coupling taking into consideration factors such as temperatures, torsional stiffness and shock loading. The shaft-hub connection must be tested by the customer.</p> <p>The stated static torsional stiffness CTstat and dynamic torsional stiffness CTdyn are valid for 0.5 TKN.</p> <p>The axial misalignment Ka refers to the gap size shown in the data sheets.</p>															
7	92 SH A						7,5	15	115	344	336				0,15	1,0
	98 SH A						12,5	25	172	513	654				0,09	0,8
9	64 SH D-H						21	42	1240	3720	2930				0,04	0,8
	80 SH A	12000	10000	---	10000	19000	5	10	340	1030	582	16	+1,2/-0,5	0,15	1,1	
12	92 SH A						10	20	570	1720	1120				0,1	1,0
	98 SH A						17	34	860	2580	2010				0,06	0,8
14	64 SH D-H						75	150	2980	8934	3696				0,07	0,8
	80 SH A	8500	7000	---	7000	13800	35	70	1430	4296	1480	24	+1,4/-0,5	0,14	1,0	
19	92 SH A						60	120	2060	6189	2560				0,1	0,9
	98 SH A						90	180	4350	13020	4310				0,08	0,8

RINGFEDER® GWE 5102

Miniature coupling with set screw hubs



Size	d ₁ ;d ₂ min-max		d _{1k} ;d _{2k} min-max		C ₁ mm	D ₁ mm	H ₃ mm	I mm	L mm
	Without keyway	With keyway	Without keyway	With keyway					
5	2 - 5	---	---	---	5	10	5	2,5	15
7	3 - 8	6 - 8	6 - 8	6 - 8	7	14	8	3,5	22
9	3 - 12	6 - 10	6 - 10	6 - 10	10	20	10	5	30
12	4 - 12	6 - 12	6 - 12	6 - 12	11	25	12	5	34
14	4 - 16	6 - 16	6 - 16	6 - 16	11	30	13	5	35
19	6 - 24	6 - 24	6 - 24	6 - 24	25	40	15	10	55
24	8 - 35	8 - 35	8 - 35	8 - 35	30	55	18	10	78
28	---	10 - 38	10 - 38	10 - 38	35	65	20	15	90
38	---	12 - 48	12 - 48	12 - 48	45	80	24	15	114

Transmission of the couplings transmissible torque T can not longer be guaranteed for certain with borings < d_{min}. Types with borings < d_{min}, however, can be supplied.

Moment of inertia and weight (mass) are calculated with reference to the largest bore size.

Size	T	H _{es}	n _{max}	J	Gw	D _{G1}	T _{A1}
	Nm		1/min	10 ⁻⁹ kgm ²	kg	mm	Nm
5	0,5	92 SHA	47500	0,000034	0,005	1 x M3	1,3
7	1,2	92 SHA	34000	0,000196	0,009	1 x M3	1,3
9	3	92 SHA	24000	0,00108	0,017	2 x M4	3
12	5	92 SHA	19000	0,00284	0,03	2 x M4	5
14	7,5	92 SHA	16000	0,0057	0,041	2 x M6	6
19	10	92 SHA	12000	0,036	0,138	2 x M6	6
24	35	92 SHA	9500	0,162	0,282	2 x M6	6
28	95	92 SHA	7300	0,322	0,454	2 x M6	6
38	190	92 SHA	5900	0,954	0,875	2 x M6	6

Elastomer Jaw Couplings RINGFEDER® GWE 5102

Transmissible torque T [Nm] of the Shaft-Hub-Connection

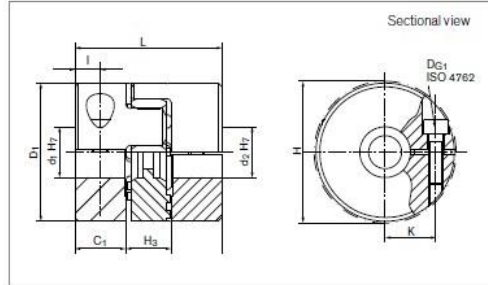
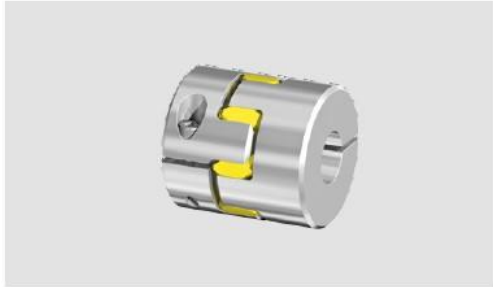
Size	Ø3	Ø4	Ø5	Ø6	Ø7	Ø8	Ø9	Ø10	Ø12	Ø14	Ø16	Ø18	Ø20	Ø22	Ø24	Ø28
5	0,5	0,5	0,5	---	---	---	---	---	---	---	---	---	---	---	---	---
7	1,2	1,2	1,2	1,2	1,2	1,2	---	---	---	---	---	---	---	---	---	---
9	3	3	3	3	3	3	3	3	3	---	---	---	---	---	---	---
12	---	5	5	5	5	5	5	5	5	---	---	---	---	---	---	---
14	---	7,5	7,5	7,5	7,5	7,5	7,5	7,5	7,5	7,5	7,5	---	---	---	---	---
19	---	---	---	10	10	10	10	10	10	10	10	10	10	10	10	---
24	---	---	---	---	---	20	22	24	29	34	35	35	35	35	35	35
28	---	---	---	---	---	---	---	95	95	95	95	95	95	95	95	95
38	---	---	---	---	---	---	---	---	190	190	190	190	190	190	190	190

Explanations

d ₁ ;d ₂ min = Min. bore diameter d ₁ /d ₂	D ₁ = Outer diameter	n _{max} = Max. rotation speed
d ₁ ;d ₂ max = Max. bore diameter d ₁ /d ₂	H ₃ = Length of damping module	J = Total moment of inertia
d _{1k} ;d _{2k} min = Min. bore diameter d ₁ /d ₂ With keyway acc. to DIN 6885-1	I = Distance between center screw hole and hub end	Gw = Weight
d _{1k} ;d _{2k} max = Max. bore diameter d ₁ /d ₂ With keyway acc. to DIN 6885-1	L = Total length	D _{G1} = Thread
C ₁ = Guided length in hub bore	T = Transmissible torque at given T _A	T _{A1} = Tightened torque of clamping screw D _{G1}
	H _{es} = Hardness of the elastomeric spider	

RINGFEDER® GWE 5103

Servo-Insert coupling with clamping hubs, short length and single slit



Size	d_1, d_2 min-max	d_{1k}, d_{2k} min-max	C_1	D_1	H	H_3	I	K	L
	Without keyway	With keyway							
	mm	mm	mm	mm	mm	mm	mm	mm	mm
7	3 - 7	6 - 7	6	14	16,5	8	3	5	20
9	4 - 11	6 - 11	8	19,5	23	10	4	7,5	26
12	4 - 12	6 - 12	7	25	26	12	3,5	8,5	26
14	5 - 15	6 - 15	9,5	29,5	33	13	5	10,5	32
19	8 - 22	8 - 22	17	39,5	43	15	6	15	50
24	10 - 31	10 - 31	20	54,5	56	18	10	20	58
28	14 - 35	14 - 35	21,5	64,5	67	19	11	23,5	62
38	15 - 46	15 - 46	31	79,5	88	23	13	30	85
42	20 - 56	20 - 56	38	94,5	95	26	14	35	102

Transmission of the couplings transmissible torque T can not longer be guaranteed for certain with borings < d_{min} . Types with borings < d_{min} , however, can be supplied.

Moment of inertia and weight (mass) are calculated with reference to the largest bore size.

Size	T	H_{es}	n_{max}	J	Gw	D_{G1}	T_{A1}
	Nm		1/min	$10^{-9}kgm^2$	kg	mm	Nm
7	1,2	92 SH A	27000	0,0001	0,006	1 x M2	0,35
9	3	92 SH A	19000	0,0002	0,019	1 x M2,5	0,75
12	5	92 SH A	15000	0,00223	0,023	1 x M3	1,5
14	12,5	98 SH A	13000	0,006	0,049	1 x M4	5
19	17	98 SH A	10000	0,029	0,12	1 x M5	10
24	60	98 SH A	7000	0,121	0,28	1 x M6	18
28	160	98 SH A	6000	0,236	0,365	1 x M8	36
38	325	98 SH A	5000	0,797	0,85	1 x M10	84
42	450	98 SH A	4000	1,779	1,5	1 x M10	84

Elastomer Jaw Couplings RINGFEDER® GWE 5103

Transmissible torque T [Nm] of the Shaft-Hub-Connection

Size	Ø3	Ø4	Ø5	Ø6	Ø8	Ø10	Ø12	Ø14	Ø15	Ø18	Ø20	Ø25	Ø26	Ø28	Ø30	Ø35	Ø40	Ø45	Ø50	Ø55	Ø56
7	0,7	0,9	1,1	1,2	--	--	--	--	--	--	--	--	--	--	--	--	--	--	--	--	--
9	--	1,7	2,1	2,4	3	3	--	--	--	--	--	--	--	--	--	--	--	--	--	--	--
12	--	2,9	3,6	4,2	5	5	5	--	--	--	--	--	--	--	--	--	--	--	--	--	--
14	--	--	9	10,6	12,5	12,5	12,5	12,5	12,5	--	--	--	--	--	--	--	--	--	--	--	--
19	--	--	--	--	17	17	17	17	17	17	17	--	--	--	--	--	--	--	--	--	--
24	--	--	--	--	--	43,9	51,9	60	60	60	60	60	60	60	60	--	--	--	--	--	--
28	--	--	--	--	--	--	--	92	98	115	126	153	159	160	160	160	--	--	--	--	--
38	--	--	--	--	--	--	--	191	226	248	302	312	325	325	325	325	325	325	--	--	--
42	--	--	--	--	--	--	--	--	--	250	305	316	337	358	408	450	450	450	450	450	450

Explanations

d_1, d_{2min}	= Min. bore diameter d_1/d_2	H	= Clearance diameter	n_{max}	= Max. rotation speed
d_1, d_{2max}	= Max. bore diameter d_1/d_2	H_3	= Length of damping module	J	= Total moment of inertia
d_{1k}, d_{2kmin}	= Min. bore diameter d_1/d_2 With keyway acc. to DIN 6885-1	I	= Distance between center screw hole and hub end	Gw	= Weight
d_{1k}, d_{2kmax}	= Max. bore diameter d_1/d_2 With keyway acc. to DIN 6885-1	K	= Distance shaft axis - clamping screw axis	D_{G1}	= Thread
C_1	= Guided length in hub bore	L	= Total length	T_{A1}	= Tightened torque of clamping screw D_{G1}
D_1	= Outer diameter	T	= Transmissible torque at given T_A		
		H_{es}	= Hardness of the elastomeric spider		